

AD707747

OPTICAL PUMPING OF LASERS

FINAL REPORT

TECHNICAL REPORT NO. 3

FOR PERIOD FROM 1 JUNE 1969 TO 31 MARCH 1970

31 MAY 1970

Sponsored By  
Advanced Research Projects Agency  
ARPA Order No. 1312  
Contract N00014-69-C-0428

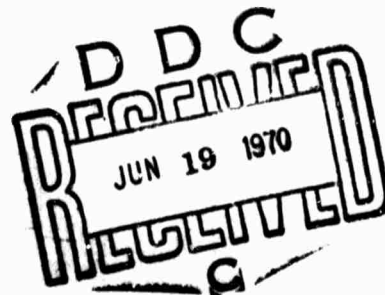
Effective Contract Date 1 June 1969  
Expiration Contract Date 31 March 1970  
Cost \$49,000

Lyle H. Taylor, Principal Investigator (412) 256-7769  
Irving Liberman, Richard Liebermann,  
Alex Federowicz, Lloyd Armstrong, Jr. (Consultant)

Reproduction in whole or in part is permitted for any  
purpose of the United States Government.

Distribution of this document is unlimited.

This document has been approved  
for public release and sale; its  
distribution is unlimited.



181

OPTICAL PUMPING OF LASERS

FINAL REPORT

TECHNICAL REPORT NO. 3

FOR PERIOD FROM 1 JUNE 1969 TO 31 MARCH 1970

31 MAY 1970

Sponsored By  
Advanced Research Projects Agency  
ARPA Order No. 1312  
Contract N00014-69-C-0428

Effective Contract Date 1 June 1969  
Expiration Contract Date 31 March 1970  
Cost \$49,000

Lyle H. Taylor, Principal Investigator (412) 256-7769  
Irving Liberman, Richard Liebermann,  
Alex Federowicz, Lloyd Armstrong, Jr. (Consultant)

Reproduction in whole or in part is permitted for any  
purpose of the United States Government.

Distribution of this document is unlimited.

# ABSTRACT

The emission spectra of 40 amp-2.5 atm xenon and krypton arc discharges are calculated. The spectral overlap of these spectra and the measured emission spectra of tungsten and potassium-mercury arc discharges with the measured absorption spectra of Nd:YAG are used to determine relative system efficiencies which agree well with measured values. It is found that the K-Hg lamp is four times more efficient in pumping Nd:YAG than the studied W, Kr, and Xe lamps. The spectral overlap calculation for a typical ruby oscillator-amplifier at the peak of the flash lamp pulse gives a pump efficiency which is much higher than measured system efficiencies. This discrepancy may be caused by the time dependent behavior of the flash lamp pulse and the oscillator pulse. A new technique is developed to obtain electronic radial wave functions from known radial integrals. In a test case, the Cu 4s wave function is determined within  $\pm 8\%$ . Group theory is applied to the calculation of radial integrals involving hydrogen wave functions and some selection rules are explained.

## TABLE OF CONTENTS

	<u>PAGE</u>
1. INTRODUCTION.....	1
Nd:YAG LASERS	5
2. LAMP EMISSION SPECTRA.....	5
2.1 Theoretical Results for Xenon and Krypton.....	7
2.1.1 Arc Composition.....	8
2.1.2 Transport Properties.....	9
2.1.3 Line Radiation.....	11
2.1.4 Continuum Radiation.....	13
2.1.5 Temperature Profile.....	15
2.1.6 Arc Emission.....	16
2.2 Comparison of Theoretical and Experimental Results.....	17
2.2.1 Xenon.....	18
2.2.2 Krypton.....	20
2.3 Measured Spectra for W and K-Hg Lamps.....	21
2.4 Discussion.....	22
3. LASER ABSORPTION SPECTRA.....	26
4. SYSTEM EVALUATION.....	27
4.1 Lamp Efficiency.....	27
4.2 Slab Efficiency.....	28
4.3 Pump Efficiency.....	29
4.4 Activator Efficiency.....	32
4.5 Discussion.....	33
5. SUMMARY.....	34

## TABLE OF CONTENTS (Continued)

	<u>PAGE</u>
<b>RUBY LASERS</b>	37
6. INTRODUCTION.....	38
7. LAMP EMISSION SPECTRUM.....	39
8. RUBY ABSORPTION SPECTRA.....	40
9. SYSTEM EVALUATION.....	41
9.1 Lamp Efficiency.....	41
9.2 Slab Efficiency.....	42
9.3 Pump Efficiency.....	43
9.4 Activator Efficiency.....	43
10. SUMMARY.....	45
<b>RADIAL WAVE FUNCTIONS</b>	47
11. PARAMETER FITTING FROM SLATER INTEGRALS.....	48
11.1 PF Constraints.....	49
11.2 PF Basis Sets.....	51
11.3 Numerical Procedures.....	53
11.4 Screening Constants.....	57
11.5 Application to the Cu 4s Electron.....	59
12. GROUP PROPERTIES.....	63
13. SUMMARY.....	65
APPENDIX 1 - A Comparison of Lamps for Use in High Continuous Power Nd:YAG Lasers.....	68
APPENDIX 2 - Rod to Slab Transformation.....	72
APPENDIX 3 - Newton's Method for Parametric Fitting of Radial Wave Functions in Integrals.....	76

## TABLE OF CONTENTS (Continued)

	<u>PAGE</u>
APPENDIX 4 - Comparison of Direct Search and Newton's Method.....	81
APPENDIX 5 - Group Theoretical Properties of Radial Wave Functions.....	84
APPENDIX 6 - Group Properties of Hydrogenic Wave Functions.....	92
REFERENCES .....	101
TABLES.....	105
FIGURES.....	128

May 31, 1970

## OPTICAL PUMPING OF LASERS

L. H. Taylor, I. Liberman,  
R. Liebermann, A. Federowicz, L. Armstrong\*

### 1. INTRODUCTION

The optically-pumped solid-state laser provides the highest peak power from coherent sources. However, one of the main energy losses in optically pumped lasers is in the energy transfer between the optical pump and the laser medium. This report summarizes the progress toward measuring and optimizing this energy transfer.

The energy transfer can best be optimized by maximizing the spectral overlap between the emission spectrum of the optical pump and the absorption spectrum of the lasing medium. Since the lasing medium is optimized for its lasing properties, it is unlikely that its absorption spectra can be significantly altered without reducing its desirable lasing properties. On the other hand, the single job of the optical pump is to convert electrical energy to optical energy in such a manner that the lasing medium absorption of the optical energy is maximized. It then follows that the best approach is to change the optical pump until the spectral overlap is maximized for a particular lasing medium. The most common optical pump is a wall-stabilized arc discharge, and therefore this type of discharge is the subject of this report.

The work in this contract is divided into two Phases. In the first Phase the emission spectra of xenon and krypton arc discharges are calculated and measured. This permits an evaluation of the theoretical results. The measured absorption spectra of Nd:YAG and ruby laser slabs are then converted to digital form and the pump efficiencies

\* Consultant, permanent address: The John Hopkins University, Baltimore, Maryland.

of different lamps for these laser materials are calculated. In the second Phase an atomic radial wave function is expanded in a power series with fitting parameters, and the fitting parameters are then adjusted to reproduce the Slater integrals determined from spectroscopic measurements. Thus the radial wave function is "experimentally" determined and is independent of the atomic shell structure complexities. Moreover, the group theoretical properties of hydrogenic radial wave functions are investigated to establish group theoretical methods for the evaluation of radial integrals.

These two Phases complement each other. The pump efficiency calculation will be possible for both experimental and theoretical spectra. However, at present the emission spectra of arc discharges can only be calculated for the noble gases and the alkali metal gases. When the second Phase is successfully developed, the emission spectra will be calculable for any monatomic gas provided only that the energy levels of the emitting atoms are known (this condition already exists for the first Phase).

The Phase One work in this report is divided into two parts. The first part investigates the narrow absorption line Nd:YAG laser whereas the second part investigates the broad absorption band ruby laser. In each part the lamp emission spectra, the slab laser absorption spectra, and the useful overlap of these spectra are measured or calculated. In the first part the emission spectra of a xenon arc discharge and of a krypton arc discharge are calculated and compared to experimental measurements. The spectral overlaps of these calculated spectra and of the tungsten and potassium-mercury measured emission spectra with the measured 0.7% Nd:YAG absorption spectra are then computed. The calculations thus evaluate the lamp emission efficiencies, the Nd:YAG slab fluorescence efficiencies when pumped by the various lamps, and the total system efficiencies. The latter two efficiencies are evaluated as a function of the slab thickness. Since most laser materials are in the form of a cylindrical rod, a relationship between slab thickness and rod diameter is given.



In the second part the spectral overlap for a typical ruby laser is calculated from the measured spectrum at the peak radiance of a xenon flash lamp and the measured absorption spectra (there are two spectra because ruby is anisotropic). The efficiencies are calculated from these spectral overlaps. The difference between a four-level laser such as Nd:YAG and a three-level laser such as ruby are explicitly considered.

Phase Two of this report is concerned with the evaluation of radial wave functions. The energy levels of any free atom or ion are experimentally determined by its emission spectrum and theoretically determined by radial integrals such as the spin-orbit coupling constant and the Slater integrals. The normal procedure is to parameterize these radial integrals and fit them to the experimentally determined energy levels. The parameter fitting (PF) technique developed and tested in Phase Two adjusts the parameters in a power series expansion of the radial wave function until the experimentally determined radial integrals are reproduced. The resulting power series representation of the radial wave function can then be used to calculate the transition probabilities which are required for the prediction of emission spectra in lamps.

A more powerful alternative to the PF technique may be group theoretical techniques for the evaluation of radial integrals. The group properties of hydrogen radial wave functions are examined since they are presumably the simplest wave functions. Although this investigation has been short and is not completed, it has already produced significant results which explain some apparent "selection rules" of radial integrals.

To accomodate the reader who may not be interested in all of this report, the material has been divided into three large parts: Nd:YAG LASERS, RUBY LASERS, and RADIAL WAVE FUNCTIONS. Although the three parts are interrelated, they are written in a self-contained manner so that the reader may read them individually or in any order.

**Nd:YAG LASERS**

## 2. LAMP EMISSION SPECTRA

The necessary input information to obtain the laser pumping efficiency of a lamp is its spectral emittance and the excitation spectrum of the lasing medium. The lasing media of  $\text{Nd:Y}_3\text{Al}_5\text{O}_{12}$  (Nd:YAG) and  $\text{Cr:Al}_2\text{O}_3$  (ruby) will be considered in later chapters, whereas the spectral emittance of several lamps is considered in this chapter.

The lamp spectra are difficult to obtain experimentally. Most continuous gas discharges and low to medium energy pulsed discharges have considerable line spectra which are difficult and tedious to measure experimentally and then convert to computer data cards. It would simplify the work considerably if the spectra could be calculated rather than measured experimentally. To do this for an arbitrary gas discharge under arbitrary operating conditions is not possible at the present state of the art. In fact, the major objective of this contract is to make some headway in calculating the properties of one class of atoms. However, because of many years effort<sup>1,2,3</sup> we believe we can calculate to a reasonable degree of precision the atomic and ionic spectra of the noble gases and the alkali metals. Fortunately, these atoms create discharges which have proved to be of interest for pumping lasers. Therefore we believe we can measure and optimize spectral overlap between pump and rod quicker and better by using calculated rather than experimental spectra.

The work done in 1969 was to verify that the calculated spectra compare favorably with the experimental. Therefore careful controlled measurements of the spectral radiance of a xenon and a krypton continuous arc were made. Computer calculations of these arcs were performed, given only the experimental values of lamp dimensions, current and pressure. To save time and money only the measured spectral radiances were used for a tungsten lamp and a potassium-mercury lamp.

## 2.1 Theoretical Results for Xenon and Krypton

The gas discharge consists of a cylindrical arc confined by a cylindrical tube. In this wall-stabilized arc, electrical current carries power into the positive column of the arc. Radiation and thermal conduction to the wall take power out of the positive column. Convective power transport is negligible in wall-stabilized arcs and will not be considered. An arc discharge has a central plasma core at the temperature of the fully ionized plasma and a cold sheath adjacent to the wall at a temperature determined by the rate at which power flows from the wall to the outside world. (A fully ionized plasma is a misnomer which means that the electron-electron and electron-ion interactions are the dominant particle-particle interactions. It does not mean that the gas is completely ionized.)

The emission from a cylindrical wall-stabilized gaseous arc discharge is calculated with a minimal amount of input information. The requisite macroscopic parameters are: (1) the length and diameter of the discharge tube, (2) the electrical current into the tube, (3) the tube wall temperature, and (4) the ambient pressure in the discharge. These parameters are easily obtained for dc discharges. The requisite microscopic parameters are: (1) the amounts of each substance (e.g., water vapor, water, xenon, etc.) present before the discharge is struck, (2) the heat capacities  $C_p$  as a function of the temperature  $T$ , (3) the heats of formation  $\Delta H(T)$  for each species present in the tube before and during the discharge, (4) the lower lying energy levels and their SLJ classification for each species in the discharge, and (5) the momentum-transfer cross sections for the species in the discharge. These parameters are difficult to obtain and are approximated whenever our knowledge is insufficient.

Given the necessary input data, the arc discharge properties are calculated as a function of temperature in the following order: (1) the arc composition, (2) the electrical and thermal conductivities of the arc gases, (3) the line radiation, (4) the continuum radiation, and

(5) the line shifts and broadening. The temperature profile and the resultant arc discharge emission can then be calculated. The calculation of the line radiation by the present computer programs restricts these calculations to arc discharges with only rare and alkali metal gases. The development of Phase Two of this contract should extend the applicability of these calculations to any atomic gases in arc discharges.

It is easily seen that a little input information generates a lot of output information. The computer programs needed in the calculations were developed by Westinghouse on internal funds and on previous government contracts. They were updated and corrected whenever necessary during the arc discharge calculations which are summarized in the remainder of Section 2.1.

#### 2.1.1 Arc Composition

The equilibrium composition of an arc at a given temperature and pressure is usually calculated by assuming local thermodynamic equilibrium (LTE) and then using the Saha Equations.<sup>4</sup> These equations need partition functions and ionization potentials for the various species in the discharge. However, in a plasma, charges of one sign are, on an average, surrounded by an excess charge of the opposite sign. This lowers the ionization potential and Debye has derived the equation which gives the magnitude of this lowering.<sup>4</sup> In practice this Debye lowering is introduced into the Saha Equations and, after an initial guess of this lowering, the Saha Equations are iterated until a self-consistent Debye lowering is obtained. This method is adequate for simple gases such as xenon or krypton but totally inadequate for complicated discharges.

R. Liebermann has developed a more complete approach which is applicable to any system (it has been applied to the  $SF_6$  discharge in which each  $SF_6$  molecule is decomposed into 22 different species). The Gibbs free energy is calculated from given heat capacities and heats of formation. The Gibbs free energy is then minimized,<sup>5</sup> under mass balance

and charge conservation constraints, via the geometric programming techniques of Duffin et al.<sup>6</sup> The Debye lowering is again introduced as an iteration parameter and the simultaneous equations iterated until a self-consistent Debye lowering is obtained.

For the simple pure xenon or krypton discharge, either approach can be used but because the Liebermann program is more general, it was used. Since the heat capacity should vary slowly with the Debye lowering, it was held constant during the iterations on the Debye lowering. The heats of formation were used as a function of temperature. To simplify the calculation it was assumed that the discharge was optically thick below 2000 Å and optically thin above 2000 Å. Thus the ultraviolet radiation effects were completely ignored. The results of the calculations for a pressure of 2.5 atm are given in Figs. 1 and 2. The temperature range was between 1000°K (the assumed wall temperature) and 18,000°K. We expected the highest temperature in the discharges to lie between 6,000°K and 10,000°K, but another calculation on a Na-Br discharge led us to believe that a temperature as high as 15,000°K might be possible. A comparison of Figs. 1 and 2 shows that the higher first and second ionization potentials of Kr require higher temperatures for ionization. In fact the concentration of ions is not significant below about 10,000°K for Xe and below about 11,000°K for Kr.

#### 2.1.2 Transport Properties

The electrical and thermal conductivities are calculated by the first Chapman-Enskog approximations as formulated by Yos<sup>7</sup> and by Brokaw.<sup>8</sup> The electron-neutral momentum-transfer cross sections for xenon have been measured by Frost and Phelps<sup>9</sup> as a function of temperature. To simplify the xenon calculations a value of  $13.17 \text{ Å}^2$  was taken for all temperatures. This was the value measured by Frost and Phelps at 10,000°K. In the highly ionized regime Sptizer's formula<sup>10</sup> was used. The neutral-neutral cross sections were estimated by Brokaw's method.<sup>11</sup> The neutral-ion cross sections are unknown but based on our previous experience with other discharges, a value of 2.5 times the neutral-neutral cross sections seemed reasonable and was taken. Since the ions

should constitute a small part of the discharge, this approximation is not critical and may even be insignificant. It also seemed reasonable to identically equate the unknown  $Q^{(2,2)}$  averaged cross sections to the  $Q^{(1,1)}$  averaged cross sections.<sup>13</sup> The xenon conductivity results are shown in Figs. 3 and 4.

Included in Figs. 3 and 4 are the results of Devoto which were published in 1967<sup>12</sup> and 1969.<sup>13</sup> When the present calculations were done only the 1967 Devoto results were known, and they were thought to be in error. The 1969 Devoto results confirm this and are quite close to the present results; the differences are easily explained. At low temperatures Devoto used a temperature-dependent electron-neutral cross section whereas our value was temperature-independent. At high temperatures Devoto used an ion-neutral cross section which was about 10 times the neutral-neutral value whereas we used a multiplicative factor of 2.5.

The electrical and thermal conductivities were more accurately calculated for the krypton discharge. The temperature dependent electron-neutral momentum-transfer cross section was used and, as given by Devoto,<sup>13</sup> is shown in Fig. 5. As a check on our cross sections and calculations, the electrical conductivity was calculated at 1.0 atmospheres and compared with Devoto's results<sup>13</sup> (Devoto did the calculation at 1.0 atmospheres, but not at 2.5 atmospheres). Our results, labeled Liebermann, are compared to Devoto's results in Fig. 6. At high temperatures the electron-ion momentum-transfer cross sections are significant. The curves differ in these regions because Devoto used different values for these cross sections. At low temperatures the fourth-order calculation by Devoto<sup>14</sup> deviates from our first-order results whereas between 7,000 and 8,000°K the first- and fourth-order theories agree. Devoto found a similar relationship for an argon arc discharge.<sup>14</sup>

The conductivity calculations for krypton were completed by equating  $Q^{(2,2)}$  to  $Q^{(1,1)}$  for the neutral-neutral and the electron-neutral interactions. The neutral-neutral cross sections were again

calculated by Brokaw's method.<sup>11</sup> The  $Q^{(1,1)}$  neutral-ion cross sections were estimated as twice the neutral-neutral cross sections, whereas the  $Q^{(2,2)}$  neutral-ion cross sections were estimated as ten times the neutral-neutral cross sections. The conductivity results are given in Figs. 3 and 4. These curves show a surprisingly small difference between the xenon and krypton results, particularly for the electrical conductivity. In fact, although small, the different cross section approximations used by Devoto give larger differences than changing the gas from xenon to krypton.

### 2.1.3 Line Radiation

Much of the discharge radiation originates from bound-bound transitions, i.e., line radiation. Although much of the science is known for these transitions, the problem is most assuredly nontrivial. Two simplifying assumptions which are usually made is that there is no configuration interaction and that magnetic dipole radiation is insignificant compared to the electric dipole transitions. The first approximation should be very good for simple gases such as xenon but is very bad for certain gases, e.g., mercury. The second approximation should be excellent except for the  $\ell^n - \ell^n$  transitions in the rare earths. Both approximations are made for xenon and krypton.

The wave function, which determines the electric dipole transition probability rate, is determined from a SLJ listing of the energy levels. For xenon I only the lowest five configurations are completely known;<sup>15</sup> these known levels are listed in Table I. For krypton I the lowest nine configurations are completely known. By setting the unknown  $3p_0$  energy level equal to the  $1p_1$  energy level within each ns configuration for n between eight and twelve, five high energy ns configurations can also be included. The energy levels for these fourteen configurations are listed in Table II.

With this energy level information the theoretical expressions for the energy levels can be adjusted to give a least squares fit to the experimental levels by using the radial integrals as fitting parameters. The resultant intermediate coupling angular wave functions for xenon are given in Table III. For example, in the  $5p^5 5d$  configurations:



$$|^1P_1\rangle = 0.717|^3D_1\rangle - 0.298|^3P_1\rangle + 0.630|^1P_1\rangle \quad (1)$$

where  $|\rangle$  is the intermediate coupling and the  $| \rangle$  is the SL coupling wave function. The intermediate coupling angular wave functions for krypton are given in Table IV (Tables III and IV do not list the trivial one-component eigenvectors). These last two tables dramatically show the well known collapse of SL coupling in the rare gases.

The Westinghouse intermediate coupling program is only valid for the rare gases, and moreover, was found to give incorrect answers. Previous to this contract the very versatile electric dipole transition computer program written by Cowan<sup>17</sup> had been obtained and converted from the IBM STRETCH Computer to the CDC 6600 Computer. A comparison of the two computer results for xenon located the Westinghouse program error which was then circumvented. (If the Cowan computer program were to be incorporated into the Westinghouse intermediate coupling program, any atom with two open shells or less could be handled.) The resultant radial integral values for xenon and krypton are listed in Table V. The  $n'd$  spin-orbit coupling parameters must be positive. The two small negative values are therefore unrealistic and are a result of cumulative errors or configuration interaction. In any event these values are too small to significantly affect the results.

The radial part of the wave functions must also be known to calculate the value of  $|\langle \psi_n | r | \psi_m \rangle|^2$  which is needed to calculate the transition probability rate. These radial wave functions are very difficult to calculate. For simple atoms (less than two equivalent electrons) the radial wave functions are calculated from the Bates and Damgaard Coulomb approximation<sup>18</sup> or the Thomas-Fermi approximation, whichever is most appropriate. Both of these methods require one electron energies and consequently break down whenever more than one equivalent electron is present. The development of Phase 2 of this contract will remove this restriction and also make this part of the calculation consistent with the intermediate coupling determined radial integrals.

The Thomas-Fermi method was exclusively used for xenon and for the five lowest configurations of krypton. The more important values of the resultant transition probability rates and transition wavelengths are listed in Table VI. As a check of our results, the thirty 5s-5p transition probabilities for krypton were compared to the results of Murphy.<sup>19</sup> The agreement is within 8% which is very satisfactory. The results of Table VI show that both atoms emit considerable energy in the ultraviolet although xenon radiates about twice as much energy in this wavelength region as does krypton. Consequently, the ultraviolet optical thickness assumption made in the arc discharge calculations will be a worse approximation for xenon than for krypton. In the infrared region xenon essentially has no radiation whereas krypton does have a small amount of radiation. The total line radiation as a function of temperature has been calculated and is given in the next subsection where it is compared to the continuum radiation.

#### 2.1.4 Continuum Radiation

The free-bound and free-free electronic transitions yield continuum radiation, but the theory for these transitions is rather crude. The spectral absorptivity for these transitions is given by

$$K(\lambda, T) = \sum_i g_i \sigma_i(\lambda) \exp(-E_i/kT)/Z_0 \quad (2)$$

where  $Z_0$  is the internal partition function,  $g_i$  is the statistical weight of the initial state,  $E_i$  is the energy, and  $\sigma_i$  is the photoelectric cross section for the  $i$ th species. The exponential factor is simply the Boltzmann factor. Unsöld<sup>20</sup> showed for hydrogen how the summation could be changed to an integration. Schlüter<sup>21</sup> has generalized Unsöld's work to give

$$K = \frac{32\pi^2 e^6 k}{3\sqrt{3} h^4 c^4} \frac{T}{Z_0} \lambda^3 \exp(-\chi/kT) [\exp(hc/\lambda kT) - 1] \gamma \xi \quad (3)$$

where  $\chi$  is the ionization energy,  $\gamma$  is the statistical weight of the core state, and  $\xi$  is a temperature dependent factor with  $O(1)$ . The latter

factor is very difficult to determine. The values given in Schlüter's paper for xenon are reproduced in Fig. 7. The Schlüter curves should be the most accurate. Biberman et al.<sup>22</sup> used the hydrogenic approximation whereas Yankov<sup>23</sup> used a modified hydrogenic approximation. For short wavelengths  $\xi$  increases exponentially with increasing wavelength. In the intermediate range between 5000 and 6500 Å, the  $\xi$  factor is extremely difficult to determine. In this region the absorption edges appear, but they are shifted to longer wavelengths by plasma interactions and there is no satisfactory theory for these shifts. Hence, the  $\xi$  factor is extremely crude between 5000 and 6500 Å. The absorption edges should be sharper than those shown by Schlüter, and might appear as Liebermann's curve shows in Fig. 7. The  $\xi$  factor for krypton is given in Fig. 8.

The evaluation of Eq. (3) in the literature has led to some confusion. The value of  $\gamma$  for xenon should technically be four, since the core state is split into the  $^2P_{3/2}$  and  $^2P_{1/2}$  states and the  $J = 3/2$  state is the ground state. However, a few people such as Schlüter use a value of six. Schlüter has shown that the value of  $\gamma$  is not important if one is consistent because the  $\xi$  factor contains a  $\gamma^{-1}$  factor. However, we used the partition function for  $\gamma$  (which is approximately four) but used Schlüter's  $\xi$  which contained the value of  $\gamma = 6$ . This confusion lead to a few incorrect early results but was eventually corrected.

The continuum radiation is calculated from the effective spectral absorptivity

$$K' = K[1 - \exp(-hc/\lambda kT)] \quad (4)$$

which is the difference between the true absorption and induced emission. Equation (4) is also valid for the line absorptivities. The radiation is then calculated as the radiated power per unit volume, as is given by the spectral emission coefficient

$$\epsilon(\lambda, T) = B_{\lambda} K' \quad (5)$$

where  $B_\lambda$  is the Planck black body intensity which is given by

$$B_\lambda = \frac{2hc}{\lambda^5} [\exp(hc/\lambda kT) - 1] \quad (6)$$

The line and continuum radiation results are given in Figs. 9 and 10.\* The former figure shows that the line radiation is more important in xenon than in krypton and is always significant for both arc discharges within the specified temperature range. The latter figure shows that below 12,000°K the xenon arc discharge emits more radiation than the krypton arc discharge. The radiation peaks in Fig. 10 are a result of two competing factors; as the temperature is increased each atom increases its radiation but, at constant pressure, the atomic density decreases. This situation is in contrast to the normal experimental situation where the atomic density is held constant and the pressure is allowed to change.

#### 2.1.5 Temperature Profile

Lowke,<sup>24</sup> at Westinghouse, has developed a very powerful computer program for the determination of temperature profiles. Given the tube radius, the wall temperature and the central temperature of the arc, the program uses a relaxation method to determine a profile, the current and the electric field strength. Of course, the electrical and thermal conductivities and the radiation must also be given. The electric field strength is guessed and then iterated until a self-consistent solution is obtained. The discharge is assumed to be optically thin.

The electrical characteristics of the xenon and krypton arc discharges are shown in Fig. 11. Two characteristics are shown for xenon; one was determined from Devoto's<sup>12</sup> conductivities and one was determined from our calculated conductivities (see Figs. 3 and 4). The measured values are also given. At the measured current of forty amperes, the electric field strength calculated from our conductivities is 4% too

---

\*The xenon continuum results in this report differ from those given in Technical Report No. 1. Subsequent to the printing of the latter report a keypunching error in the continuum computer program was discovered and corrected.

low for xenon and 8% too high for krypton. This agreement between the measured and calculated values of the electric field strengths is very good, particularly since, as Mottschmann<sup>25</sup> explains, the ultraviolet radiation which was ignored should lower the calculated value.

A qualitative dependence of the electrical characteristic upon the thermal and electrical conductivities, and thus on the cross sections, is obtained by comparing the two xenon characteristics. Figures 3 and 4 show that Devoto's conductivities are higher than ours and Fig. 11 shows that as a result of Ohm's law these higher conductivities yield a lower electric field strength (40% too low at 40 amp) which in turn leads to a lower central core temperature of the arc discharge.

The calculated temperature profiles for a central core temperature of 9200°K (xenon) and 9775°K (krypton) are given in Fig. 12. They are quite flat over most of the tube volume. Every other point is calculated and the intervening points are interpolated. Linear interpolation explains the small dip at about 2 mm. The wall temperature was fixed at 1000°K for the calculation, although the lamp was water cooled. The steep slope near the wall shows that a crude approximation of wall temperature is sufficiently accurate.

#### 2.1.6 Arc Emission

The wavelength shifts and broadening of the line radiation is first calculated. Griem's<sup>4</sup> electron impact mechanism is evaluated as well as the van der Waals interaction between different species. Resonance broadening is calculated for all transitions in which either the lower or upper state has an allowed electric dipole transition to the ground state. Whenever ions are present the charges cause a polarization effect which also shifts the lines and which is also calculated. The broadening varied from zero to two or three angstroms, and a typical wavelength shift was one angstrom.

These broadenings and shifts are calculated for each line at six different temperatures (see Fig. 12). The absorptivities of these lines are calculated and extended by interpolation. The line radiation

is then integrated along a diameter to give an "effective" line which is the actual emission observed by the experimentalist. The integration is also performed for the continuum radiation. The xenon and krypton results are shown with the experimental results in the next section.

## 2.2 Comparison of Theoretical and Experimental Results

The lamps used for spectral measurements were built at the Research Laboratories. They have been already tested as laser pumps, and spectroscopic measurements were previously made under slightly different operating conditions.<sup>26</sup> An important parameter in all calculations is atom density or pressure. In sealed lamps, the fill pressure is known, but the operating pressure changes with power and can only be calculated if the inactive or dead volume of the lamp is known. To eliminate this possible source of error, the lamps were not sealed but were connected to a large reservoir of fill gas kept at 2.5 atm. Other measured parameters were arc diameter = 0.56 cm, arc length = 7.3 cm, current = 40 A, and voltage = 82 V for xenon and 69 V for krypton. Another lamp of 14.1 cm arc length was operated under identical conditions in order to determine the electrode loss which then was calculated to be 12 V. Therefore, the electric field in the positive column is 9.6 V/cm for xenon and 7.8 V/cm for krypton, and the electrical input power densities (power per unit surface area) are 226 and 192 watts/cm<sup>2</sup> respectively.

Spectral measurements were performed using a Jarrell-Ash 1/2 m Ebert monochromator. For measurement of the line spectra the curved slits were 40  $\mu$  wide corresponding to a dispersion of 0.64  $\text{\AA}$ . In measuring the continuum the slits were opened to 100  $\mu$  in order to increase the detected signal of the relatively weak continuum radiance. The detector used was a silicon p-i-n photodiode. The system was calibrated using a calibrated tungsten spectral radiance standard and automatically corrected for nonlinearity between 5000 - 10,000  $\text{\AA}$  by using a variable attenuator.

### 2.2.1 Xenon

The experimental results are shown and compared with the computer calculations in Fig. 13. Figure 13a shows the experimentally obtained radiance spectrum of xenon between 7500 - 10,000 Å. The computerized equivalent spectrum is shown in Fig. 13b. The two spectra compare well in the location of the lines. Three lines around 9500 Å which appear in the experimental spectrum do not appear in the calculated spectrum. The reason for this discrepancy is not certain, but it appears that these lines originate from high lying configurations of xenon which were not included in the calculation.

Other differences in data include the relative amplitudes of the lines. By examining the experimental data, it appears that all the lines have about the same width. The narrower lines have greater intensity relative to the measured spectrum. The wider the line the closer is the agreement. This discrepancy could be a result of inadequate spectral resolution of the monochromator.

When taking the experimental spectrum we also measured in detail the line shape of the most intense line occurring at about 8232 Å. This measurement is compared with the calculated results at two different core temperatures in Fig. 14. The ordinate and abscissa are the same for both curves. A comparison of the experimental line and the 8450°K computed line shows that the experimental half width of 3.66 Å is 1.0 Å greater than the calculated half width. The dispersion limited resolution of the monochromator is 0.64 Å but the aberration in the instrument could decrease the true resolution to about 1 Å although the manufacturer places the aberration resolution at 0.1 Å. Regardless of the resolution, the energy in the line, which is proportional to the area under the line, i.e., the product of radiance and angstroms, remains constant. Comparing the energies of the calculated and experimental results, we find that the calculated energy is 15% smaller. This difference is surprisingly small since neither spectral curve was expected to be accurate to within 20%.

A comparison of the experimental line and the 9200°K computed line shows that the experimental half width is 1.48 Å smaller than the computed half width, and that the calculated energy is 125% larger. These results indicate that a central core temperature of 8450°K is slightly too low whereas 9200°K is considerably too high. These line shape measurements indicate a central core temperature of  $8530 \pm 150^\circ\text{K}$ .

The calculated curves also show some fine structure not present in the experimental spectrum because of limited resolution. The notch in the short wavelength side of the peak is real and due to self absorption of the hot core by the cool gas near the wall which has its peak absorptivity at shorter wavelengths than the core. There is also a difference in the location of the peak radiance of about 1.3 Å. However, neither value is sufficiently accurate to determine which curve is in error.

In addition to calculating the spectral radiance, the computer also calculates the peak absorptivity, and the emittance. These calculations for the 8232 Å line are shown in Figs. 15 and 16. The emittance is the information needed to calculate the spectral overlap. From the spectral absorptivity we can determine the degree of optical thickness of the line. In this way we have determined that the 8232 Å line does not have the strongest core radiance, but it is less absorbed by the cooler gas so that its emitted radiance is greatest. However, its radiation is also appreciably absorbed; so that the line radiation from a relatively small diameter low-current discharge is already becoming optically thick. In fact at 9200°K the discharge is 80% optically thick and below 6000°K the discharge is 100% optically thin (based on a maximum spectral absorptivity within the specified wavelength region of  $10 \text{ cm}^{-1}$  as being 100% optically thick).

The experimentally measured continuum spectrum is shown in Fig. 17 and a calculated continuum spectrum in Fig. 18. Because of a programming error the ordinate was corrected as shown in the curve. Beyond 7000 Å, comparison becomes difficult because of the contribution



of the wings of the lines to the continuum. A quick glance at the two curves shows that the agreement is poor since the shapes of the curves below  $6000 \text{ \AA}$  are different. (A keypunching error rendered impossible any absolute comparison of continuum radiation amplitudes for this figure although the line radiation results are correct.) We also tried the less sophisticated approach of Yankov.<sup>23</sup> The result appeared to be just slightly better but the shape of the curve still disagreed with the measured curve.

As explained in the section describing the method of calculating the continuum, the bound-free absorption edges occur in the  $5000 - 6500 \text{ \AA}$  region. Therefore, the shape of the continuum depends strongly on correctly choosing Schlüter's  $\xi$  function.<sup>21</sup> Schlüter could not himself get good agreement with experiment for xenon. We considered the possibility of ionic species causing the difficulty, but our calculated results show that this is not a significant factor. We also modified Schlüter's  $\xi$  function as shown by the dotted line in Fig. 7 to account for temperature shifts and obtained the spectrum shown in Fig. 19. The change in spectrum is considerable, and the shape above  $5100 \text{ \AA}$  is in much better agreement with experiment. A comparison of the measured and calculated continuum amplitudes shows fair agreement below  $6000 \text{ \AA}$  but the calculated amplitude is more than a factor of two too low above  $6000 \text{ \AA}$ . Our purpose is not to find a better Schlüter factor by fitting it to the measured spectrum but rather to show that a much better knowledge of the Schlüter factor is necessary if better continua are to be calculated. In the remaining calculations the calculated continuum of Fig. 19 is used.

### 2.2.2 Krypton

The experimental results are shown and compared with the computer calculations in Fig. 20. Figure 20a shows the experimentally obtained spectral radiance of krypton between  $7500 - 10,000 \text{ \AA}$ . The computerized equivalent spectrum is shown in Fig. 20b. A comparison of the line positions shows excellent agreement between the two spectra. As explained in the previous subsection the amplitudes of the two spectra do not compare as well because the computer resolution is finer than the experimental resolution.

The experimentally measured 7,606 Å line and the same line computed with a core temperature of 9,775°K are compared in Fig. 21. The computed line exhibits a -5 Å shift relative to the measured line. Since the unshifted line<sup>15</sup> should occur at 7,604 Å, the experimental apparatus is in error by at least 2 Å. The remaining discrepancy is small but may indicate a slightly too high core temperature. A comparison of the energy under each line shows that the computed line has 21% more energy. This very good agreement is well within the experimental and computed accuracies but again indicates that the computed core temperature may be just slightly too high.

As for the xenon discharge the emittance and spectral absorptivities were also calculated. The krypton discharge is 23% optically thick at 9775°K and 100% optically thin below 7,000°K.

The experimentally measured continuum spectrum is shown in Fig. 22 while the calculated continuum spectrum is shown in Fig. 23. As explained in the previous subsection the continuum calculation is crude. The Schlüter factor shown in Fig. 8 was used although it again lead to the wrong curve shape below 6,000 Å. The amplitudes agree fairly well below 6,000 Å, but the calculated amplitude is about a factor of two, too low above 6,000 Å. These figures again show that a better knowledge of the Schlüter factor is necessary if better continuums are to be calculated.

### 2.3 Measured Spectra for W and K-Hg Lamps

The spectral radiance of the commonly used tungsten lamp was obtained by multiplying the black body radiance at 3,200°K by the measured emissivity at 3,200°K.<sup>27</sup> The spectral emittance was obtained by multiplying by  $\pi$  steradians. This multiplication factor is correct for an optically thick infinite plane emitter radiating onto an infinite plane absorber of finite thickness, or for an infinitely long cylinder of finite radius radiating onto an infinitely long concentric annulus where the annulus thickness is much smaller than the annulus radius.

The input power to the tungsten lamp was calculated as  $\epsilon \sigma T^4$  where  $\epsilon$  is the average emissivity at  $T = 3,200^\circ\text{K}$  and  $\sigma$  is the Stefan-Boltzmann constant.

The potassium-mercury spectral emittance could be theoretically calculated as in the last section but to save time and money the experimental spectral radiance, shown in Fig. 24, was used since it was already available. The spectral emittance was obtained by multiplying the spectral radiance by three. The factor of three was obtained by averaging the factors calculated for the xenon arc discharge which should be about as optically thick as the potassium-mercury discharge. The input power density is given by the 100 volt voltage drop multiplied by the 5 amp current divided by the 2.36 cm circumference times the 3.5 cm arc length. This answer is then reduced by 15% to exclude the end losses.

#### 2.4 Discussion

Because of the narrowness of the lines, it takes about 80 minutes to make one monochromator scan from 5,000 - 10,000 Å, but the major time consumption is spent in building the lamp, set-up time, erroneous starts, etc. The entire procedure would have to be repeated for every parameter change such as current density, pressure, and wall diameter. In addition, after obtaining the data it still has to be converted to computer data cards. This spectrum provides the spectral radiance through the center of the arc. To get the spectral emittance, i.e., the radiation emitted at the wall from all portions of the arc, one would have to obtain the radiance from various rays through the arc and calculate the emittance. The above discussion points out the difficulty of doing the spectral overlap calculation from experimental data. Furthermore, if a pulsed arc were studied the experimental degree of difficulty would be further increased.

The object of comparing the Xe and Kr calculated spectra with the experimental spectra was to determine how close the calculations match the experiments. The results indicate that the line spectra

calculations are appreciably better than the experimental data. There is no absolute way of knowing which spectrum is correct, but it is certain that the experimental data is limited in resolution to at least 0.75 Å. Since the measured lines are only a few angstroms wide, a resolution of 0.75 Å will cause noticeable error. However, the measured energy within a line is independent of the resolution. The agreement for krypton to within 21% between calculation and experiment is better than the accuracy of each method and therefore impossible to determine which method is nearer reality. The xenon line profile at different core temperatures shows how accurate line profiles can be compared to determine the actual core temperature. We therefore conclude that it is very desirable to calculate the line spectrum. It is stressed that the measurements and calculations were carried out completely independently. The calculated line spectra were never altered to fit the experimental spectra. If the experimental measurements were never made, the identical calculated spectra would have been presented.

The calculated continua spectra were only about a factor of two in agreement with experiment. The difference was not only in magnitude, but in wavelength dependence. Since the experimental radiance is estimated to have an absolute certainty of  $\pm 20\%$  and a relative accuracy with wavelength of better than 5%, it is believed that the calculated continua are in error. We believe that the problem is associated with the  $\xi$  factor of Schlüter although attempts at modifying it, after making spectral comparisons, were not entirely successful even though it was apparent that this factor can exert a strong influence. As shown in Figs. 7 and 8, the Schlüter factor appears to be too small above 6,000 Å.

The true value for the continuum radiation from the xenon discharge can be crudely approximated by forming an energy balance of the arc:

$$2\pi E^2 \int_0^r \sigma r' dr' = -2\pi r K \frac{dT}{dr} + \pi^2 r^2 (R_L + R_c) \quad (7)$$

where  $r$  is the discharge tube radius. The left hand side is the electrical input power per cm and the right hand side is the output power per cm as determined by the thermal conduction and the line and continuum radiation, given by  $R_L$  and  $R_C$ , respectively (see Fig. 10). By assuming a nearly isothermal, optically thin discharge, the left hand side becomes

$$\pi E^2 r^2 \quad (8)$$

The temperature gradient  $dT/dr$  can now be evaluated by using the calculated value of 9.2 volts/cm for  $E$  and using Figs. 3, 4, and 10 to obtain the other unknown values at 9,200°K. This value of the temperature gradient is now assumed constant and the conductivities are used for 8,530°K (the core temperature determined by a comparison of the calculated line profiles to the measured profile). The value of  $R_L$  at 8,530°K is determined from Figs. 9 and 10, and the value of  $R_C$  is determined from Eqs. 7 and 8. In other words, the electrical input power is held constant but the temperature of the discharge is lowered from 9,200°K to 8,530°K. This temperature decrease lowers the conduction and line radiation losses and consequently the true continuum radiation loss must increase to exactly cancel these decreased losses. The result is that the continuum radiation at 8,530°K is approximately  $99.4 \text{ watts cm}^{-3} \text{ ster}^{-1}$  which is nine times as much continuum radiation as given by Figs. 9 and 10, although the total radiation has only been reduced from 165 to 155  $\text{watts cm}^{-3} \text{ ster}^{-1}$ . Thus the continuum radiation at 8,530°K is 64% of the total radiation. This compares favorably with the 55% calculated for the krypton discharge and leads us to believe that the continuum radiation calculated for the krypton discharge is about right.

In the determination of the temperature profiles and electrical characteristics, the discharge is assumed to be optically thin. The effect of this assumption is to increase the voltage gradient value at a given current. This increase can be seen in the xenon discharge by assuming an isothermal temperature profile. Then

$$E = IR = IK/\sigma \quad (9)$$

where E and I are given in Fig. 11 and  $\sigma$  is the electrical conductivity given in Fig. 3. The constant K is determined to be 6.44 by setting I equal to 40 amp and using the E and  $\sigma$  values appropriate for 9,200°K. If the electrical conductivity is now changed to the value for 8,530°K (the core temperature determined by a comparison of the calculated line profiles to the measured profile), the voltage gradient is determined from Eq. (7) to be 12.27 volts/cm.

On the other hand, the krypton discharge is 23% optically thick and the calculated voltage gradient is 8% too high. Since the xenon discharge is 80% optically thick its voltage gradient should be (80/23) 8% too high. In other words the calculated voltage gradient should be 12.27 volts/cm.

The above two calculations give the same result and show that the difference between the calculated and measured voltage gradients increases in direct proportion to the optical thickness of the discharge. However, the calculated core temperature is independent of the optical thickness. These results also show that the -4% agreement between the calculated and measured voltage gradients for xenon is fortuitous and should be 27.8%.

The purpose of the previous discussion is to understand the present limitations of the calculations. Thus the errors have been discussed and estimated. It is consequently very easy to be too concerned about the limitations and overlook the successes. We believe that the theoretical results are so good for the purpose of evaluating relative pump efficiencies that the original calculations of Section 2.1 are used without modification. In fact, despite the errors, we believe that the best spectral overlap calculations will be done with calculated rather than experimental spectra because the calculated spectra are better resolved. This increased resolution is particularly important for line emitting arc discharges pumping a line absorbing laser rod such as the rare earth activated lasers.

### 3. LASER ABSORPTION SPECTRA

The necessary input information to obtain the pumping efficiency of a lamp is its spectral emittance and the excitation spectrum of the lasing medium. The lasing media we wish to consider are  $\text{Nd:Y}_3\text{Al}_5\text{O}_{12}$  (Nd:YAG) and  $\text{Cr:Al}_2\text{O}_3$  (Ruby). The absorption spectra of these crystals which closely follow the excitation spectra in the region of interest can be obtained by experimental measurement. This data must then be converted from a chart recorder to computer data cards. This operation is easily done for ruby since the absorption spectrum varies slowly with wavelength and will be included in a later chapter.

The Nd:YAG absorption spectrum consists of a large number of narrow lines and requires considerably more data points to describe it compared to ruby. However, prior to this contract, we have developed a program which requires knowing only a few data points per line to calculate and describe the spectrum. The general interpolation technique used is called GOOP, and for determining the YAG spectrum it is called YAGGOP. The YAGGOP program is complete and available for use.<sup>1</sup> The general technique of YAGGOP is to fit a series of Lorentzian profiles to the measured spectrum. Each Lorentzian profile is completely specified by its center frequency, peak value and width at half the peak value. Prior to this contract the Nd:YAG absorption spectrum shown in Fig. 24 was fitted by YAGGOP. Fifty-one Lorentzian profiles are needed to reproduce the measured spectrum. In other words, 153 specified variables give a complete mathematical description of the absorption spectrum. The details of this fit are given in Ref. 1 and will not be described here.

#### 4. SYSTEM EVALUATION

How well does a particular lamp pump a given laser rod? This is a question of considerable interest which we will attempt to answer in this chapter. In particular the efficiencies of the potassium-mercury, tungsten, krypton, and xenon lamps specified in Chapter 2 will be evaluated for pumping slab lasers of different thicknesses.

The system which is considered is a simplification of actual laser systems. The lamp is considered to be an infinitely long cylinder whose light is focused by an idealized optical system onto an infinite laser slab of thickness  $t$ . The lamp light is transmitted to the slab through a perfectly transparent medium and perpendicularly strikes the slab with the same emittance at which it left the lamp. The light which enters the slab is then absorbed or transmitted. The absorbed light pumps the laser ion whereas the transmitted light is lost to the system. Although this simple system is obviously different than real laser system it will be shown that it produces excellent quantitative results.

##### 4.1 Lamp Efficiency

The lamp efficiency is defined here as the percentage of electrical power into the lamp which is emitted in the 5,000 to 10,000 Å wavelength region which includes all the useful absorption bands of Nd:YAG. The input power per unit surface area for the four lamps under consideration was given in Chapter 2. The output power per  $\text{cm}^2$  is obtained by numerically integrating the spectral emittance over the 5,000 to 10,000 Å region. This integration has an accuracy of better than 5% and shows that the lamp efficiencies are 67%, 36%, 35%, and 14% for the potassium-mercury, tungsten, xenon, and krypton lamps, respectively. Note that the xenon lamp is 2.5 times more efficient than the krypton lamp. These lamp efficiencies do not include electrode



losses which are normally about 15% of the input power to a 3" lamp and can be included in the above efficiencies by a multiplication factor of 0.87.

The efficiency of the simple system described in the beginning of this chapter is particularly interesting if the slab is 0.7% Nd:YAG. This laser material is a line absorber and is widely used in laser systems. The former property makes it a difficult test of the lamp emission calculations.

#### 4.2 Slab Efficiency

The slab efficiency is defined here as the percentage of the power density (watts/cm<sup>2</sup>) incident on the slab which is emitted at the fluorescing wavelength of 1.064  $\mu$ . In other words, the slab efficiency measures the effectiveness of the slab in absorbing incident energy and transforming this absorbed energy to useful emission. The power density incident on the slab was calculated in the last subsection. The power density emitted at 1.064  $\mu$  is determined by the spectral overlap:

$$S = \int_{\nu_1}^{\nu_2} I_\lambda(\nu) [1 - \exp(-\alpha(\nu)t)] (\nu_0/\nu) Q(\nu) d\nu \quad (10)$$

where  $I_\lambda$  is the spectral emittance of the lamp,  $\alpha$  is the spectral absorptivity of the slab and  $Q$  is the quantum efficiency of the laser material. The  $\nu_0$  is the fluorescent frequency corresponding to 1.064  $\mu$ ;  $\nu_1$  and  $\nu_2$  are the frequencies corresponding to wavelength of 1.0 and 0.5  $\mu$ , the wavelength region of the lamp emission. The quantum efficiency is assumed to be unity. The spectral emittance was calculated in Chapter 2, and the slab absorptivity was obtained as described in Chapter 3. Thus everything in Eq. (10) is specified and the integrand can be numerically integrated. Before doing the integration, however, it is interesting to study the integrand,  $I$ , for various values of slab thickness.

The spectral overlap integrand for the tungsten lamp is shown in Fig. 25. As the thickness is increased the broad emission bands from the tungsten are increasing absorbed by the unsaturated absorption lines. As the absorption lines become saturated, the spectral distribution of the tungsten lamp becomes prominent and is very evident in Fig. 25f.

It would be too bulky to include all the spectral overlap integrand plots. Therefore, only the results for a 1.2 cm slab thickness are shown in Figs. 26, 27 and 28 for the remaining three lamps. These plots clearly show that most of the spectral overlap contribution is from above 7,000 Å. The line emission of these three lamps gives a more jagged appearance to the plots than present in the tungsten plots. Xenon obviously has the worst spectral overlap.

The spectral overlap integrand is numerically integrated to an accuracy of at least 5%, and the slab efficiency is obtained by dividing by the incident power density. The results are shown in Fig. 29. The krypton lamp clearly has the best spectral match with a Nd:YAG slab.

#### 4.3 Pump Efficiency

The pump efficiency is defined here as the percentages of the electrical power density into the lamp (neglecting electrode losses) which is emitted by the slab at the fluorescing wavelength of  $1.064 \mu$ . Thus the pump efficiency measures the effectiveness of the slab laser system. Since the slab properties remain constant as the optical pump is changed, it is really a measure of the optical pump effectiveness and explains the term "pump" efficiency.

The pump efficiency is the product of the lamp efficiency and the slab efficiency and is the final goal of these calculations since it is the best method of evaluating slab laser systems. All the required numbers have been calculated in the previous subsections and the pump efficiencies are plotted in Fig. 30. The most efficient pump by far is the potassium-mercury lamp. This is a result of being the most efficient lamp of the four and having a very good spectral overlap,

although the spectral overlap of the tungsten lamp is considerably better than that of the xenon lamp. The krypton lamp is quite inefficient but the spectral overlap is so large that the pump efficiency is very close to that of the tungsten lamp.

A comparison of the krypton and tungsten pump efficiencies is rather interesting. The tungsten pump is more efficient for slabs thinner than 1.2 cm or thicker than 2.4 cm. The krypton pump is very slightly more efficient in the intermediate range of thicknesses. This behavior demonstrates how the absorption saturation of individual lines can change the relative efficiencies of two pumps with pump efficiencies which are very close to each other.

These results can be compared with experimental laser measurements. Appendix 1 shows our published results on comparing tungsten, krypton, and xenon lamps for pumping a 5 mm diameter, 50 mm long Nd:YAG laser rod. Figure 31 includes these results and also shows some more recent work on potassium-mercury lamps. These lamps appear to be very promising as Nd:YAG pumps. Currently they must operate in a vacuum to prevent atmospheric attack of the Nb end caps which operate at temperatures in excess of 700°C. The quartz vacuum jacket presently used degrades the coupling efficiency to the laser rod and the vacuum operation considerably decreases the input power to the lamp since the sapphire walls of the lamp are cooled only by radiation. By eliminating the vacuum jacket and protecting the end caps through coatings or other means we have predicted previous to this contract the experimental results designated as air-cooled K-Hg lamp.

Although the slope efficiencies are easily found from Fig. 31, the relationship between the rod diameter and the slab thickness must still be determined in order to compare the measured and calculated efficiencies. An approximation can be made by equating the slab thickness to the effective chord length in the rod,  $\bar{c}$ :

$$t = \bar{c}D \quad (11a)$$

where  $D$  is the ratio of the activator doping in the rod to the doping in the slab. The effective chord length in a cylindrical rod of diameter  $d$  is shown in Appendix 2 to be given by

$$\bar{c} = \left( \frac{4.7}{d + 6.44} + 0.27 \right) d \quad (11b)$$

This calculation does not include the cavity coupling efficiency and assumes a Lambertian distribution of the light intensity in the rod. For the 1.3% doped, 0.5 x 5 cm rod used for the experimental measurements of Fig. 31, Eqs. (11a) and (11b) give an equivalent slab thickness of 0.84 cm (see Appendix 1). The experimental slope efficiencies are included in Fig. 30 at this slab thickness. The agreement between the calculated and measured relative pump efficiencies is excellent. This agreement is rather surprising when all the approximations are considered.

The comparison for the tungsten pump only tests the spectral overlap calculation and the rod to slab thickness transformation since a measured lamp spectrum was used. The agreement at the sharply rising curve for the potassium-mercury pump is good considering the crude "measured" value. This comparison is another test for the spectral overlap and rod to slab transformation calculations.

The calculated xenon pump efficiency is too low and must be attributed to the low value calculated for the continuum radiation. The calculated value can be adjusted by reducing the total lamp radiation from 165 to 155 watts  $\text{cm}^{-3} \text{ster}^{-1}$  and by assuming that 64% of the radiation is continuum (see Section 2.3). The lamp efficiency is thus reduced from 35.2% to 33.1%. Since the radiation contributing most to the spectral overlap is the continuum radiation, the slab efficiency should be close to that for tungsten. The adjusted xenon pump efficiency is 2.5% which is in good agreement with the measured laser efficiency of 3.1%.

The real test for the theoretical calculations is given by a comparison of the calculated and measured results for the krypton pump. The continuum calculation is good and no adjustments need to be made. The measured value of 3.7% is 30% higher than the calculated value of 2.6%. This agreement is excellent in view of the lengthy ab initio calculation. This is the first time such a calculation of this type has succeeded!

#### 4.4 Activator Efficiency

Although the electrical input energy and the pump efficiency is all that is normally needed, another efficiency is interesting to know. This additional efficiency will be called here the activator efficiency and is the percentage of time spent fluorescing by an average activator ion. If the slab emits  $R$  watts  $\text{cm}^{-2}$ , each activator emits  $R/tn$  watts where  $n$  is the number of activator ions per  $\text{cm}^3$ . Each emitted photon has an energy of  $hc/\lambda_0$  where  $\lambda_0$  is  $1.064 \times 10^{-4}$  cm for Nd:YAG. Thus the number of photons emitted per second by the activator ion is given by

$$N = (R/tn)(\lambda_0/hc) \quad (12)$$

The fraction of time spent by the activator ion in the fluorescing process is simply  $N$  times the lifetime of the excited activator ion,  $\tau$ . The activator efficiency is thus

$$E_a = N\tau \quad (13)$$

The lifetime has been measured at 230  $\mu\text{sec}$ .<sup>28</sup> Equation (13) can then be evaluated and the results are plotted in Fig. 32 (Note that the input power densities have been normalized). The low values show that the use of the Nd ion is surprisingly inefficient because an activator never spends more than about 0.06% of its time in fluorescence.

#### 4.5 Discussion

The important results in this chapter are summarized in Table VII. The agreement between the relative experimental laser efficiencies and the relative calculated pump efficiencies is excellent! Ranked in order of decreasing lamp efficiency, the four lamps are potassium-mercury, tungsten, xenon and krypton. The ranking for the greatest slab efficiency is krypton, potassium-mercury, tungsten, and xenon whereas the ranking for the largest pump efficiency is potassium-mercury, tungsten, krypton, and xenon. These rankings clearly indicate the interplay of the lamp and slab efficiencies to give the pump efficiency.

The pump efficiencies as a function of thickness are important but it would be more convenient if pumps could be ranked by a single number. One possible system would be to use the activator efficiency at zero thickness. This efficiency is finite and is independent of the slab thickness. It is given in Table VII in the  $E_0$  column. This ranking system which is independent of slab thickness would rank the pumps in descending order as the potassium-mercury, tungsten, krypton, and xenon pumps.

## 5. SUMMARY

The emission spectra of a xenon and a krypton arc discharge have been measured on this contract, and the absorption spectra of Nd:YAG and ruby were measured previous to this contract. The xenon and krypton arc discharge spectra have been calculated from theory. The line spectra (which comprise about 50% of the total emission) agree so well with the measured spectra that one cannot determine which is the more accurate, although the calculated line profiles appear to be more accurate than the measured line profiles (due to the low resolving power of the spectrometer). The calculated continua only agree with the measured continua to within a factor of two. In order to save time and money, available measured emission spectra of a tungsten and a potassium-mercury lamp have been used.

The overlap between the emission spectra of these four lamps and the Nd:YAG absorption spectrum has been calculated as a function of the slab laser thickness. Combined with the calculated lamp efficiencies, the spectral overlap yields the system efficiency for an optically pumped slab laser. A cylindrical rod laser in a cavity was approximately transformed to an equivalent slab thickness of a fixed thickness and thus actual laser system efficiencies were calculated.

The agreement between the theoretical and measured relative laser efficiencies for the four lamps is excellent. This agreement is remarkable because the calculations for the krypton and xenon pumps only used: (1) lamp dimensions, (2) lamp gas, (3) lamp pressure and current, (4) laser rod absorption spectra, and (5) laser rod dimensions and activator doping as the necessary laser system variables which have to be experimentally measured. Therefore, for the

first time it has been shown that relative laser system efficiencies can be calculated from very basic laser system parameters. The results show that the potassium-mercury lamp is four times more efficient in pumping Nd:YAG for all rod diameters of interest than the tungsten and krypton lamps which are slightly better than the xenon lamp. The calculations clearly demonstrate how the theory can be applied to evaluate simple optical pumps for a given laser rod, thereby bypassing costly and lengthy experimental measurements.



**BLANK PAGE**

## **RUBY LASERS**

## 6. INTRODUCTION

The ruby laser was the first successful laser<sup>29,30</sup> and is still not completely understood. Since it is a three-level laser, more than 50% of the ground state chromium ions must be excited before lasing can occur. This requirement necessitates a very powerful flash lamp which can invert the population before the excited ions can return to the ground state via spontaneous emission (fluorescence).

The required 50% inversion automatically decreases the laser system efficiency. However, theoretical calculations of this and other losses in ruby amplifiers predict laser efficiencies which are usually an order of magnitude higher than the measured values. This discrepancy is still unexplained although many possible explanations have been proposed.

One proposed explanation is that the flash lamp is not efficiently pumping the ruby. This special report investigates this problem by calculating the pumping efficiency for fluorescence. It is found that the pumping efficiency for fluorescence is quite high at the peak of the flash lamp pulse. In fact, it is found that a 1.27 cm diameter ruby amplifier should have an overall efficiency of 6% based on pumping considerations alone. Depopulation of the  ${}^2E$  energy level by excited state absorption would decrease the efficiency by a small amount but excessive bleaching of the ruby rod or premature arrival of the ruby oscillator pulse appear to be the best explanations for the measured low amplifier efficiencies.

## 7. LAMP EMISSION SPECTRUM

The necessary input information to obtain the pumping efficiency of a lamp for a given laser material is the spectral emittance of the lamp and the excitation spectrum of the lasing medium. The excitation spectrum of ruby will be considered in the next chapter, whereas the spectral emittance of a xenon flash lamp is considered in this chapter.

The spectral radiance of a typical xenon flash lamp has been measured by Church et al<sup>31</sup> and is shown in Figure 33. The 12300 °K black body radiance is also shown for comparison. The xenon radiation is clearly continuum radiation. A comparison of the calculated radiance and the measured radiance again illustrates the inadequacy of the continuum radiation theory. For the following calculations the measured radiance is always used.

Although Figure 33 shows the peak radiance from the flash lamp, the light pulse is actually very time dependent. This is clearly seen in Figure 34. The calculation in this report neglects this time dependence and simply uses the peak radiance values. This is a good assumption since by employing pulse forming techniques nearly rectangular pulses may be obtained.

Efficiency calculations require the electrical power into the lamp. This xenon lamp, at its peak radiance, operated at a current density of 4480 amps/cm<sup>2</sup> with an electrical conductivity of 63 mho/cm. The electrical input power is thus  $1.0 \times 10^4$  watts per cm<sup>2</sup> of surface area. This calculation assumes that the voltage drop at the electrodes is negligible.

Although the radiance is measured, the emittance is required for the efficiency calculations. The emittance is obtained to a good approximation by multiplying the radiance by  $\pi$  steradians, the value for a perfect Lambertian radiator.

## 8. RUBY ABSORPTION SPECTRA

The absorption spectra of ruby closely follow the excitation spectra in the region of interest and are easily measured with a Cary spectrophotometer. The results of Maiman<sup>32</sup> are shown in Figure 35. Since ruby is anisotropic, two absorption spectra are shown, one for light propagating parallel and one for light propagating perpendicular to the c-axis of the ruby crystal. The chromium concentration was determined<sup>32</sup> by chemical analysis to be 0.0515 weight percent of  $\text{Cr}_2\text{O}_3:\text{Al}_2\text{O}_3$  which corresponds to a chromium ion density of  $1.62 \times 10^{19}$  ions/cm<sup>3</sup>. The absorption data for the R lines are shown in Figure 35 but were not used in the present calculations. Excited state absorption<sup>33,34</sup> was also not considered; however, this is expected to cause no major error.

A comparison of the two spectra in Figure 35 indicates that light propagating parallel to the c-axis should pump the ruby crystal more effectively than light propagating perpendicular to the c-axis. We will show later that this is indeed the case, although the difference is not as large as one might expect from the absorption spectra.

The absorption coefficient given in Figure 35 is for small amplitude pumping when virtually all the absorbing ions are in the ground state. However, under hard pumping at least half of the ions are in the excited state and unavailable for excitation. In this case, the absorption coefficients are half the values shown. During long-pulse laser operation, stimulated emission automatically keeps the ground state about one-half filled and therefore the efficiencies are calculated from absorption coefficients which are one-half the values given in Figure 35.

## 9. SYSTEM EVALUATION

How well does the xenon lamp pump the ruby? This is the basic question which will be examined in this chapter. However, only the fluorescence pumping efficiency is calculated; the details of the lasing process which could modify this efficiency are not considered.

The model used is a simplification of the actual laser system. It is thought to be a good approximation to the "first pass" in a focusing elliptical or spherical pumping cavity. The lamp is considered to be an infinitely long cylinder whose radiation impinges onto an infinitely long ruby slab of thickness  $t$ . The lamp radiation is transmitted to the slab through a perfectly transparent medium and perpendicularly strikes the ruby slab with the same emittance at which it left the lamp. The light which enters the slab is then absorbed or transmitted. The absorbed light pumps the chromium ions whereas the transmitted light is lost to the system. Although this simple model is obviously different than the real laser system, it produced excellent results for the pumping of Nd:YAG and should be equally applicable to the pumping of ruby.

### 9.1 Lamp Efficiency

The lamp efficiency is defined here as the percentage of electrical power into the lamp which is emitted in the 3000 to 7000 Å wavelength region which includes all the useful absorption bands of ruby. The input power per unit surface area for the xenon lamp was calculated in Chapter 7. The output power per unit surface area is obtained by numerically integrating the spectral emittance over the 3000 to 7000 Å region. This integration has an accuracy of better than 5% and shows that the xenon lamp efficiency is 36%. This calculation assumes that the electrode losses are negligible.

## 9.2 Slab Efficiency

The slab efficiency is defined here as the percentage of the power density (watts/cm<sup>2</sup>) incident on the slab which is emitted as ruby fluorescence. In other words, the slab efficiency measures the effectiveness of the slab in absorbing incident energy and transforming this absorbed energy into useful emission. The power density incident on the slab was calculated in the last section. The power density emitted at 6943 Å (assuming that all the ruby fluorescence takes place at this wavelength) is determined by the spectral overlap:

$$S = \int_{\nu_1}^{\nu_2} I_l(\nu) [1 - \exp(-\alpha(\nu)t)] (\nu_0/\nu) Q(\nu) d\nu \quad (10)$$

where  $I_l$  is the spectral emittance of the lamp,  $\alpha$  is the spectral absorptivity of the ruby slab and  $Q$  is the quantum efficiency of the ruby. As explained in Chapter 8, the absorptivity used in Equation (10) is one-half of the values shown in Figure 35. The  $\nu_0$  is the fluorescent frequency corresponding to 6943 Å;  $\nu_1$  and  $\nu_2$  are the frequencies corresponding to wavelengths of 7000 and 3000 Å, the effective wavelength region of lamp emission. The quantum efficiency has been measured by Maiman<sup>32</sup> and is shown in Figure 36 (although the results of Maiman<sup>31,32</sup> are rather old, they are in a more convenient form to use and do not significantly differ from more recent results<sup>33,34</sup>). The power efficiency curve shown in this figure is the  $\nu_0/\nu$  ratio times the quantum efficiency. Thus everything in the integrand is specified.

The spectral overlap integrand is numerically integrated to an accuracy of at least 5%, and the slab efficiency is obtained by dividing by the incident power density. The results are shown in Figure 37. As expected from the absorption data, light propagating parallel to the ruby c-axis gives better slab efficiencies.

### 9.3 Pump Efficiency

The pump efficiency is defined here as the percentage of the electrical power density into the lamp (neglecting electrode losses) which is emitted by the slab at the fluorescing wavelength of 6943 Å (i.e., the product of lamp and slab efficiency). Thus the pump efficiency measures the fluorescence effectiveness of the slab laser system. Since the slab properties remain constant as the optical pump is changed, it is really a measure of the optical pump effectiveness and explains the term "pump" efficiency.

All the required numbers have been calculated in the previous sections and the pump efficiencies are plotted in Figure 38. It was shown in Section 4.3 that, to a good approximation, the diameter of a laser rod may be equated to about the same value of slab thickness. Consequently, the abscissas of Figures 5 and 5 may be considered as laser rod diameters. For a rod with the same diameter as the xenon lamp (1.27 cm) the pumping efficiency is about 6%. It is then apparent that the pumping efficiency of ruby is quite high and does not explain the measured low ruby laser efficiencies<sup>35</sup>.

### 9.4 Activator Efficiency

Although the electrical input energy and the pump efficiency are all that are normally needed, another efficiency is needed for lasers which are pumped hard. This additional efficiency will be called here the activator efficiency and is the percentage of time spent in the excited state by an average chromium ion. If the ruby slab emits  $R$  watts per unit surface area, each chromium ion emits  $R/tn$  watts where  $n$  is the number of activator ions per  $\text{cm}^3$  and  $t$  is the slab thickness. Each emitted photon has an energy of  $hc/\lambda_0$  where  $\lambda_0$  is taken as 6943 Å. Thus the number of photons emitted per second by each chromium ion is approximately given by

$$N = (R/tn) (\lambda_0/hc) \quad (12)$$



Equation (12) is slightly different for a laser rod. If we take the rod diameter  $d$  to be the same as the slab thickness (this is probably accurate to within 10%), each chromium ion emits  $4(\pi d \ell)R/(\pi d^2 \ell)n$  watts, where  $\ell$  is the length of the rod. In other words, each chromium ion emits  $4R/dn$  watts and Equation (12) becomes

$$N = (4R/dn) (\lambda_0/hc) \quad (12a)$$

for a ruby rod. This expression assumes that no pump light is absorbed by the ends of the rod.

The fraction of time spent by the activator ion in the excited state is simply  $N$  times the lifetime of the excited chromium ion,  $\tau$ . The activator efficiency is thus

$$E_a = N\tau \quad (13)$$

The measured lifetime at low pumping levels is 3.0 msec at 300°K.<sup>32</sup> At this lifetime the calculated activator efficiency varies with slab thickness from 150% to 1300%! Since the activator efficiency can never exceed 100%, it is clear that the activator efficiency cannot be calculated as described. The problem is the excited-state lifetime. At low pumping levels the measured values are appropriate, but at high pumping levels many excited ions will go to the ground state via stimulated emission. If stimulated emission is prevented, the power absorbed and reemitted by the ruby decreases due to bleaching. By assuming that stimulated emission takes place, the number of stimulated emission transitions is sufficient to lower the average excited-state lifetime. This lowered lifetime due to stimulated emission can be calculated from Equation (13) by setting the activator efficiency at the desired value of 50%. The results are plotted in Figure 39, which shows that the lifetime of a 1.27 cm diameter ruby rod is lowered from 30 msec at low pumping levels to about 120  $\mu$  sec at the high pumping levels of the xenon flash lamp used for these calculations.

## 10. SUMMARY

The calculated pump efficiency of about 6% for a 1.27 cm diameter ruby rod is considerably higher than measured laser efficiencies, particularly in oscillator-amplifier combinations.<sup>35</sup> One possible cause for this difference is depopulation of the  $^2E$  state (see Figure 40) via transitions to the charge transfer band.<sup>36,37</sup> This transition occurs at 3600 Å and decreases the pump efficiency. However, the xenon flash lamp radiance shown in Figure 33 decreases in this wavelength region, and can be filtered out without changing the pump efficiency appreciably. Depopulation should consequently have a measurable but small effect on the pump efficiency.

Another possible source of the discrepancy between calculated pump efficiencies and laser efficiencies is the time dependence of the pump pulse. Figure 34 shows the time history of one xenon line and Figure 40 shows the energy level diagram of ruby with measured lifetimes. As the pulse radiance increases, the pump spectrum changes and becomes a more efficient pump. Thus, the initial part of the pump pulse decreases the total pump efficiency. This effect is also present during the final stages of the pulse when the pump radiance is decreasing. This loss can be minimized by pulse forming networks.

The above arguments hold for oscillators as well as amplifiers. Amplifiers have an additional mechanism for loss of efficiency which we believe could be very large. Above it was assumed that stimulated emission kept the ground state population at 50%. In oscillators this occurs automatically, but in amplifiers this condition depends on the proper timing of the input laser energy. If the input laser power arrives too soon, it will be absorbed by the amplifier rod rather than amplified. If it arrives too late, the pump pulse will have bleached the rod to the point where the pump radiation is no longer being absorbed by the rod. This problem can only be accurately analyzed by a time-dependent study.

A time-dependent analysis of lamp emission, excited populations, absorption coefficients, quantum efficiencies, and pump efficiencies would give a better understanding of ruby amplifiers and perhaps lead to increased efficiencies.

RADIAL WAVE FUNCTIONS

## 11. PARAMETER FITTING FROM SLATER INTEGRALS

The objective of this work phase is to determine atomic radial wave functions by fitting a power series expansion with parametric coefficients of the radial wave function to experimentally determined Slater integrals of the radial wave functions. These wave functions can then be used to calculate the transition probabilities required in the arc discharge emission calculations. The parameter fitting (PF) technique has the advantage of being independent of the complex electronic shell structure. This independence is in contrast to the conventional methods such as the Thomas-Fermi<sup>4</sup> and Bates and Damgaard coulomb<sup>18</sup> approximations which only work for simple shells of one or two electrons. We consequently expect PF to succeed where all other methods fail.

To initiate PF the constraints must be enumerated which a radial wave function must satisfy, and reasonable forms for the PF power series expansion with fitting parameters must be formulated. The constraints and expansions are given in the next two sections. The selection of the numerical procedure to adjust the fitting parameters to satisfy the constraints and reproduce the experimentally determined Slater integrals is a critical selection which forms the heart of the PF technique. Two iterative numerical procedures are examined in Section 11.3. The initiation of both procedures requires an approximation of the fitting parameters. This approximation is best achieved with the aid of screening constants which are discussed in Section 11.4. Finally, the PF technique must be proven in a case where the radial wave function is known. The Hartree-Fock calculations<sup>38</sup> of the Cu 4s Slater Integrals and radial wave function provide an excellent test case.

## 11.1 PF CONSTRAINTS

An atomic wave function is usually given by

$$|n\ell m\rangle = r^{-1} P_{n\ell}(r) Y_{\ell m}(\theta, \phi) \quad (14)$$

where  $P_{n\ell}(r)$  is the normalized radial wave function to which PF will be applied and is given below in atomic units. The radial wave function must satisfy the following general requirements.

As  $r$  approaches zero Mann<sup>38</sup> has shown that

$$P_{n\ell}(r) \xrightarrow{r \rightarrow 0} r^{\ell+1} \left(1 - \frac{Z}{\ell+1} r\right) \quad (15)$$

where  $Z$  is the nuclear charge. On the other hand, as  $r$  approaches infinity Handy et al.<sup>39</sup> have shown that the asymptotic form of the radial wave function is

$$P_{n\ell}(r) \xrightarrow{r \rightarrow \infty} f(\vec{r}) \exp(-(-E_{n'\ell'})^{1/2} r) \quad (16)$$

where  $f(\vec{r})$  is a function of  $\vec{r}$  which does not have as critical dependence on  $r$  as the exponential. The  $E_{n'\ell'}$  (whose value is negative) is the Hartree-Fock binding energy<sup>38</sup> of the least bound electron of the atom, i.e., not necessarily of the electron under consideration. The constraints in Eq. (15) and (16) result from the Hartree-Fock Equation and may not be physically correct. However, because the Hartree-Fock formulation is so extensively used and generally gives good results, these constraints will be accepted as valid for PF.

Three other common constraints are the number of nodes and orthonormality. The number of nodes, excluding end values, is given by  $n - \ell - 1$ . This condition will be used although certain wave functions

are more accurately obtained when this condition is dropped. The orthonormality condition:

$$\int_0^{\infty} P_{nl}(r) P_{n'l}(r) dr = \delta_{nn'} \quad (17)$$

is one of mathematical convenience.

Of the above constraints, only the asymptotic form given in Eq. (16) poses any problem in principle. The  $f(\vec{r})$  is unknown as is the binding energy (except for the ground states of atoms).<sup>38</sup> Consequently, the implementation of this constraint requires an approximate approach.

The  $f(\vec{r})$  will be guessed based on our experience. The choice of  $f(\vec{r})$  should not be critical because (a) it is only pertinent in the extreme outer portion of the wave function, (b) its  $r$  dependence is less than that of the exponential, and (c) any error in  $f(\vec{r})$  will be largely ameliorated by the fitting of the adjustable parameters to reproduce the measured Slater integrals.

The determination of the binding energy is more important since it appears in the exponential. Fortunately, the binding energy is valuable for other purposes and approximations for its value have already been devised. The binding energy is given by

$$E_{nl} = -(Z - \sigma_{nl})^2/n^2 \quad (18)$$

where  $n$  is the principal quantum number and  $\sigma$  is a screening constant. Thus  $Z - \sigma_{nl}$  is the effective nuclear charge as seen by an electron in the  $(nl)$ th orbit. Methods for estimating the screening constant have been developed<sup>40,41</sup> and tables of their values have appeared.<sup>42</sup>

## 11.2 PF BASIS SETS

The choice of a basis set of functions into which the radial wave function can be expanded is a rather arbitrary choice. Except for trivial problems the true analytic form (if one exists) of the radial wave function is unknown. Approximate analytic forms are usually obtained by assuming an analytic form with variational parameters and then varying these parameters until the energy is minimized. These variational techniques are very dependent upon a good choice for the analytic form. On the other hand, the least-squares fit of an analytic function with fitting parameters to a numerical function is not very dependent upon the choice of the analytic form (this fact has often allowed experimentalists to fit their data to wrong theories, and vice versa). This advantage of PF will tend to be offset by the large smoothing of the integrand e.g., the radial wave functions, by the double integrals in the Slater integrals. In other words, integrals tend to be independent of the detailed integrand structure and this independence allows poor radial wave functions to give good Slater integrals. That is why constraints on the analytic radial wave function are imperative.

Since the choice of the PF basis set is somewhat arbitrary, it would be best to investigate several sets so as to obtain the best one. The five best known sets are hydrogenic orbitals,<sup>43</sup> Slater orbitals,<sup>44</sup> Boys orbitals,<sup>45</sup> Bessel orbitals<sup>46</sup> and Gaussian orbitals.<sup>46</sup> Economic realities dictate that only one basis set be investigated (at least until PF becomes a proven and useful tool). The Slater orbitals are chosen because they satisfy constraints (15) and (16), are very flexible, and are the most commonly used basis set. The PF expansion is they written as



$$P_{nl}(r) = AP_{nl}^{(o)}(ax) + \sum_{j=l}^{n-1} B_j P_{nj}^{(o)}(b_j x) \quad (19)$$

$$+ C P_{n,n-1}^{(o)}(cx)$$

where, for Slater orbitals

$$P_{nl}^{(o)}(ar) = [2a/(2l+2)!] (2ar)^{l+1} \exp(-ar) \quad (20)$$

This PF expansion has  $A$ ,  $B_j$ ,  $C$ ,  $a$ ,  $b_j$ , and  $c$  for the fitting parameters. As stated the fitting parameters always occur in pairs, even though there frequently are an odd number of Slater integrals which can be used for fitting. Whenever this situation exists the value of  $c$  will be approximated by Eq. (18). Since only Slater orbitals are considered here, these fitting parameters will be called the Slater parameters.

### 11.3 NUMERICAL PROCEDURES

The numerical evaluation of integrals such as the Slater integrals and those in Eq. (17) is a mundane, but important numerical problem since these integrals are evaluated thousands of times in a long PF iteration. The most commonly used technique is to use a variable step size Simpson's rule. Herman and Skillman<sup>47</sup> and Mann<sup>48</sup> tabulate their wave functions in a step size which starts from 0.01 for  $x$  between 0.00 and 0.10 and is doubled for succeeding ranges until 1.28 is the largest step size used for large values of  $x$ . It is important to note that the variable which is usually tabulated, and used as the variable of integration is not  $r$ , but  $x$ , which is a Thomas-Fermi normalized radius. The relationship between the two variables is given by

$$r = (9\pi^2/128 Z)^{1/3} x = Kx \quad (21)$$

where  $Z$  is the nuclear charge.

Although Simpson's rule is the most convenient integration method to use, it is neither the fastest nor the most accurate. The trapezoidal rule is faster and only slightly less accurate. However, the best integration procedure for integrals which contain radial wave functions is probably Laguerre integration of the Gaussian type:<sup>49</sup>

$$\int_0^\infty f(x) dx \approx \sum_{k=1}^n w_k f(x_k) \quad (22)$$

The abscissa  $x_k$  are fixed at the zeros of the  $n^{\text{th}}$  order Laguerre polynomial and the weights  $w_k$  are determined from the values of the  $(n+1)^{\text{th}}$  order Laguerre polynomial at the  $x_k$  values. The weights and abscissa are tabulated in the literature for many values of  $n$ .<sup>50</sup> It is

easily shown that when  $f(x)$  contains radial wave functions, the Laguerre integration rapidly converges to the correct value as  $n$  increases without limit.

A comparison of these numerical integration methods is given in Tables VIII and IX where the integrals are between the Cu 4s electron and inner shell electrons. The true values of the integrals have been evaluated by Mann.<sup>38</sup> Simpson's rule with 100 points is the most accurate method, but extremely slow. The trapezoidal rule is slightly faster and slightly less accurate. The 15-point Laguerre integration is about fifty times faster, but a little too inaccurate for most work. The 48-point Laguerre integration is five times faster and as accurate as Simpson's rule integration.

It is clear that Laguerre integration is the best method for PF, but the application of Laguerre integration requires more facts. The Hartree-Fock radial wave functions which appear in the  $f(x)$  of Eq. (22) are evaluated at the  $x_k$  values by six-point Lagrange interpolation. The upper limit of the integral cannot practically be infinite, but must be some value of  $x$  beyond which the integrand must be negligible. For the 15-point integration the upper limit is simply taken to be  $x_{15}$ , i.e., 48.03. For the 48-point integration the upper limit is the last tabulated value of the radial wave function which is larger than 0.0001. For the Cu 4s radial wave function this upper limit is 66.46.

The selection of the numerical integration technique now allows the iterative PF method to be selected. A conventional problem in physics is to fit via least squares parameterized functions to a given curve. The PF problem is different in that the parameterized functions are first integrated and the integrals are fitted to known values. This difference poses a problem as to which iterative procedure should be used. A Newton's method for systems of simultaneous non-linear equations and a Direct Search method have been tried in which the sum of the squares of the differences between the known and calculated radial integrals is minimized.

The Newton's method for solving a set of simultaneous non-linear equations has been slightly modified for PF. This method should quickly converge and has the advantage over other methods in that if it does not work, the method specifies the reason for the impasse and, hopefully, corrective action may be taken. The details of the procedure are given in Appendix 3 where  $f_n$  is the difference between the  $n^{\text{th}}$  calculated and experimentally determined Slater integral, and the  $x_n^*$  are the  $n$  fitting parameters of the basis set.

A constant danger in all non-linear iterations is that the procedure will settle into a rather high local minimum and be unable to adequately search parameter space for lower minima (in non-linear problems many minima usually exist and the lowest minimum is usually not found). Unfortunately, this danger was actually reality for the Newton's method. It was all too clear from the beginning that the Newton's method was inadequate for PF. The cause of the problem was traced to the almost linear dependency of some of the Slater parameters. A detailed analysis of the problem is given in Appendix 4.

The Direct Search method should work in all cases because it is essentially an organized trial and error technique, and, indeed, it does work very well, if a bit slow. The Direct Search program has been internally developed by Westinghouse and basically works in the following manner. From the initial set of Slater parameters, the sum of the square of the differences between the known and calculated radial integrals is calculated. The base set of Slater parameters is equated to the initial set and a set of exploratory moves is made, adjusting individual Slater parameters one at a time. The sum of the squares is computed after each move. A particular move is retained if it produces a lower sum of squares, but is otherwise rejected. If a set of exploratory moves lowers the sum of squares, the adjusted Slater parameters replace the base Slater parameters and the procedure is repeated. If a set of exploratory moves does not lower the sum of squares, the base set of Slater parameters is retained and a new set of exploratory moves tried. Direct Search contains a set of rules for determining the step size of the exploratory moves

for individual Slater parameters. These step sizes depend on the success or failure of previous exploratory moves.

## 11.4 SCREENING CONSTANTS

The usage of PF requires the approximation of the Slater parameters. The PF expansion is given by Eq. (19), but is written in a more compact form as

$$P_{nl}(x) = \sum_{m=1}^M A_m P_m^{(0)}(a_m x) \quad (23)$$

where the  $P_m^{(0)}$  are the Slater orbitals. This expansion is more sensitive to the  $a_m$  values than to the  $A_m$  values since the  $a_m$  parameters appear in exponentials. This expansion is also implicitly dependent on the choice of the  $M$  Slater orbitals, i.e., on the choice of the  $nl$  for each orbital as given in Eq. (20) (Although the Slater orbitals are independent of  $n$ , the  $nl$  notation is retained to indicate which atomic orbital the Slater orbital is approximating). Since each Slater orbital is nodeless, the selection of the  $M$  orbitals will be made such that the sum of orbitals reproduces the nodes of the  $P_{nl}(x)$  as closely as possible.

The selection of the  $M$  orbitals is mainly based on experience and is explored in the next section. The approximation of the  $A_m$  is not critical and crude methods (such as guesses) suffice. However, the approximation of the  $a_m$  is an important function and is based on the concept of screening constants. From Eqs. (16), (18), and (21) we see that

$$a_m = K [(Z - \sigma_{nl})/n]^{1/2} \quad (24)$$

gives a method for approximating these parameters.

Slater<sup>40</sup> has given some rules for the estimation of screening constants which are convenient to use, but very inaccurate. A more accurate set of rules is given by Burns<sup>41</sup> who fit a single Slater orbital

to more than 90 Hartree-Fock wavefunctions. The results are given in Table X. If  $n'$  is less than  $n-2$ ,  $\sigma_{n',\ell}$  is 1 and if  $n'$  is larger than  $n+2$ ,  $\sigma_{n',\ell}$  is 0. The screening constant in Eq. (24) is obtained by summing the screening constants for each  $n'\ell'$  electron (excluding the  $n\ell$  th electron) in the atom. Thus,

$$\sigma_{n\ell} = \sum_{n',\ell'} \sigma_{n',\ell'} \quad (25)$$

For example, the screening constant for the Cu 4s electron is given by

$$\sigma_{4s} = 10 + 2(0.90) + 6(0.75) + 10(0.50) = 21.3 \quad (26)$$

In other words, the 4s electron sees an effective nuclear charge of 7.7 since  $Z$  for copper is 29.

An alternate method of obtaining screening constants is to use Eq. (18) by putting Mann's values<sup>38</sup> of the binding energy on the left hand side and solving for the screening constant. This can be done for the first 103 atoms and the resulting screening constants averaged. The result is given in Table XI. In this case the screening constant for the Cu 4s electron is given by

$$\sigma_{4s} = 10 + 2(0.875) + 6(0.776) + 10(0.918) = 25.586 \quad (27)$$

or an effective nuclear charge of 3.414. This value is considerably lower than the value calculated from Burns' rules. This is consistent with the different rule derivations since Burns fit the entire wavefunction whereas the Mann's rules are obtained from Eq. (16) which is only valid for the outer portion of the wavefunction.

## 11.5 APPLICATION TO THE Cu 4s ELECTRON

The final proof of any new numerical technique is in the application of the technique to a good test case. A good test case for PF is the Cu 4s electronic radial wave function. This wave function is sufficiently compressed that 15-point Laguerre integration can be used, thereby reducing computer expenses. On the other hand it is sufficiently complicated, e.g., it has three nodes, to tax any radial wave function generating technique. It may at first appear that a s wave function is too simple and that a p or d wave function should be selected. However, these latter wave functions are too extended for 15-point Laguerre integration or have too few nodes. Furthermore, although there is a considerable difference between different  $\ell$  value angular wave functions, there is no explicit difference between different  $\ell$  value radial wave functions.

Values of some  $\langle r^n \rangle$  integrals and Slater integrals between the 4s electron and some inner shell electrons are given in Table XII. The  $F^0$  Slater integral, the normalization integral, and the three orthogonality integrals with the 3s, 2s, and 1s electrons gives values of five integrals which the PF 4s wave function must reproduce. Thus, the PF expansion will have five fitting parameters. The 3s, 2s, and 1s wave functions needed for the orthogonality integrals will be those of Mann,<sup>48</sup> as will be the 4s wave function which will be considered as the "true" wave function with which the PF wave function will be compared.

There are many different ways of selecting the initial PF expansion. Seven different methods were tried; the first four expansions have three Slater orbitals with the last exponent being fixed, and the last three expansions have five Slater orbitals with all the exponents being fixed. Thus, the first four expansions can have at most two nodes while trying to reproduce a three node wave function. This may lead



to some inaccuracy near the origin. However, these same expansions have two fitting parameters in the exponents which would appear to give them a greater flexibility than the five-term expansions. These seven expansions were tested by comparing, after 100 seconds of computing time on a Burroughs B5500 Computer, the standard deviation between the five PF integrals and the five Hartree-Fock integrals. The results are summarized in Tables XIII and XIV. These expansions will now be described in detail.

Set 1: Switched Input. This set was actually set 3, but an accidental shuffling of data cards exchanged the  $a_2$  and  $A_3$  parameters. The result was that the first and second Slater orbitals almost cancelled. In other words, this set represents an extremely bad initial expansion and should consequently yield relatively bad results. However, as Table XIII shows, the PF procedure was able to recover from this extremely bad set (note the initial standard deviation of 8.983!) and produce a respectable final standard deviation of 0.069! Although this final standard deviation was the highest found, it is not bad and proves the great stability of PF.

Set 2: Optimized Set. Since the 4s wave function has one very prominent hump, a good starting expansion might be obtained by first optimizing the fit between a three-term expansion and the single hump. The result of this optimization is given in Table XIII. Although there are no nodes in this set, the PF procedure inserted one.

Set 3: Burns Set. This set has its exponents determined from the Burns<sup>41</sup> screening constants. The  $A_m$  parameters are arbitrarily fixed.

Set 4: Mann's Set. This set has its exponents determined from Mann's binding energies.<sup>38</sup> The  $A_m$  parameters are arbitrarily fixed.

Three of these three-term expansions resulted in two node PF wave functions. This seems to indicate that the PF wave function is using one Slater orbital to reproduce the main hump of the 4s wave function (and thereby the  $F^0$  and normalization integrals) and two Slater orbitals to accommodate the orthogonality constraints.

Set 5: Mann's Set. This five-term expansion is determined from Mann's binding energies as was the case for Set 4. It is interesting that although the initial standard deviation is worse than that of Set 4, the final standard deviations are almost identical. The five Slater orbitals for this and later sets are chosen so that there is a 1s, 2s, and 3s Slater orbital for the orthogonality conditions, a 4s orbital for the normalization, and a 3d orbital to help form the main hump of the wave function.

Set 6:  $a_m$  Peaked. The location of the maximum value of a Slater orbital is given by

$$x_{\max} = p_m / a_m \quad (28)$$

where  $p_m$  is the power of  $x$  (or  $r$ ) in the Slater orbital (see Eq. (20)). The  $x_{\max}$  of the Hartree-Fock orbitals which these Slater orbitals are approximating are given in Table XV. The  $a_m$  are determined by setting  $p_m$  to the conventional value of  $\ell + 1$ . The  $A_m$  in all the five-term expansions are arbitrarily set to the  $x_{\max}$  value of the  $n^{\text{th}}$  orbital divided by the square root of the sum of the squares of all the  $x_{\max}$  values. The signs are selected to give three nodes. This procedure yields the same accuracy as the last two sets.

Set 7:  $p_m$  Peaked. Instead of letting  $p_m$  be  $\ell + 1$ , the  $a_m$  could be set to those values of Set 5 and  $p_m$  could be found from Eq. (28). The result is given in Table XV. These "exact"  $p_m$  can then be rounded to the nearest integer value, and the  $a_m$  solved for. Thus s Slater orbitals approximate the 1s and 3d Hartree-Fock orbitals whereas p Slater orbitals approximate the 2s, 3s, and 4s Hartree-Fock orbitals. This set gives a standard deviation at least three times lower than the previous sets. This illustrates the importance of having each Slater orbital accurately represent the main hump of the orbital it is approximating.

Set 8: Final Set. This set is simply a continuation of Set 7 and illustrates the capability of PF to obtain accurate wave functions. In several minutes of computing time the standard deviation is reduced from 0.0100 to 0.0002. In detail the errors in the five integrals are given by

$$\begin{aligned}
 \langle 4s | 1s \rangle &= -8 \times 10^{-7} \\
 \langle 4s | 2s \rangle &= -3 \times 10^{-7} \\
 \langle 4s | 3s \rangle &= 2 \times 10^{-5} \\
 \langle 4s | 4s \rangle &= 3 \times 10^{-4} \\
 F^{\circ} &= -3 \times 10^{-4}
 \end{aligned}
 \tag{29}$$

The orthogonality constraints are the best satisfied.

The final result of Set 5 has two nodes whereas the results of the last three sets have three nodes. The most accurate sets possessed three nodes although this is clearly no guarantee of a good set.

Thus far the various expansion sets have been compared as to how well they reproduce the five radial integrals of (29). However, the real question is how well they reproduce the 4s Hartree-Fock wave function. The answer is given in Table XVI where, in particular, the percent standard deviation between the PF and Hartree-Fock wave functions is given in the third column. It is quite evident that a good fit of the integrals in (29) does not guarantee a good fit of the wave function. Actually, of the first six sets, the Burns Set and Optimized Set give the best results. Of course, Set 7 (and therefore Set 8) yields the best wave function. The  $\langle r^n \rangle$  integrals describe where the PF expansion gives a poor fit. The fits are usually poorest at very small  $x$ , very good in the main portion of the wave function, and gradually become poorer in the tail. The wave function derived by PF Set 8 is compared to the Hartree-Fock wave function in Fig. (41). This figure gives ample proof that the PF method works and works well.

## 12. GROUP PROPERTIES

Group theory has successfully elucidated and simplified the angular portion of atomic wave functions. It is hardly an exaggeration to state that much, if not most, of our knowledge of the actinide and rare earth atoms has come from their group properties. However, the present status of the radial portion of atomic wave functions is quite primitive with respect to the angular portion of the wave function. The best radial wave functions presently obtainable result from some type of Hartree-Fock calculation. This type of calculation is very difficult and time consuming, even with the use of modern computers. In addition, there are many unsolved theoretical problems in the Hartree-Fock procedure.

The greatest weakness of Hartree-Fock procedures is that the resulting wave function has no known transformation properties with respect to any symmetry groups of the atom. Because the angular wave functions do transform in known ways with respect to certain groups, many selection rules are known, and even more important, many matrix elements are known which are proportional to each other. This latter result, a consequence of the Wigner-Eckart theorem, enables one to calculate the values of one set of matrix elements and, after finding a single constant of proportionality, to write down directly the values for another set having the same transformation properties. Unfortunately, since the transformation properties of the radial wave functions are unknown, such a labor-saving simplification cannot be used to relate radial matrix elements.

The mathematical techniques to be used in this work are not well defined. Although a great deal of effort has gone into the general problem<sup>57</sup>, it is not certain that the techniques exploited by mathematicians are the best techniques to apply to physical problems. Because of the uncertainty in the techniques and the associated inherent difficulties, the present investigation is confined to the hydrogen atom, since the radial wave functions are well known and well studied in this case.

Although the hydrogen atom has been extensively studied, most of the group theoretical work which involves radial wave functions has consisted of studies of hydrogen using the orthogonal groups  $O(4)$ ,  $O(4,1)$ , etc. However in this case, the radial wave function has not been studied directly since the basic functions for these groups are composed of product of radial and angular parts. This report studies the group properties of the hydrogen radial wave function themselves.

Two approaches for this study immediately come to mind. The first approach is to search for a selection rule based on a symmetry group of the hydrogen atom:  $R(4)$ , the proper rotation group in four dimensions. The second approach is to study the groups for which Laguerre polynomials form bases of representation. These groups may be pertinent because the hydrogen radial wave function is proportional to a Laguerre polynomial.

These approaches are studied in detail in Appendix 5. The  $R(4)$  group does explain some selection rules and has promise for explaining some vanishing matrix elements. The second approach leads to the complex 3-dimensional rotation group. In order to search for the desired selection rules, the representation to which the operators  $r^{-s}$  belong must be known. The latter problem is not trivial and the solution is not known.

Another approach is examined in Appendix 6. Here hydrogenic radial wave functions are shown to form bases for representations of the algebra of a three dimensional non-compact group. Powers of  $r$  are found to transform as tensors with respect to this algebra. Through the properties of the group, matrix elements of  $r^{-N}$  ( $N$  positive) can be expressed in terms of the familiar Clebsch-Gordan coefficients for  $R(3)$ . For the first time these coefficients explain the known selection rules of the radial wave functions of hydrogen.

### 13. SUMMARY

The calculation of atomic spectra requires the knowledge of radial wave functions which determine the transition probabilities between the atomic energy levels. Transition probabilities are very difficult to measure and they are therefore calculated whenever possible. For example, in arc discharge emission calculations the angular wave functions are calculated in intermediate coupling from experimentally determined Slater integrals and the radial wave functions are calculated from the Thomas-Fermi<sup>4</sup> or the Bates and Damgaard coulomb<sup>18</sup> approximation, but these latter methods are limited to light atoms with one or two valence electrons. However, it should be possible to determine the radial wave function for any atom by fitting a power series expansion with parametric coefficients of the radial wave function to the experimentally determined Slater integrals (used for the angular wave function) of the radial wave functions, keeping the radial wave function normalized and orthogonal to closed shell electrons. This parameter fitting (PF) technique has the advantage of being independent of the complex electronic shell structure. Thus, PF should succeed where all other methods fail.

An alternative to the PF method is to apply group theory directly to the calculation of the transition probability matrix elements, thus bypassing the need for an exact knowledge of the radial wave function. This technique has worked extremely well for angular wave functions but thus far has failed for radial wave functions.

This study of radial wave functions has progressed with some significant progress. The PF technique has been developed and tested on a Hartree-Fock Cu 4s radial wave function which was reproduced by PF to within  $\pm 8\%$ . This technique is relatively slow but for the first time a method is available for the determination of radial wave functions for any atom. Moreover, this technique is more consistent than other methods since the same Slater integrals are used for both the angular and radial wave functions.

The knowledge of "experimentally determined" radial wave functions via PF is intriguing. Transition probabilities may be calculated more accurately and for more complex atoms than presently done in arc discharge calculations such as described in the first six chapters of this report. Furthermore, these transition probabilities would be "experimentally determined", i.e., not from ab initio theoretical calculations.

A potentially more interesting application of PF is to determine the radial wave functions of atoms in crystals. Whenever the crystal field parameters are known, they can be treated as additional Slater integrals in PF. Thus, the radial wave function of an atom can be studied in different crystals, e.g.,  $\text{Nd}^{3+}$  in YAG,  $\text{LaCl}_3$ ,  $\text{Y}_2\text{O}_3$ ,  $\text{Y}_2\text{O}_2\text{S}$ , etc. The correlation between the physical extent of the radial wave function and the fluorescing or lasing properties of the atom can then be studied.

Significant progress has also been achieved in the application of group theory to the calculation of matrix elements over the radial wave functions of hydrogen. In particular, hydrogenic radial wave functions have been shown to form bases for representations of the algebra of a three dimensional non-compact group. Through the properties of this group, matrix elements of  $r^{-N}$  ( $N$  positive) were expressed in terms of the familiar Clebsch-Gordan coefficients for the proper rotation group in three dimensions,  $R(3)$ . For the first time these coefficients explain the known selection rules of the radial wave functions of hydrogen.

This successful group theoretical investigation of the hydrogen radial wave function is of particular long-range significance and should be immediately applicable to heavier atoms via at least two methods: the quantum defect method and the  $1/Z$  expansion method. Both methods use hydrogenic radial wave functions. The PF method could also be used by replacing the Slater orbitals in the PF expansion with hydrogenic wave functions.

This successful investigation strongly suggests that group theoretical investigations of more complicated radial wave functions may be possible. In addition, it is particularly gratifying to demonstrate that the radial and angular parts of the atomic wave function can be placed on a more even footing and theoretically treated with the same general techniques.



## APPENDIX 1

Reprinted from **APPLIED OPTICS**, Vol. 8, page 1875, September 1969  
Copyright 1969 by the Optical Society of America and reprinted by permission of the copyright owner

# A Comparison of Lamps for Use in High Continuous Power Nd:YAG Lasers

I. Liberman and R. L. Grassel

The efficiency of krypton, xenon, and tungsten-iodine lamps for pumping Nd:YAG are compared both spectroscopically and by laser pumping. The relative pumping efficiencies of xenon and tungsten to krypton are 0.86 and 1.1, respectively. However, because the tungsten filament uses a higher percentage of its power in overcoming the laser threshold, the krypton lamp with its larger power density yielded the best over-all efficiency. An output power of 105 W was obtained at an input power of 3610 W for an over-all efficiency of 2.9%.

## Introduction

The tungsten filament lamp was the first and is today the most common lamp used for pumping Nd:YAG in the cw mode of operation. Because of the development of the tungsten-iodine cycle these lamps are compact and can operate for appreciable duration near the melting point of tungsten. Even at this temperature, the radiance of tungsten is low compared to some gas discharges. However, if the radiance from continuous discharges is to compete with the radiance from a tungsten filament, lamps must be constructed having electrodes and envelopes which can withstand the average power dissipated at high current densities.

The diameter of Nd:YAG rods used for cw applications is limited to the order of 1 cm because of the radial thermal gradients occurring at high average power and because of growth considerations. In any imaging pump cavity there is no advantage to lamp diameters being larger than rod diameters since the imaged radiance can never be greater than the source radiance and that it is desirable to collect the radiation over  $4\pi$  sr. At current densities obtainable continuously in a 1-cm diam discharge, the plasma is optically thin. That is, the radiation from the continuum is much less than that of a blackbody at the same temperature as the plasma. The radiance from the line spectrum may be orders of magnitude greater than that from the continuum. Therefore if the line spectrum of a gas has a good overlap with the absorption spectrum of Nd:YAG it might be superior gas for use as a laser pump. However, although intense, the lines are usually narrow and therefore may only contain a negligible part of the energy dissipated by the lamp.

It has been observed<sup>1-3</sup> that the line spectrum from krypton is a better match to Nd:YAG than the line spectrum of xenon. For pulsed pumping of lasers, xenon is superior to krypton because the current densities are sufficiently high that the line spectrum is negligible<sup>4</sup> and xenon, because of its large atomic weight, is a more efficient continuum radiator than krypton.<sup>5</sup> For continuous discharge lamps the comparison becomes difficult because both the continuum and the line radiation may be nearly equivalent. A number of methods can be used to compare lamps although none of them are entirely satisfactory.

The simplest method is to measure the fluorescence from a Nd:YAG sample when irradiated by various sources placed at large distances from the YAG sample. This experiment is difficult to perform because the intensity is low, the total radiation is orders of magnitude greater than the fluorescence, and the radiation around  $1.06 \mu$  is comparable to the fluorescence. Read<sup>1</sup> performed an experiment of this type and concluded that the relative fluorescence resulting from Kr, Xe, and W-I<sub>2</sub> lamps was 1.90:1.00:0.63, respectively.

A second approach is based on spectral measurements. While this technique yields a great deal more information, the interpretation is difficult, tedious, and requires very precise wavelength measurements. The importance of wavelength precision is a result of the narrow absorption lines of Nd<sup>3+</sup> in YAG (about 10 Å) and, as will be shown, the even narrower line radiation from Xe and Kr. Previous spectral measurements<sup>2,4</sup> of continuous noble gas discharges have been made using relatively poor resolution. In one comparison between Xe and Kr<sup>2</sup> the resolution stated was 50.0 Å. However, the band replotted curves show full widths at half height of over 100 Å which is over an order of magnitude greater than the actual line width and thus distorts the actual contribution from the lines. There-

The authors are with the Westinghouse Research Laboratories, Pittsburgh, Pennsylvania 15235.

Received 12 February 1969.

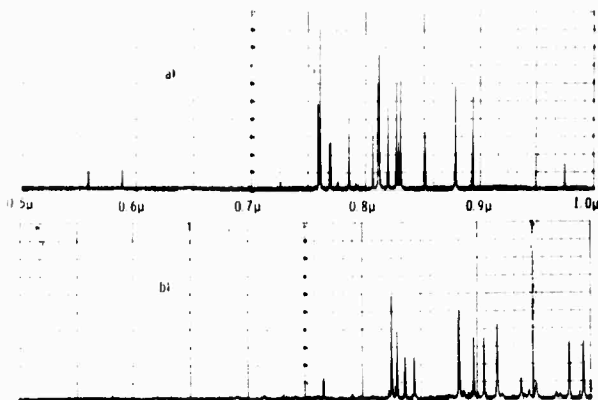


Fig. 1. Line spectrum of (a) krypton and (b) xenon lamp at 200  $\mu\text{V}$  full scale. Spectral radiance =  $15.5 \mu\text{W}(\text{sr} - \text{\AA} - \text{mm}^2 - \mu\text{V})^{-1}$ .

fore before spectral measurements can be used to compare gases, high resolution must be obtained.

A third method of comparison is the actual laser test. Here comparison is difficult unless the laser head is optimized for each specific lamp. Since a tungsten filament lamp has well defined radiating dimensions while a gas discharge does not, this comparison can be subject to criticism. Read found that Kr had a slope efficiency about 2.4 times as great as Xe or W-I<sub>2</sub>. However, since no absolute numbers are given, the degree of optimization cannot be determined.

### Experimental Apparatus

The discharge lamps used for our tests are very similar to the lamp described by Stearn and Colliver.<sup>6</sup> That is, cooling water not only flowed over the quartz envelope, but also circulated inside the hollow electrodes. The electrode spacing was 5 cm and the bore diameter 5.5 mm. The electrode diameter was 5 mm so that the gas space behind the electrode tips was kept at a minimum thus building up the operating pressure as much as possible over the fill pressure of 2 atm.

The rod used was 5 mm  $\times$  50 mm and had antireflection coatings placed on the flat ends. The rod was centered in an optical cavity of 41-cm length terminated by two dielectric mirrors of 1-m radius of curvature. The output reflectivity was 95% which for Kr and Xe pumping was found to be more nearly optimal than 98% or 92% reflectivity. The pump cavity consisted of a 25-cm diam gold coated sphere.<sup>7</sup> While we believe this cavity is superior to an elliptical cylinder, it has a further advantage when comparing lamps in that it provides a one to one image. Therefore good geometric coupling is always assured if the lamp diameter is equal to or smaller than the rod diameter. In an elliptical cylinder having an appreciable eccentricity, the image coming from over  $\frac{1}{2}$  the solid angle of the lamp radiation is magnified.

Spectral measurements were performed using a Jarrell-Ash  $\frac{1}{2}$ -m Ebert monochromator. The curved slits

were 40  $\mu$  wide corresponding to a resolution of 0.64  $\text{\AA}$ . The detector used was a silicon *p,i,n* photodiode. The system was calibrated with a calibrated tungsten spectral radiance standard and automatically corrected for non-linearity between 5000–10,000  $\text{\AA}$  by using a variable attenuator.

The laser power was measured with a Spectra-Physics model 401 photovoltaic cell in conjunction with two quartz plate beam splitters. It was calibrated using a TRG model 107 ballistic thermopile. Each quartz plate deflects the radiation 7.5° from the normal, and in mutually perpendicular planes. This allows for relatively easy alignment and removes any calibration variations with polarization. The discharge lamps were dc excited, while the tungsten lamp ran on 60-Hz ac.

### Spectral Measurements

The spectra of the krypton and xenon lamps operating at 35 A are shown in Figs. 1 and 2. Since the peak intensity of the continuum is orders of magnitude lower than that of the lines, the continuum radiation is clearly optically thin. Line widths were obtained by

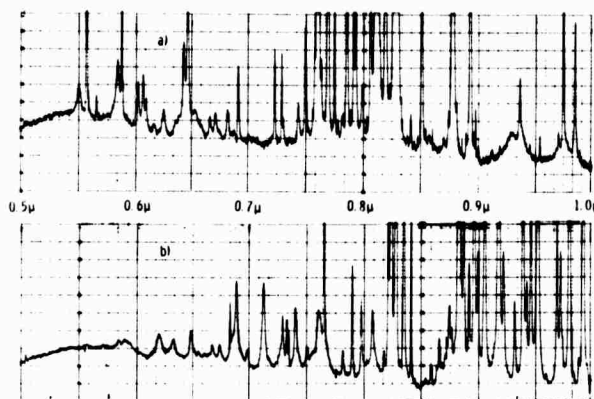


Fig. 2. Continuum spectrum of (a) krypton lamp at 2  $\mu\text{V}$  full scale and (b) xenon lamp at 5  $\mu\text{V}$  full scale. Spectral radiance =  $15.5 \mu\text{W}(\text{sr} - \text{\AA} - \text{mm}^2 - \mu\text{V})^{-1}$ .

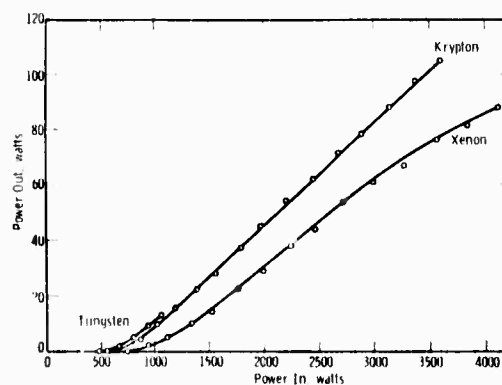


Fig. 3 Power conversion of 5 mm  $\times$  50 mm Nd:YAG.

Table I. Comparative Spectral Efficiency of Lamps for Pumping Nd:YAG

Wavelength region ( $\mu$ )	Useful portion ( $\text{\AA}$ )	Weighting factor	2.28-kW krypton		2.73-kW xenon		2.4-kW tungsten	
			Avg. intensity ( $\mu\text{V}$ )	product ( $\text{\AA}\text{-}\mu\text{V}$ )	Avg. intensity ( $\mu\text{V}$ )	product ( $\text{\AA}\text{-}\mu\text{V}$ )	Avg. intensity ( $\mu\text{V}$ )	product ( $\text{\AA}\text{-}\mu\text{V}$ )
0.50-0.60	300	0.50	0.8	120	1.4	210	1.0	150
0.74-0.83	600	0.75	0.6	270	1.0	450	1.9	855
0.86-0.90	30	0.85	0.5	13	1.0	25	1.9	48
Lines	2 <sup>a</sup>	0.75	300 <sup>b</sup>	450	—	—	—	—
Total				853		685		1053
Total/kW				374		250		430
Fluorescent efficiency				4.3%		2.9%		5.0%

<sup>a</sup> Average line width of krypton.

<sup>b</sup> Total absorption of all lines.

using a much slower scan speed. For each gas the line width of the various lines varied about 20%. An average measured full width at half height for krypton was 2.0  $\text{\AA}$  and for xenon it was 4.9  $\text{\AA}$ . Therefore, despite the lower peak intensities and fewer number of lines, the xenon lamp is a superior emitter of line radiation in the wavelength region studied. In the continuum the xenon lamp is also more efficient than krypton by about 30%.

Because of the spectral overlap of the krypton lines with the Nd:YAG absorption spectrum the krypton lamp can be more efficient than a xenon lamp for pumping Nd:YAG. The overlap was measured by placing a spectroscopic Nd:YAG sample in front of the monochromator entrance slit. The results show that the overlap for krypton lines is appreciable while for xenon the overlap is negligible. As shown in Table I an estimate of the relative pumping efficiency of the lamp is given based on the spectral measurements. The effect of reflection from the Nd:YAG spectroscopic sample was taken into account in making the calculation. It was assumed that all photons absorbed in the measured wavelength region contribute equally to photons emitted at 1.064  $\mu$ . However, the energy absorbed at each wavelength was multiplied by the ratio of the wavelength to 1.064  $\mu$ . Since the spectral measurements are absolute numbers, a calculation of laser efficiency can be approximated. This was done as given in the last row of Table I. The collected energy was assumed to be 0.75 ( $3\pi$  sr) of the emitted radiance based on a computation of the spherical pump cavity efficiency. Due to the difficulty in determining the spectral overlap the accuracy of the over-all efficiency is no better than 30%. The tungsten measurements were obtained using a 2550 K spectral radiance standard and converted to 3200 K by using a table of blackbody radiance. The 2.4-kW input power was calculated as the radiation from a 5 mm  $\times$  50 mm cylinder of 0.4 emissivity at 3200 K having an 80% radiative efficiency. These calculations show that tungsten is about 16% superior than krypton in spectral efficiency for pumping Nd:YAG.

## Laser Tests

One lamp was used for both the xenon and the krypton tests so that all other parameters would be unchanged. The lamp was first filled with two-atm xenon and pinched off. After the test, only a negligible amount of blackening was observed on the quartz wall. The lamp was opened, refilled with 2-atm krypton and pinched closed. For the case of tungsten pumping, no lamp was available for a proper geometric match to the laser rod. A 2 mm  $\times$  50 mm single coil filament was used which limited the input power to 1070 W. The results are shown in Fig. 3. The saturation of the output under xenon pumping is not peculiar to the xenon lamp. Saturation was observed with the krypton lamp when the resonator spacing was increased to 50 cm. It is believed that the saturation is a result of a strong lens effect in the rod due to the radial thermal gradient present. In pumping the rod without the resonators, and placing a He:Ne beam axially through the rod, a positive lens was observed with a waist minimum occurring less than 20 cm from the rod. This strong lensing should increase the losses for many of the oscillating modes. It is further hypothesized that since the xenon lamp is more efficient than the krypton lamp in pumping the visible absorption bands, more heat is dissipated in the rod for the same output power. Therefore, the equivalent lensing should occur at lower output power levels for the xenon lamp. With tungsten pumping, because of the low input power, a 98% output mirror produced an over-all efficiency of 1.4% compared with 1.23% using

Table II. Summary of Pumping Efficiency of Lamps Calculated by Several Ways

Efficiency	Absolute %			Relative		
	Kr	Xe	W	Kr	Xe	W
Spectral	4.3	2.9	5.0	1.0	0.68	1.16
Slope	3.74	3.22	—	1.0	0.76	—
At 80 W	2.63	2.13	—	1.0	0.81	—
At 15 W	1.16	0.89	1.22	1.0	0.77	1.06

the 95% mirror. However, for comparison purposes the 95% mirror results are shown.

Because of the threshold power required to obtain oscillations, the over-all efficiency of the system is a function of input power thus making comparisons subject to interpretation. Assuming the spectral efficiency of the lamp does not vary with power, the slope efficiency should be proportional to the spectral efficiency and equal to it for a lossless system. Row 2 of Table II gives these results. Row 3 and 4 of Table II gives the over-all efficiencies at outputs of 80 W and 15 W.

### Discussion and Conclusions

The comparison of efficiency by spectral and laser tests agree within experimental error. We believe that because of the difficulty in interpreting the spectral data, the slope efficiency is the most accurate measurement. Therefore our best estimate of relative efficiency between Kr, Xe, and W is 1:0.86:1.1, respectively. This is in considerable disagreement with Read.<sup>1</sup> Our spectral data look quite different from those previously published<sup>2,4</sup> because their spectral resolution is much poorer than the true line width of xenon and krypton operating under the conditions described.

Using the krypton lamp an output power of 105 W at an efficiency of 2.92% has been obtained. A potassium-mercury spectral additive lamp has been developed<sup>6</sup> which has a spectral efficiency over three times that of tungsten which in turn has a better

spectral efficiency than krypton. Therefore we predict that with development a cw Nd:YAG laser will have an efficiency appreciably greater than the results reported here.

We wish to thank C. Spontak, E. Kowal, and A. Zoltola for constructing the electrodes used in the discharge lamps. We also thank C. H. Church for developing the foundation of this work.

*Note added in proof:* Additional data on rare gas pumping efficiencies has been recently published by J. R. Oliver and F. S. Barnes, IEEE J. Quantum Electron. **QE5**, 225, 222 (1969). As in Ref. 1, laser test results are in arbitrary units which could lead to erroneous conclusions if all parameters are not fully optimized. Also, as in Ref. 2, the spectral resolution was 100 Å which is estimated to be an order of magnitude greater than the actual line width under their operating conditions. However, their conclusions are similar to ours.

### References

1. T. B. Read, Appl. Phys. Lett. **9**, 342 (1966).
2. P. B. Newell and J. D. O'Brien, IEEE J. Quantum Electron. **QE4**, 291 (1968).
3. N. L. Yeamans and J. E. Creedon, Tech. Rep. ECOM-3043, U. S. Army Electronics Command, Ft. Monmouth, N. J. (November 1968).
4. J. H. Goncz and P. B. Newell, J. Opt. Soc. Amer. **56**, 87 (1966).
5. I. S. Marshak, Appl. Opt. **2**, 793 (1963).
6. J. W. Stearn and D. J. Colliver, J. Sci. Instr. **43**, 52 (1966).
7. C. H. Church and I. Liberman, Appl. Opt. **6**, 1966 (1967).
8. I. Liberman, D. A. Larson, and C. H. Church, IEEE J. Quantum Electron. **QE-5**, 238 (1969).

## APPENDIX 2

### ROD TO SLAB TRANSFORMATION

Although the simple slab laser geometry has been used for the computer calculations reported in the text, the most common laser geometry is that of a cylindrical rod in a cavity. In order to fully utilize the computed results for the slab laser geometry, the cylindrical rod in a cavity geometry must be transformed to an equivalent slab laser geometry. This transformation is given in this appendix.

The emittance (power per unit surface area) absorbed by an arbitrary body as a function of wavelength is given by

$$(2.1) \quad P_a = P_o \int [1 - \exp(-\alpha c)] d\omega$$

where  $\alpha$  is the spectral absorptivity,  $c$  is the chord length traversed by the light in the body,  $P_o$  is the incident light emittance, and  $\omega$  is the solid angle. The integration is over the entire absorbing body. An effective chord length  $\bar{c}$  can be defined as that length which absorbs from a single light ray the same power density as the actual body, i.e.,

$$(2.2) \quad P_a = P_o [1 - \exp(-\alpha \bar{c})]$$

Thus an effective chord length can be found for a given wavelength for any absorbing body from an evaluation of Eq. (2.1).

The effective chord length for the slab geometry is easily found when the light is perpendicularly incident on the slab because then

$$(2.3) \quad P_a = P_o [1 - \exp(-\alpha_s t)]$$

where  $t$  is the slab thickness and  $\alpha_s$  is the absorptivity of the slab. Therefore

$$(2.4) \quad \bar{c}_s = t$$

which is rather obvious.

The effective chord length for a laser rod geometry can be found from Eq. (2.1) with one modification. The rod in a spherical laser cavity subtends a very small solid angle when viewed from the lamp and therefore almost all the light absorbed by the laser rod is first reflected by the laser cavity walls. The rod is thus bathed in this reflected lamp light. However, the light intensity emitted by the lamp has an approximate Lambertian distribution with respect to the angle  $\theta$  between the emitted light ray and the normal to the outer lamp wall. Specular reflecting laser cavities maintain this Lambertian distribution at the rod surface. A surface roughened rod will slightly modify the Lambertian distribution but probably not by a factor larger than the accuracy of the general pump efficiency calculations. In any event, we assume the light distribution within the rod to be Lambertian and that Eq. (2.1) can be written as

$$(2.5) \quad P_a = (P_o/\pi) \int [1 - \exp(-\alpha_r c)] \cos \theta d\omega$$

where the integration is over the laser rod and  $\alpha_r$  is the rod absorptivity. The  $\pi$  in the denominator keeps the same light emittance incident on the laser rod and slab. The integral in Eq. (2.5) has not been analytically solved but Pukhov<sup>51</sup> has numerically evaluated it for an infinite cylinder of diameter  $d$  and expressed his results in the simple form:

$$(2.6) \quad \bar{c}_r = \left( \frac{4.7}{\alpha_r d + 6.44} + 0.27 \right) d$$

The rod to slab transformation is completed by equating the emittance absorbed by the slab to the emittance absorbed by the rod, provided the incident emittance is the same. In other words Eq. (2.2) is the same value irrespective of which effective chord length is used, i.e.,

$$(2.7) \quad \alpha_s \bar{c}_s = \alpha_r \bar{c}_r$$

which implies that

$$(2.8) \quad t = D \bar{c}_r$$

where D is the activator doping of the rod relative to the activator doping of the slab.

The transformation is strictly valid for only one wavelength but for the 5 x 50 mm Nd:YAG rod used for the laser system efficiency measurements Eq. (2.8) is fairly constant for all wavelengths, as can be seen by using the experimental parameters to obtain

$$(2.9) \quad D = 1.3/0.7$$

and

$$(2.10) \quad 0.63 \text{ cm} < t < 0.93 \text{ cm}$$

where, using Eqs. 2.6 and 2.8, the maximum absorptivity ( $10 \text{ cm}^{-1}$ ) within the main absorption bands of the rod determines the lower limit and zero absorptivity determines the upper limit. An average value for the absorptivity is roughly  $2 \text{ cm}^{-1}$  which gives an average value of

$$(2.11) \quad t = 0.84 \text{ cm}$$

This value is better than one might expect at a casual glance. The average value of  $2 \text{ cm}^{-1}$  for the absorptivity is admittedly crude but only appears in the denominator of Eq. (2.6) and a  $\pm 1 \text{ cm}$  error in this average value only gives an error of  $\pm 0.04 \text{ cm}$  for the effective slab thickness. Thus, to a good approximation, the laser rod used in the experimental measurements reported in Appendix 1 is equivalent to a slab of thickness  $0.84 \text{ cm}$ .



### APPENDIX 3

#### NEWTON'S METHOD FOR PARAMETRIC FITTING OF RADIAL WAVE FUNCTIONS IN INTEGRALS

A. J. Federowicz

The radial wave fitting problem has already been formulated as one of solving sets of simultaneous non-linear equations in which the number of fitting parameters (variables in the fitting problem) equal the numbers of equations. These simultaneous equations result from applying normality and orthogonality conditions which the radial wave function must satisfy and from attempting to obtain agreement with certain experimental observations.

If the number of equations were larger than the number of parameters, this proposed procedure would be modified, but not drastically. What would then be done would be to fit such overdetermined sets of equations using least squares. As will be seen, a least squares criterion is suggested here for a different reason and to apply this criterion to overdetermined sets of equations would be a minor modification.

The proposed procedure is to use a modified form of Newton's method for solving systems of simultaneous non-linear equations. The modifications are aimed at guaranteeing convergence of the iteration and at avoiding the use of analytic partial derivatives.

Newton's method for solving a set of simultaneous non-linear equations is as follows: as the problem is generally phrased, for a set of  $m$  functions of  $m$  variables, one is to find a point at which the  $m$  functions are simultaneously zero, that is, find  $\vec{x}^* = (x_1^*, x_2^* \dots x_m^*)$  such that

$$(3.1) \quad f_1(\vec{x}^*) = f_2(\vec{x}^*) = \dots = f_m(\vec{x}^*) = 0$$

or in compact form

$$(3.2) \quad \vec{f}(\vec{x}^*) = 0.$$

Newton's method consists of making simultaneous linear approximations to the  $m$  functions at some point,  $\vec{x}^{(n)}$ , and solving this set of linear approximations for the point where all will be zero. That is

$$\begin{aligned}
 (3.3) \quad f_1(\vec{x}) &\approx f_1(\vec{x}^{(n)}) + f_{1x_1} \Delta x_1 + f_{1x_2} \Delta x_2 + \dots + f_{1x_m} \Delta x_m \\
 f_2(\vec{x}) &\approx f_2(\vec{x}^{(n)}) + f_{2x_1} \Delta x_1 + f_{2x_2} \Delta x_2 + \dots + f_{2x_m} \Delta x_m \\
 &\vdots \\
 f_m(\vec{x}) &\approx f_m(\vec{x}^{(n)}) + f_{mx_1} \Delta x_1 + f_{mx_2} \Delta x_2 + \dots + f_{mx_m} \Delta x_m
 \end{aligned}$$

which upon being set equal to zero yields

$$(3.4) \quad \begin{bmatrix} \Delta x_1 \\ \Delta x_2 \\ \vdots \\ \Delta x_m \end{bmatrix} = - \begin{bmatrix} f_{1x_1} & f_{1x_2} & \dots & f_{1x_m} \\ f_{2x_1} & f_{2x_2} & \dots & f_{2x_m} \\ \vdots & \vdots & \ddots & \vdots \\ f_{mx_1} & f_{mx_2} & \dots & f_{mx_m} \end{bmatrix}^{-1} \begin{bmatrix} f_1 \\ f_2 \\ \vdots \\ f_m \end{bmatrix}$$

or in compact form

$$(3.5) \quad \vec{\Delta x}^{(n)} = - \left[ \frac{\partial \vec{f}}{\partial \vec{x}}(\vec{x}^{(n)}) \right]^{-1} \vec{f}(\vec{x}^{(n)})$$

The iteration then consists of using the obvious recurrence relation

$$(3.6) \quad \vec{x}^{(n+1)} = \vec{x}^{(n)} + \vec{\Delta x}^{(n)}$$

If there is only one equation in one unknown, this formulation reduces to the familiar form of Newton's method in which

$$(3.7) \quad \Delta x^{(n)} = - \frac{f(x^{(n)})}{f'(x^{(n)})}$$

$$x^{(n+1)} = x^{(n)} + \Delta x^{(n)}$$

In the radial wave function fitting problem some of the equations will not be in analytic form but only as numerical approximations to integrals. Difference approximations to the partial derivatives should thus be used in constructing the  $[\vec{f}_x]$  matrix. This modification will considerably simplify the necessary computer programming since only one subroutine, which simply evaluates  $\vec{f}$ , will be necessary in setting up  $\vec{f}$  and  $[\vec{f}_x]$  for each case. It is necessary to use differences which will estimate  $\vec{f}_x$  accurately, however. Attention must thus be paid to the question of how many significant digits result from the differencing process.

In order to guarantee convergence of the iteration,  $\vec{x}^{(n+1)}$  computed using (1.6), will be accepted only if it represents a better solution to the set of simultaneous equations than  $\vec{x}^{(n)}$  does. For reasons of simplicity "better" will be taken to mean that

$$(3.8) \quad ||\vec{f}(\vec{x}^{(n+1)})||^2 < ||\vec{f}(\vec{x}^{(n)})||^2$$

with weighting of the components of  $\vec{f}$  being an option. Equation (1.8) says that the sum of the squared errors must be reduced from one step to the next.

If  $\vec{x}^{(n+1)}$  results in an increase in  $||\vec{f}(\vec{x})||^2$  then the chord joining  $\vec{x}^{(n)}$  and  $\vec{x}^{(n+1)}$  will be searched for a better value. This can be done assuming linearity of  $\vec{f}$  between  $\vec{x}^{(n)}$  and  $\vec{x}^{(n+1)}$  as follows:

$$(3.9) \quad \vec{f}(\vec{x}^{(n)} + s\vec{\Delta x}^{(n)}) \doteq \vec{f}(\vec{x}^{(n)}) + s(\vec{f}(\vec{x}^{(n+1)}) - \vec{f}(\vec{x}^{(n)}))$$

$$= \vec{f}^{(n)} + s \vec{\Delta f}^{(n)}$$

The point at which the norm of this linear approximation is minimized can be used to determine  $s$ . The minimizing  $s$  is given by

$$(3.10) \quad s^* = - \frac{\vec{f}^{(n)} \cdot \vec{\Delta f}^{(n)}}{\|\vec{\Delta f}^{(n)}\|^2}.$$

If this interpolating procedure does not produce a smaller  $\|\vec{f}\|^2$  at  $\vec{x}^{(n)} + s^* \vec{\Delta x}^{(n)}$ , then it may be repeated several times using  $\vec{x}^{(n)}$  and  $\vec{x}^{(n)} + s^* \vec{\Delta x}^{(n)}$  as new end points. If this strategy fails then a different one dimensional search strategy, such as interval halving, may be employed.

In the case that  $\vec{f} = 0$  has no solution, as is likely to be the case in this problem, the determinant of  $[\frac{\partial \vec{f}}{\partial \vec{x}}]$  will tend to zero as  $\|\vec{f}\|$  tends to a positive value. The analogy with the one dimensional case is that  $f'(x^{(n)})$  is zero at any point where  $\|f^2\|$  is minimized, if that minimum is non-zero, which is the case when  $f = 0$  has no solution. It is instructive to examine what Newton's method does when used to look for a zero of  $f$  which does not exist in the one dimensional case. The method will usually oscillate, neither approaching a limit nor diverging, in such a case. For example, if the problem is to find a zero of  $f = 1 + x^2$  then one has

$$(3.11) \quad \Delta x^{(n)} = - \frac{1+x^{(n)2}}{2x^{(n)}}$$

and

$$(3.12) \quad x^{(n+1)} = \frac{x^{(n)}}{2} - \frac{1}{2x^{(n)}}$$

For large  $|x^{(n)}|$  the term  $1/2x^{(n)}$  can be ignored and this formula says that  $x^{(n)}$  will be halved at each step. As  $|x^{(n)}|$  becomes small, however, this term dominates and causes  $|x^{(n)}|$  to again become large,

while also causing  $x^{(n)}$  to change sign. A similar behavior occurs in multi-dimensional problems in which  $\vec{f} = 0$  has no solution. By insisting that  $||f||^2$  be reduced on each step, this possibility of oscillation is avoided.

A problem which may also occur is that  $\vec{f} = 0$  may have several solutions and/or that  $||f||^2$  may have several local minima. Since this problem can be rigorously resolved only in the case that one is dealing with a convex function, different starting points should be tried for the iteration. Then if the iteration consistently converges to the same answer in a given case, one can be reasonably certain that the answer is unique; if convergence to different answers occurs, then the best answer should be selected and one must be careful about finding the best answer in other cases.

As a final point, it should be mentioned that a number of other optimum search procedures are potentially applicable to this problem. These include Direct Search, GOOP and a non-linear least squares program written by R. D. Fardo, three methods which have been used extensively at this location. An essential feature, which must be maintained in any computer program of this proposed procedure in order to make such other techniques easily usable, is the separation of the functional evaluation subroutine from the logic of the iterative method.

#### APPENDIX 4

##### COMPARISON OF DIRECT SEARCH AND NEWTON'S METHOD

A. J. Federowicz

This appendix is a post-mortem on why Newton's method, suggested in Appendix 3, did not work well on the radial wave function parametric fitting problem. Conversely light is shed on the question why Direct Search did a relatively much better job.

The characteristic exhibited by the modified Newton's method was that it became hung up in local areas during the search. Very little improvement in the least squares criterion would occur for many iterations. At the time that this occurred, a computer program bug was suspected. A bug was not the cause, however, but rather the problem is an ill-conditioned one for Newton's method. As an example of slow convergence, the following sums of squares occurred in one case:

Iteration #	Error Sum of Squares
0	6.319567
1	3.107108
2	3.103914
3	3.102053
4	3.101231

By comparison, Direct Search produced the following sequence starting near the parameter point of iteration #1:

Iteration #	Error Sum of Squares
0	3.108122
1	2.538027
2	.603644
3	.338447
4	.217680
5	.116751
⋮	
12	.012570

There are a number of equivalent ways of explaining the observed phenomena. One explanation is that the radial wave function parameters are highly correlated in their effect upon the sum of square criterion. The result of this correlation is that Newton's method selects a very poor direction for minimizing the sum of squares locally. The selected direction would be very good if the linear approximation used by Newton's method were valid far from the current point. However, the problem is highly non-linear and the use of a linear approximation to select a point far from the current one is thus weak.

In order to illustrate what can occur, assume for the moment that there are two functions,  $f_1$  and  $f_2$ , for which zeroes are being sought and two parameters  $x_1$  and  $x_2$  which are being searched for these zeroes. Then the search procedure of Appendix 3 consists of making linear approximations to both and solving for where these linear approximations are simultaneously zero. A case in which the two parameters are correlated in their effect upon the sum of squares is illustrated in the Fig. 42. The correlation is identified by the nearly parallel gradients  $\vec{\nabla}f_1$  and  $\vec{\nabla}f_2$ . Based upon these gradients, a good local direction in which to search is the  $x_2$  direction. Based upon the contours, the step length to take would be approximately the length of the pictured  $\vec{\nabla}f_1$ . However, the modified Newton's method selects the intersection of the zeroes of the linear approximations. The resultant step length overtakes the linear approximations and only a small improvement in the sum of squares can be achieved in this direction.

A measure of the correlation between parameters in the illustrated case is the sine of the angle between the two gradient vectors. This is given by

$$\sin(\vec{\nabla}f_1, \vec{\nabla}f_2) = \frac{|\text{Det} [\vec{\nabla}f_1 \ \vec{\nabla}f_2]|}{|\vec{\nabla}f_1| \ |\vec{\nabla}f_2|}$$

As this measure increases from 0 to 1, the gradient vectors go from parallel to being orthogonal.

The similar statistic in 3 parameters measures how nearly co-planar the 3 gradient vectors would be. The identity

$$\frac{|\text{Det} [\vec{\nabla}f_1 \ \vec{\nabla}f_2 \ \vec{\nabla}f_3]|}{|\vec{\nabla}f_1| \ |\vec{\nabla}f_2| \ |\vec{\nabla}f_3|} = \sin(\vec{\nabla}f_1, \vec{\nabla}f_2) \sin(\vec{\nabla}f_1, \vec{\nabla}f_2, \vec{\nabla}f_3)$$

puts this co-planar relationship into terms similar to the 2 dimensional case. In 3 dimensions the measure equals the product of the sine between two of the gradients multiplied by the sine of the angle between the last gradient and the plane of the first two. This final product of sines relationship extends to an arbitrary number of dimensions, one sine term being added for each additional dimension.

For the 5 parameter case noted earlier in which the modified Newton's method converged very slowly, this measure was found equal to .00019, a value indicating that the 5 gradients are very nearly co-planar and thus explaining the slow convergence.

Direct Search, by contrast, works directly with the sum of squares criterion, computing it at neighboring points to the current point. Referring to Fig. 42, Direct Search would choose a direction more nearly in line with the gradients and would thus achieve a bigger local improvement in the criterion. It does not extrapolate a long distance for zero and come up with nothing as a result.



## APPENDIX 5

### GROUP THEORETICAL PROPERTIES OF RADIAL WAVE FUNCTIONS

Lloyd Armstrong, Jr.

Group theory has been applied with great success to studies of the angular portion of atomic wave functions. It is hardly an exaggeration to state that much, if not most, of the present day knowledge of the actinide and rare earth atoms could scarcely have been obtained without use of this powerful tool. The state-of-the-art concerning the radial portion of atomic wave functions is, however, quite primitive with respect to that of the angular portion of the wave function. The best radial wave functions obtainable result from some type of Hartree-Fock calculation. This type of calculation is very difficult and time consuming to carry out, even using the best of modern computers. In addition, there are many unsolved theoretical problems relating to the Hartree-Fock procedure.

Rather than discuss any of these difficulties, however, let me point out what I consider to be the greatest weakness of such a procedure: the resulting wave function has no known transformation properties with respect to any symmetry groups of the atom. Because the angular wave functions do transform in known ways with respect to certain groups, one is able to immediately write down a number of selection rules on angular matrix elements and, even more important, to pick out types of matrix elements that must differ in value by only a proportionality factor. This latter result, a consequence of the Wigner-Eckart theorem, enables one to calculate the values for one set of matrix elements and, after finding a single constant of proportionality, to write down directly the values for another set having the same transformation properties. Unfortunately, since no transformation properties of the radial wave functions are known, such a labor-saving simplification cannot be used to relate radial matrix elements.

The purpose of this report is to describe ways in which one might hope to determine the transformation properties of radial wave functions. We wish to start by studying the simplest possible system, hydrogen. Pasternack and Sternheimer<sup>52</sup> have reported a very interesting selection rule on hydrogenic radial wave functions:

$$(5.1) \quad \int \frac{R_{n\ell} R_{n\ell'}}{r^s} dr = 0 \quad s = 2, 3, \dots, |\ell - \ell'| + 1,$$

where the complete hydrogenic wave function is written

$$\psi_{n\ell m} = \frac{R_{n\ell}(r)}{r} Y_{\ell m}(\theta, \phi).$$

This selection rule, which has successfully defied all attempts to give it a simple explanation, looks suspiciously like the type of selection rule that results from a group property. Thus the primary goal of this type of research must be to explain the above result using group theory.

Two avenues of investigation immediately present themselves. The first involves searching for a selection rule based on a symmetry group of the hydrogen atom:  $R(4)$ , the proper rotation group in four dimensions. The second involves a study of the groups for which Laguerre polynomials form bases of representation. This latter is of interest because  $R_{n\ell}$  is proportional to a Laguerre polynomial,  $L_{n+\ell}^{2\ell+1}$ . The former may perhaps be the most susceptible to study, so we shall consider it first.

#### a) The Symmetry Group of the Hydrogen Atom.<sup>53</sup>

The  $R(4)$  symmetry group of the hydrogen atom has an algebra consisting of the three components of the angular momentum vector  $\mathbf{L}$  and the three components Lenz vector

$$\mathbf{M} = (1/2\mu)(\mathbf{P} \times \mathbf{L} - \mathbf{L} \times \mathbf{P}) - k \frac{\mathbf{r}}{r}$$

where  $k = ze^2$ . Only one of the commutators of the algebra is of real interest at the moment

$$[L^2, M_+] = -2M_z L_+ + 2M_+ L_z + 2M_+.$$

If we consider the operation of this commutator on the state  $\psi_{n\ell\ell}$ , we find

$$L^2(M_+ \psi_{n\ell\ell}) = (\ell+1)(\ell+2)(M_+ \psi_{n\ell\ell})$$

which implies that

$$M_+ \psi_{n\ell\ell} = A \psi_{n\ell+1, \ell+1}$$

where A is some constant. A detailed calculation reveals that

$$(5.2) \quad M_+ \psi_{n\ell\ell} = \frac{Y_{\ell+1, \ell+1}(\theta, \phi)}{\sqrt{2\ell+3}} \frac{\ell+1}{r} \left[ \frac{\partial}{\partial r} - \frac{\ell+1}{r} + \frac{k\mu}{\ell+1} \right] R_{n\ell}.$$

We shall return to this below.

One can, in fact, find a simple commutator which explains Eq. (5.1) if one uses the raising operator for hydrogenic radial wave functions<sup>54,55</sup>,  $R_+^\ell$

$$(5.3a) \quad R_+^\ell = \frac{d}{dr} - \frac{\ell+1}{r} + \frac{k\mu}{\ell+1}$$

$$(5.3b) \quad R_+^\ell R_{n\ell} = B R_{n\ell+1}.$$

We consider first the commutator

$$[H - \frac{\hbar^2 L^2}{2mr^2}, C_q^k] = 0$$

$$\text{where } H = \frac{\hbar^2}{2m} \frac{1}{r} \frac{d^2 r}{dr^2} + \frac{\hbar^2 L^2}{2mr^2} - \frac{ze^2}{r}$$

and  $C_q^k$  is a spherical tensor of rank k. Multiplying the commutator on the left by  $(\psi_{n\ell\ell}|$ , on the right by  $|\psi_{n'\ell'\ell'}\rangle$ , and obtain

$$\begin{aligned}
& (E_{n\ell} - E_{n'\ell'}) (\psi_{n\ell m} | C_q^k | \psi_{n'\ell' m'}) \\
&= \frac{\hbar^2}{2m} (\psi_{n\ell m} | \frac{C_q^k}{r^2} | \psi_{n'\ell' m'}) [\ell(\ell+1) - \ell'(\ell'+1)]
\end{aligned}$$

For  $n = n'$ ,  $E_{n\ell} = E_{n'\ell'}$ . The angular portion of the matrix element on the right above can easily be seen to be non-vanishing for at least one value of  $k, q$ , leaving the result

$$\theta = \int \frac{R_{n\ell} R_{n\ell'}}{r^2} dr (\ell(\ell+1) - \ell'(\ell'+1))$$

which implies<sup>56</sup>

$$(5.4) \quad \int \frac{R_{n\ell} R_{n\ell'}}{r^2} dr = 0 \quad \text{if } \ell \neq \ell'$$

Consider next the commutator

$$[H - \frac{\hbar^2 L^2}{2mr^2}, C_q^k \frac{1}{r} \frac{d}{dr} r] = 0.$$

Proceeding as before, and letting  $n = n'$

$$\begin{aligned}
(5.5) \quad & \ell(\ell+1) (\psi_{n\ell m} | C_q^k \frac{1}{r^3} \frac{d}{dr} r | \psi_{n\ell m'}) \\
& - (\psi_{n\ell m} | C_q^k \frac{1}{r} \frac{d}{dr} r \frac{1}{r^2} | \psi_{n\ell m'}) = 0
\end{aligned}$$

or

$$\begin{aligned}
& [\ell(\ell+1) - \ell'(\ell'+1)] (\psi_{n\ell m} | \frac{C_q^k}{r^3} \frac{d}{dr} r | \psi_{n\ell m'}) \\
& + 2\ell'(\ell'+1) (\psi_{n\ell m} | \frac{C_q^k}{r^3} | \psi_{n\ell m'}) = 0
\end{aligned}$$

Again, we can carry out the angular integration which is the same for both matrix elements and which has at least one non-vanishing value. We then have

$$[\ell(\ell+1) - \ell'(\ell'+1)] \int \frac{R_{n\ell}}{r^2} \frac{d}{dr} R_{n\ell'} dr$$

$$+ 2\ell'(\ell'+1) \int \frac{R_{n\ell} R_{n\ell'}}{r^3} dr = 0$$

Assume that  $\ell' > \ell$ , and use Eqs. (5.3a) and (5.3b) to treat the  $\frac{d}{dr} R_{n\ell'}$  term above. One obtains

$$[\ell(\ell+1) - \ell'(\ell'+1)] \int \frac{R_{n\ell}}{r^2} \left[ \frac{\ell'+1}{r} R_{n\ell'} \right.$$

$$\left. + \frac{k\mu}{\ell'+1} R_{n\ell'} + B R_{n, \ell'+1} \right] dr$$

$$= -2\ell'(\ell'+1) \int \frac{R_{n\ell} R_{n\ell'}}{r^3} dr.$$

Because of Eq. (5.4), the above simplifies greatly, leaving

$$\{[\ell(\ell+1) - \ell'(\ell'+1)](\ell'+1) + 2\ell'(\ell'+1)\}$$

$$\int \frac{R_{n\ell} R_{n\ell'}}{r^3} dr = 0$$

or

$$(\ell'+1) [\ell(\ell+1) - \ell'(\ell'-1)] \int \frac{R_{n\ell} R_{n\ell'}}{r^3} dr = 0$$

which implies

$$\int \frac{R_{n\ell} R_{n\ell'}}{r^3} dr = 0 \quad \ell' > \ell+1.$$

All the remaining selection rules can be proven by considering commutators of the type

$$[H - \frac{\hbar^2}{2m} \frac{L^2}{r^2}, C_q^k \frac{1}{r} \frac{d^n r}{dr^n}] = 0,$$

and proceeding as above.

The next step is clearly to try to express the simple commutators above in terms of the generators of  $R(4)$ . In particular, if we consider

equations such as Eq. (5.5) with  $m=l$ ,  $m'=l'$ , we should be able to replace, in some fashion,  $\frac{d}{dr}$  with  $M_+$  (Eq. (5.2)). This approach provides a very encouraging method of studying the vanishing matrix elements; one can hope for early success in the use of  $R(4)$  symmetry to obtain selection rules on the radial matrix elements.

b) Symmetry Groups of Laguerre Polynomials.

This subject has been studied, in some detail by Miller.<sup>57</sup> We shall only mention here some of the major results of his work. He considers the general 4 dimensional complex Lie Algebra defined by

$$[J^+, J^-] = 2a^2 J^3 - bE; [J^3, J^+] = J^+;$$

$$[J^3, J^-] = -J^-; [J^+, E] = [J^-, E] =$$

$$[J^3, E] = 0.$$

for all complex  $a, b$ .

Clearly, if  $a=1$ ,  $b=0$ , one has the algebra for the complex three dimensional rotation group. Miller has shown that the basis functions for a realization in two variables of this algebra are confluent hypergeometric functions.

(The Laguerre polynomials are simply a special case of the confluent hypergeometric functions.) In addition, he finds that when  $b=1$ ,  $a=0$ , one also may construct basis functions from confluent hypergeometric functions. The algebra in this case is the complex form of the algebra of  $S_4$ . It would appear, at this time, that this latter group is of little value and we shall confine our attention to the case  $a=1$ ,  $b=0$ .

The realization in two variables of the algebra with  $a=1$ ,  $b=0$  ( $G(1,0)$ ) can be written

$$J^3 = \frac{\partial}{\partial y}, J^\pm = e^{\pm y} \left( \pm \frac{\partial}{\partial x} - k(x) \frac{\partial}{\partial y} + j(x) \right)$$

$$E = u,$$

where  $u$  is a complex constant;  $k(x)$  and  $j(x)$  must be determined so as to make the above operators satisfy the proper commutation relations. Miller finds two possible types of solutions for  $k(x)$  and  $j(x)$ :

Type A  $k(x) = \cot(x+p), j(x) = \frac{q}{\sin(x+p)}$

Type B  $k(x) = i, j(x) = qe^{-ix}$

where  $p, q$  are complex constants.<sup>58</sup> As an example, we consider Type B representations of the variety labelled  $D(u, m_0)$ . We first change coordinate systems by letting  $\tau = y - i\pi/2, z = -ie^{-ix}$ . Then

$$J^3 = \frac{\partial}{\partial \tau}, J^{\pm} = e^{\pm \tau} \left( z \frac{\partial}{\partial z} \pm \frac{\partial}{\partial \tau} \mp qz \right)$$

If the solution is written in the form  $f_m = Z_m e^{m\tau}$ , we find

$$\left( z \frac{d}{dz} + m - qz \right) Z_m = - (m - u) Z_{m+1}$$

$$\left( z \frac{d}{dz} - m + qz \right) Z_m = - (m + u) Z_{m-1}$$

which has solutions

$$Z_m = (2qz)^{u+1} e^{-qz} {}_1F_1(u-m+1; 2u+2; 2qz)$$

and

$$Z'_m = (2qz)^{-u} e^{-qz} {}_1F_1(-u-m; -2u; 2qz)$$

where  ${}_1F_1$  is a confluent hypergeometric function. In terms of Laguerre polynomials, we have

$$Z_m = (2qz)^{u+1} e^{-qz} L_{m-u-1}^{2u+1}(2qz)$$

$$Z'_m = (2qz)^{-u} e^{-qz} L_{m+u}^{-2u-1}(2qz).$$

This type of representation has  $u + m \neq \text{integer}$ .

Of greater interest to us are the basis states  $f_m$  for representation labelled  $\downarrow_u$ ; here

$$f_m = \frac{\Gamma(2u)n!}{\Gamma(n+2u)} L_n^{2u-1}(z) t^{u+n}$$

where  $u, n$ , are integers. Acting on this state with raising operators, one finds

$$J^+ L_n^{2u-1} \rightarrow L_{n+1}^{2u-1}.$$

Basically, this result implies that a basis for the representation  $\downarrow_u$  can be formed by the collection of states of the hydrogen atom obtained by holding  $l$  fixed and letting the principal quantum number run over all possible values. One can work out Clebsch-Gordan Coefficients for the Kronecker product  $\downarrow_u \times \downarrow_u$ , without too much difficulty.<sup>57</sup>

One therefore has the transformation properties of the hydrogenic radial wave functions with respect to the complex 3-dimensional rotation group. In order to search for the desired selection rules, one must determine the representation to which the operators  $1/r^s$  belong. This is not trivial and at the present time the solution is unknown.

This latter approach would appear to be more general and powerful than that of (a), but the problems involved are correspondingly more difficult. None the less, both approaches seem at the present to be rather hopeful.



APPENDIX 6

GROUP PROPERTIES OF HYDROGENIC RADIAL WAVEFUNCTIONS\*

Lloyd Armstrong, Jr.  
The Johns Hopkins University  
Baltimore, Maryland 21218

\*This work was partially supported by the U.S. Atomic Energy Commission.

Most contemporary studies of atomic structure depend heavily on the use of group theory. In the central field model of the atom, wavefunctions can be written as a product of an angular function and a radial function. The radial function is usually calculated through use of some variational technique (e. g. , Hartree-Fock) or simply treated in terms of a variable parameter; the angular portion is expressed in terms of products of spherical harmonics. It is to this angular portion of the wavefunction that group theory has traditionally been applied.<sup>59</sup>

Quite impressive simplifications have resulted from this application of groups to the angular wavefunction. For example, selection rules based on Kronecker products permit one to identify many matrix elements as being identically zero without explicit (and often laborious) calculation. Use of the Wigner-Eckart theorem often enables one to ascertain sets of angular matrix elements which are proportional to one another, thus saving a great deal of computational effort.

The use of group theory has been invaluable in advancing the understanding of angular wavefunctions and atomic shell structure to its present state. Unfortunately, although very impressive techniques have been developed in the last few years for the calculation of radial wavefunctions, very little has been done on the study of the symmetry properties of radial wavefunctions. Most of the group theoretical work which involves

radial wavefunctions has consisted of studies of hydrogen using  $O(4)$ ,  $O(4,1)$ , etc. In this case, however, the radial function has not been studied directly, since the basis functions for these groups are composed of a product of radial and angular parts.

We wish to report on a study of the group properties of the hydrogenic radial functions themselves. Two previous results suggested strongly that these functions should be amenable to a group-theoretic study. First, a well-known result of Pasternack and Sternheimer<sup>52</sup> shows that, for hydrogenic radial wavefunctions,

$$\int_0^{\infty} \frac{R_{n\ell} R_{n\ell'}}{r^s} dr = 0 \quad \begin{array}{l} \ell > \ell' \\ s = 2, 3, \dots, \ell - \ell' + 1 \end{array}$$

(we choose our radial wavefunction to be  $R_{n\ell}(r)/r$ ). This result is quite suggestive of a group-theoretical selection rule.

Second, the expectation values of  $r^n$  ( $n$  both positive and negative) evaluated with hydrogenic functions<sup>60</sup> can be seen to be proportional to Clebsch-Gordan coefficients<sup>61</sup> in which  $\ell$  plays the part of the angular momentum, and  $n$ , the projection of the angular momentum.

The group algebra pertinent to this study is formed by the operators

$$\begin{aligned} J_3 &= -i \frac{\partial}{\partial \tau} \\ J_{\pm} &= e^{\pm i\tau} \left( z \frac{\partial}{\partial z} \mp i \frac{\partial}{\partial \tau} \mp \frac{z}{2} \right) \end{aligned} \quad (1)$$

which satisfy the commutation relations

$$\begin{aligned} [J_+, J_-] &= 2J_3 \\ [J_3, J_{\pm}] &= \pm J_{\pm} \end{aligned} \quad (2)$$

(Operators of this same general type have been considered by Miller.<sup>57</sup>) We wish to construct functions  $f_{\ell n}$  such that

$$\begin{aligned} J_3 f_{\ell n} &= n f_{\ell n} \\ J_{\pm} f_{\ell n} &= [\ell(\ell+1) - n(n\pm 1)]^{\frac{1}{2}} f_{\ell, n\pm 1} \end{aligned} \quad (3)$$

A function satisfying Eqs. (3) is given by

$$f_{\ell n} = \left[ \frac{(n-\ell-1)! (2\ell+1)}{2\pi (n+\ell)!} \right]^{\frac{1}{2}} (i)^{n-\ell-1} e^{-z/2} z^{\ell+1} L_{n-\ell-1}^{2\ell+1}(z) e^{i n \tau} \quad (4)$$

where  $L_b^a$  is the Laguerre polynomial of Morse and Feshbach.<sup>62</sup>

For fixed  $n$ , this function is, of course, proportional to the radial wavefunction for hydrogen.<sup>62</sup> We define a Hilbert space as the space of functions  $f_{\ell n}$  with inner product

$$\langle f_{\ell n} | f_{\ell' n'} \rangle = \int f_{\ell n}^* f_{\ell' n'} d\Omega$$

where  $d\Omega = z^{-2} d\tau dz$ ; the parameter  $\tau$  can range from 0 to  $2\pi$ , the parameter  $z$  from 0 to  $\infty$ . One can easily show that

$$\langle f_{\ell n} | f_{\ell' n'} \rangle = \delta(\ell, \ell') \delta(n, n')$$

In addition, one has

$$\langle f_{\ell n} | J_{\pm} | f_{\ell' n'} \rangle = \langle J_{\mp} f_{\ell n} | f_{\ell' n'} \rangle$$

$$\langle f_{\ell n} | J_3 | f_{\ell' n'} \rangle = \langle J_3 f_{\ell n} | f_{\ell' n'} \rangle$$

Consideration of the operators shows that

$$J_- f_{\ell, \ell+1} = 0,$$

providing a lower bound to the set of functions  $f_{\ell n}$ ; clearly, there is no upper bound. The representation thus formed is infinite dimensional. It can also be shown to be irreducible, implying that the group described by the algebra (1) and (2) is non-compact.

We define a spherical tensor  $T_q^{(k)}$  by the relationships

$$\begin{aligned} [J_{\pm}, T_q^{(k)}] &= [k(k+1) - q(q \pm 1)]^{\frac{1}{2}} T_{q \pm 1}^{(k)} \\ [J_3, T_q^{(k)}] &= q T_q^{(k)}. \end{aligned} \quad (5)$$

This definition assures that the operators  $T_q^{(k)}$  transform in the same way as a state  $f_{kq}$ . Note, however, that the operators  $T_q^{(k)}$  (or the states  $f_{kq}$ ) with  $|q| \leq k$  form a finite dimensional representation of the algebra. We shall be concerned here only with operators of this type. Because of the transformation properties of the  $T^{(k)}$  we can use the Wigner-Eckart theorem to show that

$$\langle f_{\ell n} | T_q^{(k)} | f_{\ell' n'} \rangle = A(kq, \ell' n' | \ell n) (\ell \| T^{(k)} \| \ell') \quad (6)$$

where  $(\ell \| T^{(k)} \| \ell')$  is a reduced matrix element which is independent of  $q, n'$ , and  $n$ ; and  $A(kq; \ell'n' | \ell n)$  is a coefficient which depends on the transformation properties of  $f_{\ell n}$ ,  $f_{\ell' n'}$ , and  $T^{(k)}_q$  but not on their explicit form. One can determine the coefficients  $A$  following the technique of Racah.<sup>63</sup> By considering the matrix elements of  $[J_{\pm}, T^{(k)}_q]$  between the states  $\langle f_{\ell n} |$  and  $| f_{\ell' n'} \rangle$ , and the coupling of states  $f_{\ell' n'}$  and  $f_{kq}$  to a state  $f_{\ell n}$ , one can easily obtain recursion relations which demonstrate that the dependence of  $A(kq, \ell'n' | \ell n)$  on  $k, q, \ell', n', \ell$  and  $n$  is identical to the dependence of the algebraic form of the Clebsch-Gordan coefficient  $(kq, \ell'n' | \ell n)$  on the same quantum numbers. The  $A$  coefficient is not strictly identical to the corresponding Clebsch-Gordan coefficient, however, since in the present case  $n > \ell$ ,  $n' > \ell'$ , values for which the Clebsch-Gordan coefficient vanishes identically. Nonetheless, one can obtain an algebraic expression for  $A(kq, \ell'n' | \ell n)$  for a fixed  $k$  and  $q$ , and general  $\ell', n', \ell, n$  by determining the algebraic expression for the equivalent Clebsch-Gordan coefficient and relaxing the restriction that  $|n'| < \ell'$ ,  $|n| < \ell$ .

Changing for convenience from Clebsch-Gordan to 3-j symbols, we can write

$$\langle f_{\ell n} | T^{(k)}_q | f_{\ell' n'} \rangle = (-1)^{\ell-n} \begin{pmatrix} \ell & k & \ell' \\ -n & q & n' \end{pmatrix}_a (\ell \| T^{(k)} \| \ell') \quad (7)$$

where the subscripted 3-j symbol refers to the algebraic form of the usual 3-j symbol with the restrictions on the range of  $n$  and  $n'$  relaxed. Algebraic forms of certain 3-j symbols have been given by e. g., Edmonds<sup>61</sup> and Falkoff et al.<sup>64</sup>.

We now consider the tensorial ranks of the operators  $e^{im\tau}/r^N$  ( $N \geq 0$ ). By using Eqs. (5), one can easily show that such an operator corresponds to the  $m$ th component of a tensor of rank  $N$ ,  $T_m^{(N)}$ . By relating the function (4) to the radial wavefunction of hydrogen, we can therefore make the identification ( $N > 1$ )

$$\int \frac{R_{nl} R_{n'l'}}{r^N} dr = \frac{1}{2n} \left(\frac{2z}{n}\right)^N \frac{(-1)^{l-n} (+i)^{l'-l}}{[(2l+1)(2l'+1)]^{\frac{1}{2}}} \begin{pmatrix} l & N-2 & l' \\ -n & 0 & n' \end{pmatrix}_a$$

$$(l \| T^{(N-2)} \| l')$$
(8)

One notes immediately that the selection rules of Pasternack and Sternheimer<sup>52</sup> are contained in the triangular selection rules of the 3-j symbol contained in Eq. (8).

The proportionality of expectation values of  $r^{-N}$  to 3-j symbols is also made obvious by Eq. (8).

In order to fully utilize Eq. (8) one must be able to evaluate the pertinent reduced matrix elements. This is easily done: assume that  $\ell \geq \ell'$ , and consider matrix elements in which the bra is the state  $\langle f_{\ell, \ell+1} |$ . Then, for example

$$\begin{aligned} \langle f_{\ell, \ell+1} | T^{(k)}_0 | f_{\ell', \ell'+1} \rangle &= - \begin{pmatrix} \ell & k & \ell' \\ -(\ell+1) & 0 & \ell'+1 \end{pmatrix}_a (\ell \| T^{(k)} \| \ell') \\ &= \left[ \frac{(\ell-\ell')! (2\ell+1)(2\ell'+1)}{(2\ell+1)! (\ell+\ell'+1)! 3} \right]^{\frac{1}{2}} (i)^{\ell-\ell'} \int e^{-z} z^{\ell+\ell'-k} L_{\ell-\ell'}^{2\ell'+1}(z) dz \quad (9) \end{aligned}$$

The integral above can be simply evaluated, as can the 3-j symbol. One then obtains

$$\begin{aligned} (\ell \| T^{(k)} \| \ell') &= (i)^{\ell-\ell'} [(-1)^{\ell-\ell'}]^{-\frac{1}{2}} \\ &\quad \left[ \frac{(2\ell+1)(2\ell'+1)k!^2 (\ell+\ell'-k)!}{(k+\ell+\ell'+1)! (\ell-\ell'+k)! (\ell+k-\ell')!} \right]^{\frac{1}{2}} \quad (10) \end{aligned}$$



Use of these expressions in conjunction with algebraic forms of 3-j symbols leads immediately to the known expectation values  $r^{-N}$  (N positive).

This successful application of the techniques of group theory to a study of radial wavefunctions suggests strongly that such studies of more complicated radial functions may be possible. In addition, it is particularly gratifying to demonstrate that the radial and angular parts of the atomic wavefunction can be placed on a more even footing and treated theoretically using the same general techniques.

The author gratefully acknowledges invaluable discussions with Professors B. R. Judd and G. Domokos.

#### REFERENCES

1. I. Liberman, et al., "Optical Pumps for Lasers-Phase II," Contract No. DA-28-043-AMC-02097(E), AD679143, Ft. Monmouth, New Jersey (1968).
2. C. H. Church, et al., "Arc Discharge Sources," Contract Nonr 4647(00) (1967).
3. C. H. Church, R. G. Schlecht and I. Liberman, J. Quant. Spectrosc. Rad. Trans., 8, 403 (1968).
4. H. R. Griem, Plasma Spectroscopy, McGraw-Hill Book Co., New York (1964).
5. W. P. White, S. M. Johnson and G. B. Danzig, J. Chem. Phys., 28, 751 (1958).
6. R. J. Duffin, E. L. Peterson and C. M. Zener, Geometric Programming: Theory and Application, John Wiley and Sons, New York (1967).
7. J. M. Yos, AVCO Technical Memorandum RAD-TM-63-7, AD435053 (1963).
8. R. S. Brokaw, J. Chem. Phys., 32, 1005 (1960).
9. L. S. Frost and A. V. Phelps, Phys. Rev., 136, A1538 (1964).
10. L. Spitzer, Jr., Physics of Fully Ionized Gases, Interscience Publishers, New York (1956).
11. R. S. Brokaw, NASA TR R-81 (1960).
12. R. S. Devoto (private communication, also see Ref. 2).
13. R. S. Devoto, AIAA 7, 199 (1969).
14. R. S. Devoto, Phys. of Fluids 10, 354 (1967).
15. C. E. Moore, Atomic Energy Levels III, NBS, U. S. Govt. Print. Off. (1958).
16. C. E. Moore, Atomic Energy Levels III, NBS, U. S. Govt. Print. Off. (1952).

17. R. D. Cowan, J. Opt. Soc. Am., 58, 808 (1968).
18. D. R. Bates and A. Damgaard, Phil. Trans. Roy. Soc., London A242, 101 (1949).
19. P. W. Murphy, "Transition Probabilities in the Spectra of Neon I, Argon I, and Krypton I," Technical Note BN-523, University of Maryland (1967).
20. A. Unsöld, Ann. Phys. Lpz., 33, 607 (1938).
21. D. Schlüter, Z. Phys., 210, 80 (1968).
22. L. M. Biberman, G. E. Norman, and K. N. Ulyanov, Soviet Astron., AJ6, 77 (1963).
23. V. V. Yankov, Opt. and Spectr., 14, 14 (1963).
24. J. J. Lowke, J. App. Phys., (1970).
25. H. Mottschmann, Z. Phys., 214, 42 (1968).
26. I. Liberman and R. L. Grassel, Appl. Optics, 8, 1875 (1969).
27. M. Pivovonsky, and M. R. Nagel, Tables of Blackbody Radiation Functions, The Macmillan Co., New York (1961).
28. J. A. Koningstein and J. E. Gausic, Phys. Rev. 136, A711 (1964).
29. T. H. Maiman, Brit. Commun. Elect. 7, 674 (1960).
30. T. H. Maiman, Nature 187, 493 (1960).
31. C. H. Church, R. G. Schlecht and I. Liberman, J. Quant. Spectrosc. Radiat. Transfer 8, 403 (1968).
32. T. H. Maiman, R. H. Hoskins, I. J. D'Haenens, C. K. Asawa and V. Eutuhov, Phys. Rev. 123, 1151 (1961).
33. D. M. Doff, D. L. Wood and R. L. Barnes, J. Appl. Phys. 35, 1183 (1964).
34. E. E. Bukke and Z. L. Morgenshtern, Optics and Spectros. 14, 362 (1963).

35. For example the Korad K1500 Q-switched ruby oscillator-amplifier has a laser system efficiency of 0.01%.
36. T. H. Maiman, Phys. Rev. Letters 4, 564 (1960).
37. J. W. Huang and H. W. Moos, Phys. Rev. 173, 440 (1968).
38. J. B. Mann, "Atomic Structure Calculations I. Hartree-Fock Energy Results for the Elements Hydrogen to Lawrencium," LA-3690, Los Alamos (1967).
39. N. C. Handy, M. T. Marron and H. J. Silverstone, Phys. Rev., 180, 45 (1969).
40. J. C. Slater, Quantum Theory of Atomic Structure. I, McGraw-Hill Book Co., New York (1960).
41. G. Burns, J. Chem. Phys., 41, 1521 (1964).
42. E. Clementi and D. L. Raimondi, J. Chem. Phys., 38, 2686 (1963).
43. L. I. Schiff, Quantum Mechnaics, 85 McGraw-Hill Book Co., New York (1955).
44. P. Löwdin, Phys. Rev., 90, 120 (1953).
45. W. Kauzmann, Quantum Chemistry, 334, Academic Press, New York (1957).
46. I. Shavitt, Methods in Computational Physics. II, Academic Press, New York (1963).
47. F. Herman and S. Skillman, Atomic Structure Calculations, Prentice-Hall, Englewood Cliffs, New Jersey (1963).
48. J. B. Mann, "Atomic Structure Calculations II. Hartree-Fock Wavefunctions and Radial Expectation Values: Hydrogen to Lawrencium," LA-3691, Los Alamos (1968).
49. M. Abramowitz and I. A. Stegun, Handbook of Mathematical Functions, NBS Applied Mathematics Series No. 55 (1964).
50. A. H. Stroud and D. Secrest, Gaussian Quadrature Formulas, Prentice-Hall, Englewood Cliffs, New Jersey (1966).

51. V. I. Pukhov, Sov. Phys. (Tech. Phys.) 1, 1055 (1956).
52. S. Pasternack and R. M. Sternheimer, J. Math. Phys. 3, 1280 (1962).
53. M. Bander and C. Itzykson, Rev. Mod. Phys. 38, 330, 346 (1966).
54. L. Infeld and T. E. Hull, Rev. Mod. Phys. 23, 21 (1951).
55. Z. W. Salsborg, Am. J. Phys. 33, 36 (1965).
56. This particular result has also been obtained via another method by G. Feinberg, Phys. Rev. 112, 1637 (1958).
57. W. Miller, Lie Theory and Special Functions, Academic Press, New York (1968).
58. This classification is based on the work of Infeld and Hull (reference 54).
59. B. R. Judd, Operator Techniques in Atomic Spectroscopy, McGraw-Hill Book Co., New York (1963).
60. H. A. Bethe and E. E. Salpeter, Quantum Mechanics of One- and Two-Electron Atoms, Academic Press, New York (1957).
61. A. R. Edmonds, Angular Momentum in Quantum Mechanics, Princeton University Press, Princeton, New Jersey (1957).
62. P. M. Morse and H. Feshbach, Methods of Theoretical Physics, Vols. I and II, McGraw-Hill Book Co., New York (1953).
63. G. Racah, Phys. Rev. 62, 438 (1942).
64. D. L. Falkoff, G. S. Holladay and R. E. Sells, Can. J. Phys. 30, 253 (1952).

TABLE I. The Measured Energy Levels<sup>15</sup> and SLJ Labels for the Lowest Five Configurations of Xe I.

The core configuration is always  $5p^5(^2P)$  and therefore is not listed.

n'l'	SLJ	E(cm <sup>-1</sup> )	n'l'	SLJ	E(cm <sup>-1</sup> )
5p	1s <sub>0</sub>	0	5d	3p <sub>0</sub>	79,772
6s	3p <sub>2</sub>	67,068		3d <sub>1</sub>	79,987
	3p <sub>1</sub>	68,046		3f <sub>4</sub>	80,197
	3p <sub>0</sub>	76,197		3f <sub>2</sub>	80,323
	1p <sub>1</sub>	77,186		3f <sub>3</sub>	80,971
6p	3d <sub>1</sub>	77,270		3d <sub>2</sub>	81,926
	3d <sub>2</sub>	78,120		3d <sub>3</sub>	82,431
	3d <sub>3</sub>	78,404		3p <sub>1</sub>	83,890
	3p <sub>1</sub>	78,957		3p <sub>2</sub>	91,153
	3p <sub>2</sub>	79,213		1d <sub>2</sub>	91,448
	3p <sub>0</sub>	80,119		1f <sub>3</sub>	91,747
	3s <sub>1</sub>	88,380		1p <sub>1</sub>	93,619
	1d <sub>2</sub>	89,163	7s	3p <sub>2</sub>	85,189
	1p <sub>1</sub>	89,279		3p <sub>1</sub>	85,441
	1s <sub>0</sub>	89,861		3p <sub>0</sub>	95,721
				1p <sub>1</sub>	95,801

TABLE II. The Measured Energy Levels<sup>16</sup> and SLJ Labels for Fourteen Configurations of Kr I.

The core configuration is always  $4p^5(^2P)$  and therefore is not listed. The values in parentheses are approximate values.

n'l'	SLJ	E(cm <sup>-1</sup> )	n'l'	SLJ	E(cm <sup>-1</sup> )
4p	<sup>1</sup> S <sub>0</sub>	0	6s	<sup>3</sup> P <sub>2</sub>	99,628
5s	<sup>3</sup> P <sub>2</sub>	79,973		<sup>3</sup> P <sub>1</sub>	99,895
	<sup>3</sup> P <sub>1</sub>	80,918		<sup>3</sup> P <sub>0</sub>	105,092
	<sup>3</sup> P <sub>0</sub>	85,192		<sup>1</sup> P <sub>1</sub>	105,147
	<sup>1</sup> P <sub>1</sub>	85,848	6p	<sup>3</sup> D <sub>1</sub>	102,888
5p	<sup>3</sup> D <sub>1</sub>	91,169		<sup>3</sup> D <sub>3</sub>	103,116
	<sup>3</sup> D <sub>3</sub>	92,295		<sup>3</sup> D <sub>2</sub>	103,122
	<sup>3</sup> D <sub>2</sub>	92,308		<sup>3</sup> P <sub>1</sub>	103,314
	<sup>3</sup> P <sub>1</sub>	92,965		<sup>3</sup> P <sub>2</sub>	103,363
	<sup>3</sup> P <sub>2</sub>	93,124		<sup>3</sup> P <sub>0</sub>	103,762
	<sup>3</sup> P <sub>0</sub>	94,094		<sup>3</sup> S <sub>1</sub>	108,439
	<sup>3</sup> S <sub>1</sub>	97,597		<sup>1</sup> P <sub>1</sub>	108,515
	<sup>1</sup> P <sub>1</sub>	97,920		<sup>1</sup> D <sub>2</sub>	108,569
	<sup>1</sup> D <sub>2</sub>	97,946		<sup>1</sup> S <sub>0</sub>	108,822
	<sup>1</sup> S <sub>0</sub>	98,856	5d	<sup>3</sup> D <sub>1</sub>	103,803
4d	<sup>3</sup> P <sub>0</sub>	96,772		<sup>3</sup> P <sub>0</sub>	104,074
	<sup>3</sup> D <sub>1</sub>	97,086		<sup>3</sup> F <sub>4</sub>	104,631
	<sup>3</sup> F <sub>2</sub>	97,689		<sup>3</sup> F <sub>3</sub>	104,917
	<sup>3</sup> F <sub>4</sub>	97,798		<sup>3</sup> F <sub>2</sub>	105,008
	<sup>3</sup> F <sub>3</sub>	98,227		<sup>3</sup> D <sub>2</sub>	105,164

TABLE II. (Continued)

$n'l'$	SLJ	$E(\text{cm}^{-1})$	$n'l'$	SLJ	$E(\text{cm}^{-1})$
4d	$^3D_2$	98,868	5d	$^3D_3$	105,209
	$^3D_3$	99,080		$^3P_1$	105,649
	$^3P_1$	99,647		$^1D_2$	110,104
	$^1D_2$	103,267		$^3P_2$	110,123
	$^3P_2$	103,443		$^1F_3$	110,238
	$^1F_3$	103,702		$^1P_1$	110,734
	$^1P_1$	104,888			
7s	$^3P_2$	105,648	9s	$^3P_2$	109,753
	$^3P_1$	105,772		$^3P_1$	109,780
	$^3P_0$	(111,004)		$^3P_0$	(115,128)
	$^1P_1$	111,004		$^1P_1$	115,128
4f	$^3D_1$	105,965	10s	$^3P_2$	110,609
	$^3F_2$	105,966		$^3P_1$	110,620
	$^3G_5$	105,990		$^3P_0$	(115,961)
	$^3G_4$	(105,990)		$^1P_1$	115,961
	$^3G_3$	106,022	11s	$^3P_2$	111,155
	$^3D_2$	106,022		$^3P_1$	111,172
	$^3F_3$	106,048		$^3P_0$	(116,527)
	$^3F_4$	106,048		$^1P_1$	116,527
	$^1G_4$	111,379	12s	$^3P_2$	111,529
	$^3D_3$	111,379		$^3P_1$	111,537



Table II. (Continued)

$n'l'$	SLJ	$E(\text{cm}^{-1})$	$n'l'$	SLJ	$E(\text{cm}^{-1})$
4f	$1F_3$	111,381	12s	$3P_0$	(116,904)
	$1D_2$	111,382		$1P_1$	116,904
8s	$3P_2$	108,326			
	$3P_1$	108,374			
	$3P_0$	(113,711)			
	$1P_1$	113,711			

TABLE III. The Intermediate Coupling Wave Functions for the Five Lowest Configurations of Xe I.  
The core configuration is always  $5p^5(^2P)$ .

J	n'l'	SL	Eigenvectors		
0	6p	$^3P$	0.782	-0.624	
		$^1S$	0.624	0.782	
1	6s	$^3P$	0.754	-0.657	
		$^1P$	0.657	0.754	
		$^3D$	0.155	0.860	0.482
		$^3P$	-0.766	-0.148	0.445
	6p	$^3S$	0.491	-0.135	-0.047
		$^1P$	0.384	-0.470	0.753
		$^3D$	0.139	0.947	0.290
		$^3P$	-0.683	-0.121	0.720
		$^1P$	0.717	-0.298	0.630
2	7s	$^3P$	0.807	-0.590	
		$^1P$	0.590	0.807	
	6p	$^3D$	0.658	-0.246	-0.712
		$^3P$	0.480	0.865	0.145
		$^1D$	0.581	-0.437	0.687

TABLE III (Cont)

J	n'l'	SL	Eigenvectors			
	5d	3F	0.462	0.784	0.410	-0.060
		3D	-0.607	0.093	0.584	0.531
		3P	0.374	-0.593	0.679	-0.216
		1D	0.527	-0.160	-0.170	0.817
3	5d	3F	-0.206	0.627	0.752	
		3D	0.730	0.610	-0.309	
		1F	0.652	-0.485	0.583	

TABLE IV. The intermediate coupling wave functions for fourteen configurations of KrI. The core configuration is always  $4p^5(2P)$ .

J	n'l'	SL	Eigenvectors			
0	5p	$^3P$	0.738	-0.675		
		$^1S$	0.675	0.738		
	6p	$^3P$	0.786	-0.618		
		$^1S$	0.618	0.786		
1	5s	$^3P$	0.717	-0.697		
		$^1P$	0.697	0.717		
	5p	$^3D$	0.192	0.908	0.370	0.027
		$^3P$	0.725	0.059	-0.487	-0.484
		$^3S$	0.482	-0.068	-0.147	0.861
		$^1P$	0.453	-0.408	0.777	-0.153
	4d	$^3D$	0.144	0.961	0.237	
		$^3P$	-0.712	-0.065	0.699	
		$^1P$	0.687	-0.269	0.675	
	6s	$^3P$	0.798	-0.603		
		$^1P$	0.603	0.798		
	6p	$^3D$	0.225	0.843	0.486	0.045
		$^3P$	-0.767	-0.091	0.474	0.424
		$^3S$	0.474	-0.151	-0.038	0.867
		$^1P$	0.370	-0.508	0.733	-0.259
	5d	$^3D$	0.173	0.945	0.277	
		$^3P$	0.766	0.048	-0.641	

TABLE IV. (Continued)

J	n'l'	SL	Eigenvectors			
2	7s	$1_P$	0.620	-0.323	0.716	
		$3_P$	0.809	-0.588		
		$1_P$	0.588	0.809		
	8s	$3_P$	0.814	-0.581		
		$1_P$	0.581	0.814		
	9s	$3_P$	0.815	-0.580		
		$1_P$	0.580	0.815		
	10s	$3_P$	0.816	-0.578		
		$1_P$	0.578	0.816		
	11s	$3_P$	0.815	-0.579		
		$1_P$	0.579	0.815		
	12s	$3_P$	0.816	-0.578		
		$1_P$	0.578	0.816		
	5p	$3_D$	0.653	-0.208	-0.728	
		$3_P$	0.477	0.860	0.181	
		$1_D$	0.589	-0.466	0.661	
	4d	$3_F$	0.357	0.844	0.401	-0.015
		$3_D$	-0.615	0.024	0.518	0.594
		$3_P$	0.373	0.081	-0.472	0.795
	6p	$1_D$	0.596	-0.530	0.590	0.124
		$3_D$	0.653	-0.265	-0.709	
		$3_P$	0.483	0.867	0.121	

TABLE IV. (Continued)

J	n'l'	SL	Eigenvectors			
3	5d	$1_D$	0.583	-0.422	0.694	
		$3_F$	0.372	0.795	0.479	0.009
		$3_D$	-0.658	-0.014	0.524	0.541
		$3_P$	0.447	-0.034	-0.307	0.840
		$1_D$	0.479	-0.605	0.634	-0.047
	4f	$3_F$	0.617	0.786	0.021	
		$3_D$	-0.539	0.404	0.739	
		$1_D$	0.573	-0.467	0.674	
	4d	$3_F$	-0.493	0.292	0.819	
		$3_D$	0.610	0.788	0.086	
		$1_F$	0.620	-0.542	0.567	
	5d	$3_F$	-0.620	0.200	0.759	
		$3_D$	0.520	0.829	0.206	
		$1_F$	0.588	-0.522	0.617	
	4f	$3_G$	0.485	0.674	0.558	-0.001
		$3_F$	-0.652	0.001	0.566	0.505
		$3_D$	0.336	0.073	-0.380	0.859
		$1_F$	-0.477	0.735	-0.474	-0.086
		$3_G$	-0.750	-0.011	0.661	
4	4f	$3_F$	0.327	0.863	0.386	
		$1_G$	0.575	-0.505	0.643	

TABLE V. The values of Slater integrals and spin-orbit coupling constants which was determined by fitting the theoretical energy levels to the measured levels. The parameters and the rms deviation,  $\sigma$ , of the fit are given in  $\text{cm}^{-1}$ .

Atom	n'l'	F <sub>0</sub>	F <sub>2</sub>	G <sub>0</sub>	G <sub>1</sub>	G <sub>2</sub>	G <sub>3</sub>	G <sub>4</sub>	δ <sub>n1</sub>	δ <sub>n'l'</sub>	δ
Xe	6s	71040			951				6239		233
	6p	81866	173	629		33			7005	382	105
	5d	84161	186		298		28		6892	-175	191
	7s	88875			175				7001		32
Kr	5s	82512			800				3482		4
	5p	94118	176	650		42			3538	153	46
	4d	99747	175		177		14		3501	- 35	138
	6s	101626	176						3608		54
	6p	104922	45	204		13			3556	60	17
	5d	106520	105		88		6		3539	11	245
	7s	107507			73				3545		40
	4f	107800	4			0		0	3580	0	1
	8s	110150			29				3580		16
	9s	111561			16				3578		8
	10s	112399			6				3566		3
	11s	112956			10				3578		5
	12s	113326			5				3582		3

TABLE VI. The transition probability rates  $A_{mn}$  for emission between the energy levels of the five lowest configurations of Xe I and between the energy levels of fourteen configurations of Kr I. The core configuration is always  $5p^5(^2P)$  and  $4p^5(^2P)$  for xenon and krypton, respectively. Only values of  $A_{mn}$  larger than  $0.1 \times 10^8 \text{ sec}^{-1}$  was listed.

Atom	State n		State m		$\lambda$ Å	$A_{mn}$ $10^8 \text{ sec}^{-1}$
	n'l'	SLJ	n''l''	SLJ		
Xe	5p	$1s_0$	7s	$1p_1$	1044	0.9
			5d	$1p_1$	1068	27.8
			7s	$3p_1$	1170	1.1
			5d	$3p_1$	1192	13.0
				$3d_1$	1250	1.1
			6s	$1p_1$	1296	5.2
				$3p_1$	1470	3.9
	6s	$3p_0$	6p	$1p_1$	7644	0.3
				$1s_0$	7890	0.4
				$3s_1$	8209	0.1
				$3p_2$	8234	0.3
				$1p_1$	8269	0.1
				$3p_0$	8282	0.4
				$1d_2$	8349	0.4
				$3d_3$	8822	0.3
				$3s_1$	8933	0.2
				$3p_2$	8955	0.1
				$3d_2$	9048	0.1



TABLE VI. (Continued)

Atom	State n		State m		$\lambda$ Å	$A_{mn}$ $10^8 \text{ sec}^{-1}$
	n'l'	SLJ	n'l''	SLJ		
Kr	4p	$3P_1$		$3P_1$	9165	0.3
		$3P_2$		$3D_1$	9802	0.2
		$3P_1$		$3D_2$	9926	0.2
		$1S_0$	6s	$1P_1$	951	0.8
			4d	$1P_1$	953	11.9
			6s	$3P_1$	1001	1.1
			4d	$3P_1$	1004	9.9
				$3D_1$	1030	1.2
			5s	$1P_1$	1165	4.7
				$3P_1$	1236	3.9
	5s	$3P_1$	5p	$3P_0$	7589	0.5
		$3P_2$		$3P_2$	7604	0.3
		$1P_1$		$1S_0$	7687	0.4
		$3P_0$		$1P_1$	7857	0.2
	5p	$3D_1$	5d	$3D_1$	7916	0.1
	5s	$3P_0$	5p	$3S_1$	8062	0.2
		$3P_2$		$3D_2$	8107	0.1
				$3D_3$	8115	0.4
		$3P_1$		$3P_2$	8192	0.1
		$1P_1$		$1D_2$	8266	0.4
				$1P_1$	8283	0.2

TABLE VI. (Continued)

Atom	State n		State m		$\lambda$ Å	$A_{mn}^{8mn}$ $10^8 \text{ sec}^{-1}$
	n'l'	SLJ	n''l''	SLJ		
		$3P_1$		$3P_1$	8300	0.3
		$1P_1$		$3S_1$	8511	0.2
		$3P_1$		$3D_2$	8779	0.2
		$3P_2$		$3D_1$	8931	0.2

Table VII. Comparisons of the four lamps pumping a 0.7% Nd:YAG slab.  
 $P_{in}$  is the electrical power density into the lamp and  $P_{out}$   
is the power density out of the laser slab.

Lamp	$P_{in}$ Watts/cm <sup>2</sup>	t = 0.6 cm				t = 4.0 cm				t = 0.84 cm			
		Lamp Effi- ciency %	Slab Effi- ciency %	Pump Effi- ciency %	$P_{out}$ Watts/cm <sup>2</sup>	Slab Effi- ciency %	Pump Effi- ciency %	$P_{out}$ Watts/cm <sup>2</sup>	$E_o$ 10 <sup>-2</sup> %	Measured Laser Effi- ciency, %	Calculated Pump Effi- ciency, %		
K-Hg	52	67.1	13.5	9.1	4.7	29.9	20.1	10.3	6.23	13.0*	10.8		
W	200	35.5	6.3	2.2	4.4	15.1	5.4	10.7	1.48	3.8	2.7		
Kr	192	13.9	15.4	2.1	4.0	37.4	5.2	10.0	1.28	3.7	2.6		
Xe	226	35.2	3.4	1.2	2.7	12.1	4.3	9.6	0.64	3.1	1.5		

\*Estimated from incomplete experimental data.

TABLE VIII. A comparison of accuracy and speed of different integration methods for the evaluation of orthonormality and Slater integrals for the Cu 4s electron.

Two Laguerre integrations with  $n = 15$  ( $L_{15}$ ) and  $n = 48$  ( $L_{48}$ ) are compared with Simpson's rule of integration. The per cent errors in the  $G^k$  values for the  $L_{15}$  integration were invalidated by a programming error and are not given. However, the quoted execution times are for the evaluation of all integrations. Only errors larger than 0.1% are listed.

n'l'	Integration Method	Absolute Error in Orthogonality Integral	Per Cent Errors				Execution Time In Seconds
			F°	G°	G <sup>1</sup>	G <sup>2</sup>	
4s*	L <sub>15</sub>		20.3				
	L <sub>48</sub>		0.1				
	S		0.1				
3d	L <sub>15</sub>		1.4				0.7
	L <sub>48</sub>					1.6	6.2
	S					0.6	32.8
3p	L <sub>15</sub>		0.5				0.6
	L <sub>48</sub>				2.0		5.7
	S				0.5		30.3
3s	L <sub>15</sub>	$2 \times 10^{-5}$	0.6				0.5
	L <sub>48</sub>	$<10^{-6}$		1.0			5.1
	S	$<10^{-6}$		0.2			27.0
2s	L <sub>15</sub>	$1 \times 10^{-3}$	2.9				0.5
	L <sub>48</sub>	$<10^{-6}$		3.1			4.9
	S	$7 \times 10^{-5}$		0.1			27.0
1s	L <sub>15</sub>	$4 \times 10^{-3}$	12.4				1.3
	L <sub>48</sub>	$<10^{-6}$		8.8			4.9
	S	$<10^{-6}$		0.3			26.7

\* These execution times are included in Table IX.

TABLE IX. A comparison of accuracy and speed of different integration methods for the evaluation of  $\langle r^n \rangle$  radial integrals for the Cu 4s electron. Two Laguerre integrations with  $n = 15$  ( $L_{15}$ ) and  $n = 48$  ( $L_{48}$ ) are compared to the trapezoidal rule (T) and Simpson's rule integration (S). The accuracy is given in per cent. Errors less than 0.1% are not listed.

Integration Method	n in $\langle r^n \rangle$							Execution Time in Seconds*
	-2	-1	0	1	2	4	6	
$L_{15}$	10.1	2.0					0.1	0.7
$L_{48}$								3.3
T	6.4	0.1	0.1	0.1	0.1	0.1	0.1	13.9
S	4.5							15.0

\* Includes the calculation of  $F^0$ .

TABLE X. The screening constants proposed by Burns.<sup>41</sup>

$\ell$	$\ell, n'$	$n - 1$	$n$	$n + 1$
s	s	0.90	0.40	0.10
	p	0.75	0.35	0.10
	d	0.50	0.35	0.10
	f	0.40	0.20	
p	s	1.00	0.50	
	p	0.90	0.35	
	d	0.70	0.35	
	f	0.30	0.20	
d	s	1.00	0.75	0.15
	p	1.00	0.50	0.05
	d	0.90	0.35	0.05
	f	1.00	0.20	
f	s	1.00	1.00	0.50
	p	1.00	0.75	0.15
	d	0.85	0.50	
	f	1.00	0.35	

TABLE XI. Average screening constants obtained from Mann's binding energies.<sup>38</sup>

$\ell$	$\ell' \backslash n'$	$n - 2$	$n - 1$	$n$	$n + 1$	$n + 2$	$n + 3$	$n + 4$	$n + 5$	$n + 6$
s	s	1.000	0.875	0.644	0.133	0.157	0.141	0.103	0.062	0.025
	p	1.000	0.776	0.505	0.286	0.200	0.130	0.070	0.028	
	d	1.000	0.918	0.560	0.321	0.183	0.115	0.062	0.025	
	f	0.982	0.884	0.610	0.354	0.186	0.072	0.029		
p	s	1.000	1.000	0.397	0.079	0.150	0.162	0.135	0.085	
	p	1.000	1.000	0.706	0.308	0.237	0.168	0.105		
	d	1.000	0.936	0.576	0.322	0.220	0.150	0.095		
	f	1.000	0.918	0.628	0.358	0.187	0.106			
d	s	1.000	1.000	1.000	-0.134	0.038	0.148	0.155		
	p	1.000	1.000	1.000	0.231	0.235	0.198			
	d	1.000	1.000	0.747	0.313	0.237	0.175			
	f	1.000	0.996	0.661	0.362	0.224				
f	s	1.000	1.000	1.000	1.000	0.020	0.020			
	p	1.000	1.000	1.000	0.801	0.113				
	d	1.000	1.000	1.000	0.218	0.120				
	f	1.000	1.000	0.866	0.352					

TABLE XII. Hartree-Fock values of radial integrals involving the Cu 4s wave function.<sup>38,48</sup>

Slater Integrals between 4s and n'l' Wave Functions				4s Radial Integrals	
n'l'	F <sup>o</sup>	k	G <sup>k</sup>	n	<r <sup>n</sup> >
4s	.5450896			-2	.8077270
3d	.7122117	2	.0636135	-1	.3822107
3p	.7235111	1	.0232793	0	1.000000
3s	.7248400	0	.0164793	1	3.331133
				2	13.08433
				4	310.3408
				6	12034.72



TABLE XIII. Initial and final Slater parameters for four different three-term expansions. The final parameters are the values after 100 seconds of computing time. The standard deviation is between the five true radial integrals and the five calculated radial integrals.

Description	Expansion Set No.	m	nl	$a_m$		$A_m$		Standard Deviation	
				Initial	Final	Initial	Final	Initial	Final
Switched Input	1	1	4s	0.53	0.26	0.70	2.15		
		2	3d	0.50	0.84	-0.50	-1.49		
		3	3p	1.25		1.03	-0.31	8.983	0.069
Optimized Set	2	1	4s	0.22	0.23	-0.64	-0.71		
		2	3d	0.21	0.35	2.27	0.35		
		3	3p	0.23		-0.79	1.21	0.871	0.052
Burns	3	1	4s	0.53	0.16	0.70	1.11		
		2	3d	1.03	3.46	-0.50	0.23		
		3	3p	1.25		0.50	-0.59	0.559	0.041
Mann	4	1	4s	0.20	0.11	0.95	-1.38		
		2	3d	0.29	0.28	0.23	2.21		
		3	3p	0.72		-0.23	0.14	0.187	0.030

TABLE XIV. Initial and final Slater parameters for three different five-term expansions. The final parameters for the first three sets are the result of 100 seconds of computing time. Set no. 8 is the continuation of set no. 7. The standard deviation is between the five true radial integrals and the five calculated radial integrals.

Description	Expansion Set No.	m	nl	$a_m$	$A_m$		Standard Deviation	
					Initial	Final	Initial	Final
Mann	5	1	3d	0.29	0.90	0.70		
		2	4s	0.20	0.43	-0.44		
		3	3s	0.91	-0.09	-0.10		
		4	2s	2.60	0.03	0.03		
		5	1s	7.39	-0.01	-0.01	0.554	0.032
$a_m$ Peaked	6	1	3d	0.10	0.23	-0.41		
		2	4s	0.11	0.94	-0.60		
		3	3s	0.47	-0.23	-0.02		
		4	2s	1.43	0.07	0.07		
		5	1s	8.33	-0.01	-0.01	1.321	0.030
$p_m$ Peaked	7	1	3s	0.47	0.23	0.42		
		2	4p	0.23	0.94	0.97		
		3	3p	0.93	-0.23	-0.67		
		4	2p	2.86	0.07	0.06		
		5	1s	8.33	-0.01	-0.03	0.130	0.010
Final Set	8	1	3s	0.47	0.42	-0.01		
		2	4p	0.23	0.97	1.06		
		3	3p	0.93	-0.67	-0.31		
		4	2p	2.86	0.06	0.10		
		5	1s	8.33	-0.03	-0.02	0.010	0.0002

TABLE XV. The determination of the initial set of Slater parameters for expansion sets 5, 6, and 7.

m	nl	$x_{\max}$	Set 5	Set 6	Set 7		n'l'	$a_m$
			$a_m$	$a_m$	$p_m$ exact	$p_m$ rounded		
1	3d	2.14	0.29	1.40	0.61	1	3s	0.47
2	4s	8.86	0.20	0.11	1.76	2	4p	0.23
3	3s	2.14	0.91	0.47	1.95	2	3p	0.93
4	2s	0.70	2.60	1.43	1.82	2	2p	2.86
5	1s	0.12	7.39	8.33	0.89	1	1s	8.33

TABLE XVI. Accuracy of the PF wave functions for the eight final PF expansions given in Tables XIII and XIV.

Expansion Set No.	Standard Deviation of Integrals	Percentage Standard Deviation of Wave Function	Percentage Errors of $\langle r^n \rangle$						
			n = -2	-1	0	1	2	4	6
1	0.069	69.1	74.6	20.4	-4.4	-16.7	-31.2	-59.2	-78.3
2	0.052	35.2	-53.1	-2.9	0.9	5.8	8.1	5.1	-4.1
3	0.041	32.2	-53.4	12.6	1.2	-5.9	-8.2	-1.2	18.1
4	0.030	84.7	-76.6	-13.7	1.6	11.4	25.8	140.3	574.1
5	0.032	46.4	-80.8	-17.7	2.4	14.7	22.2	22.7	7.7
6	0.030	50.5	-17.0	2.6	2.5	18.3	52.3	208.9	574.7
7	0.010	13.1	-24.8	3.6	-1.5	-6.0	-10.5	-19.1	-27.5
8	0.0002	8.2	-48.1	-3.2	-0.0	0.3	-0.8	-6.0	-14.0

**BLANK PAGE**

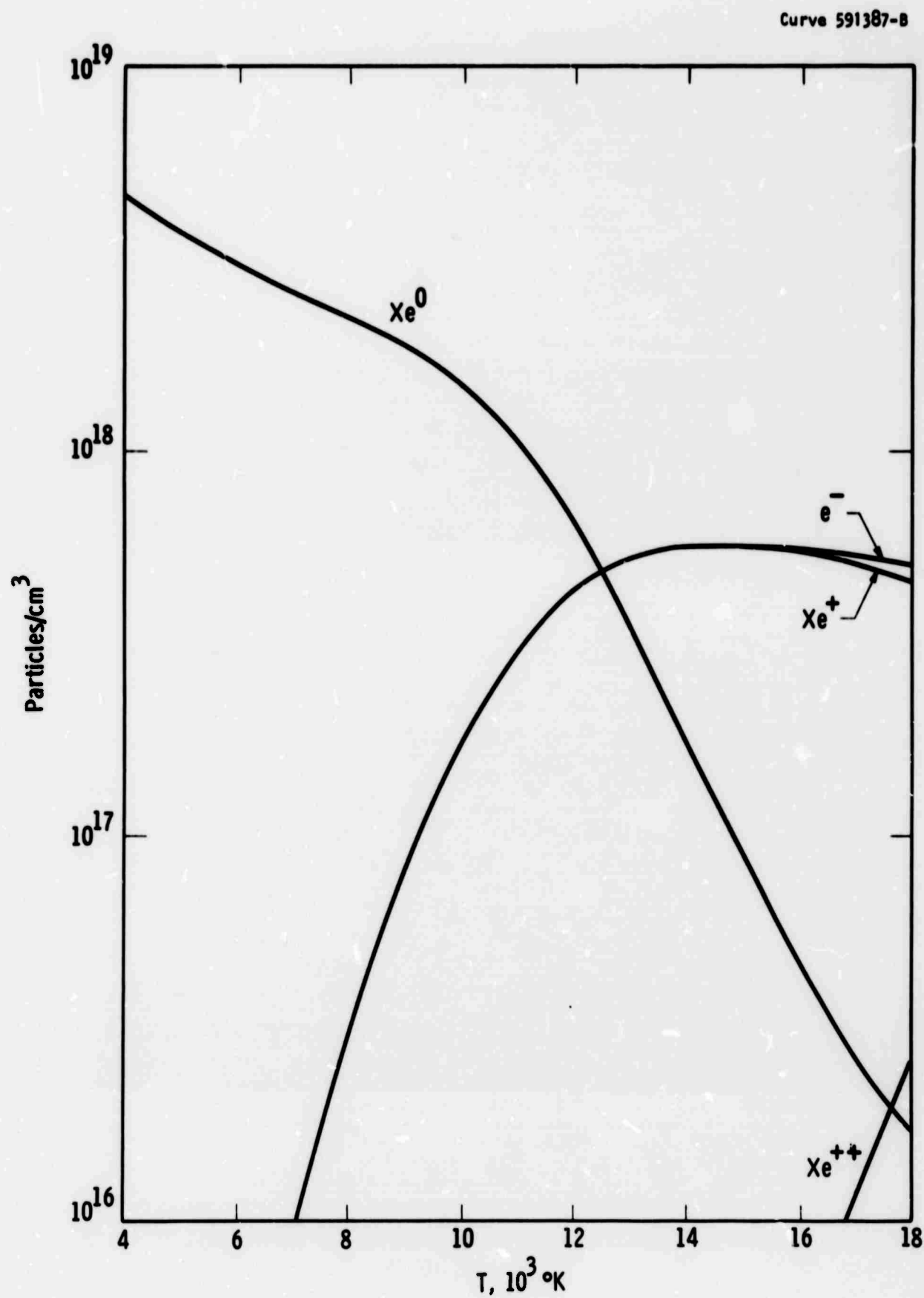


Fig. 1—Chemical composition of a 2.5 atmosphere xenon arc discharge as a function of temperature

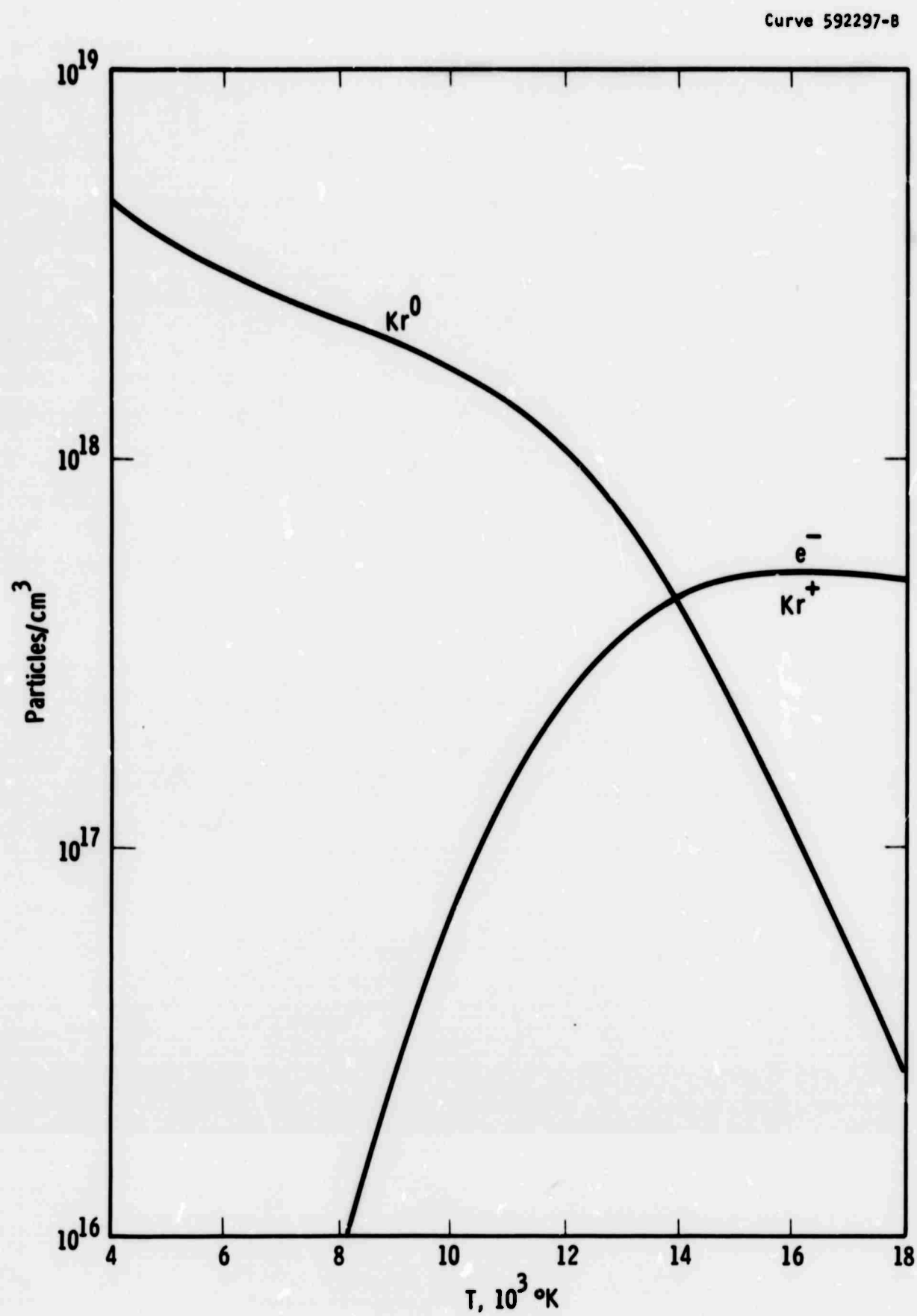


Fig. 2—Chemical composition of a 2.5 atmosphere krypton arc discharge as a function of temperature

Curve 591388-B

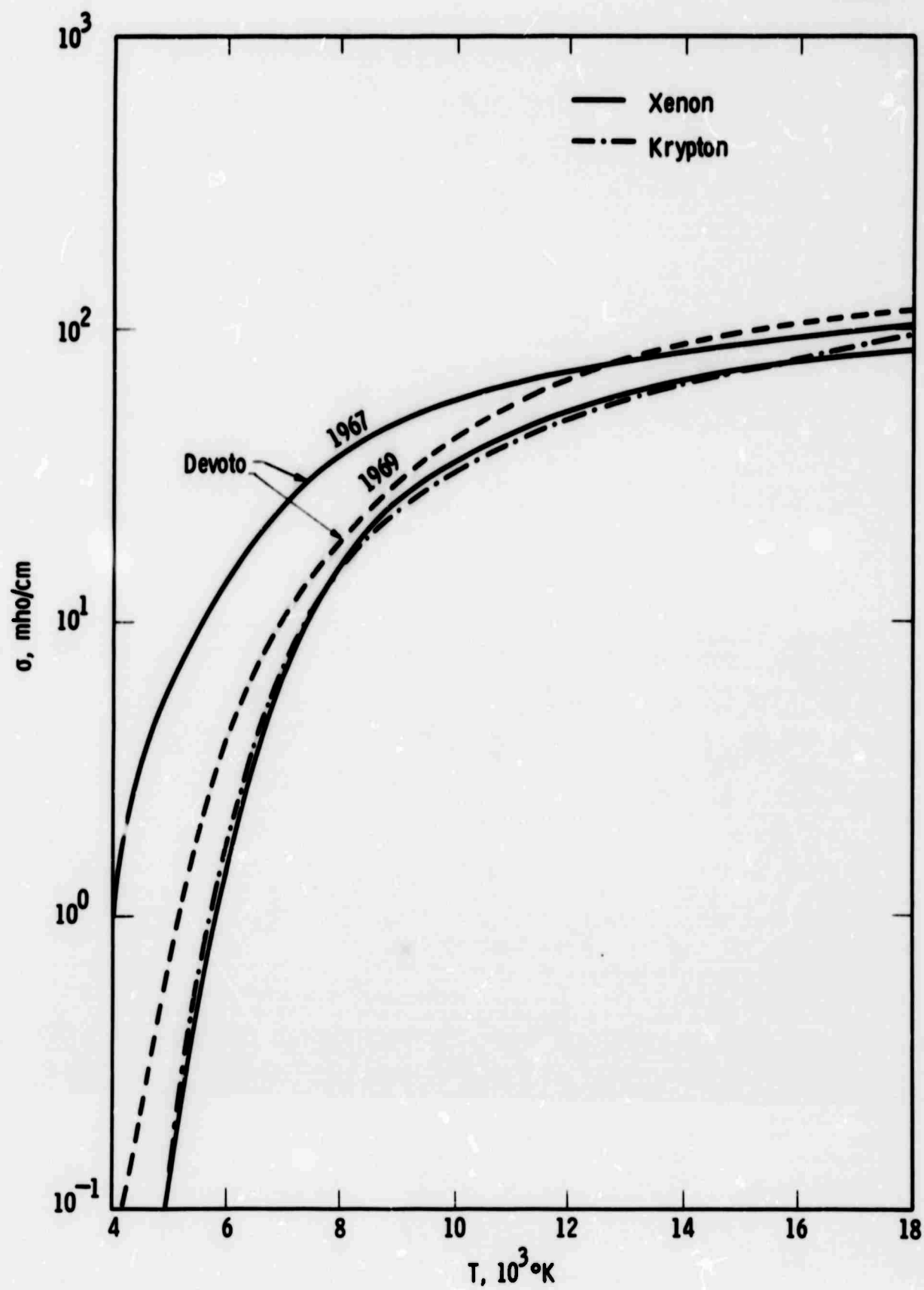


Fig. 3—Electrical conductivity of a 2.5 atmosphere arc discharge.  
Devoto's values are for xenon



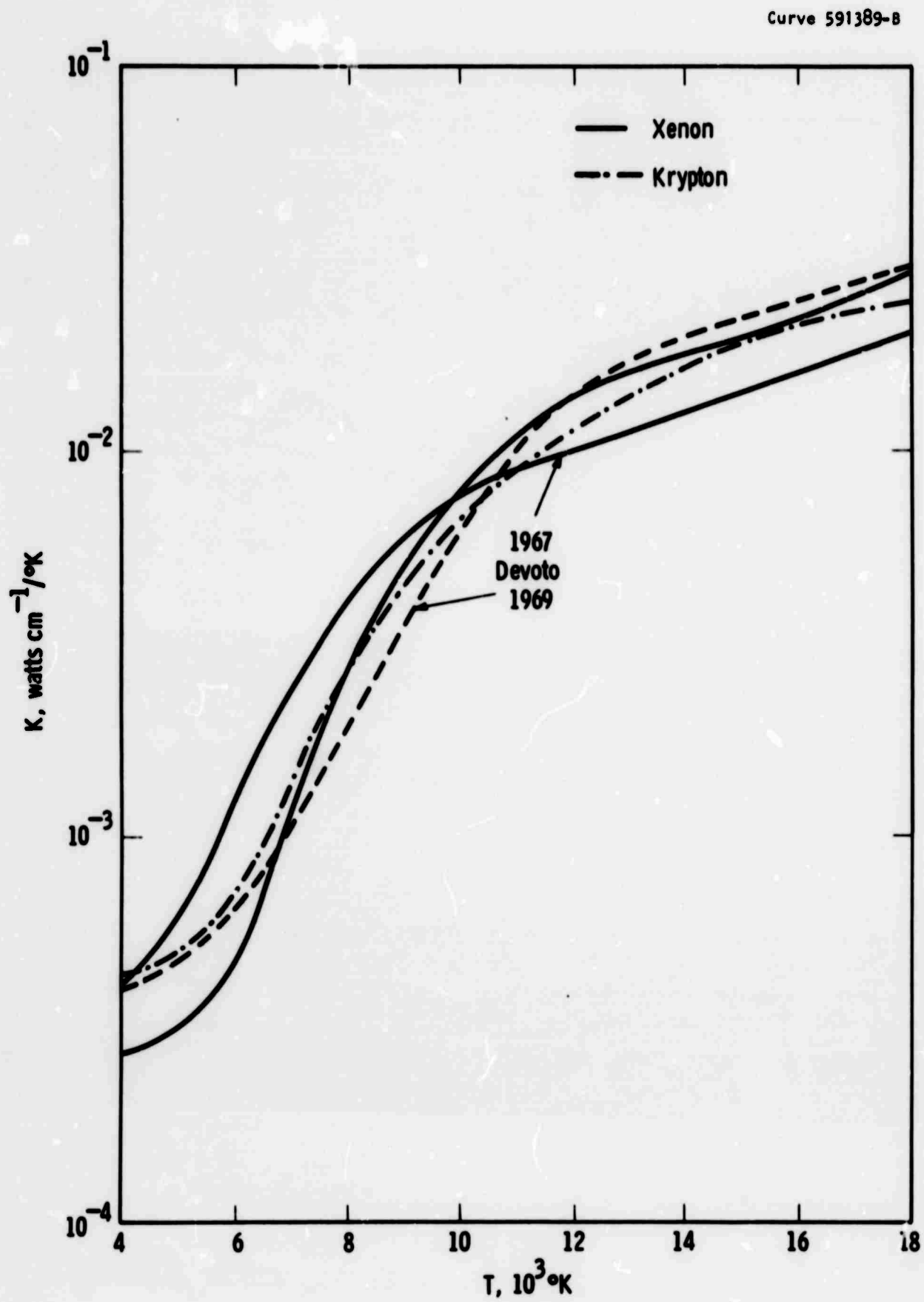


Fig. 4—Thermal conductivity of a 2.5 atmosphere arc discharge.  
Devoto's values are for xenon

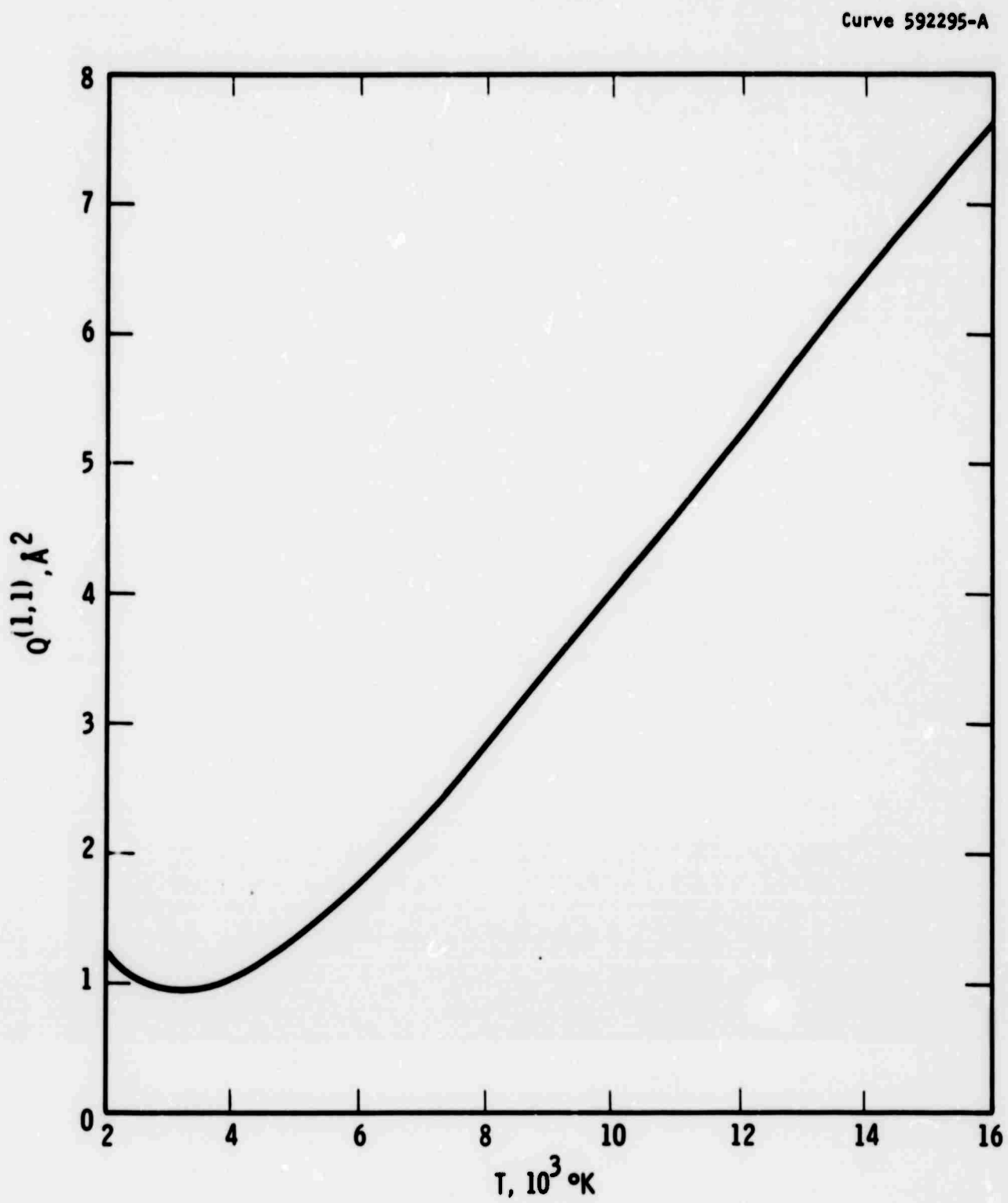


Fig. 5—Average electron-neutral momentum-transfer cross sections for krypton

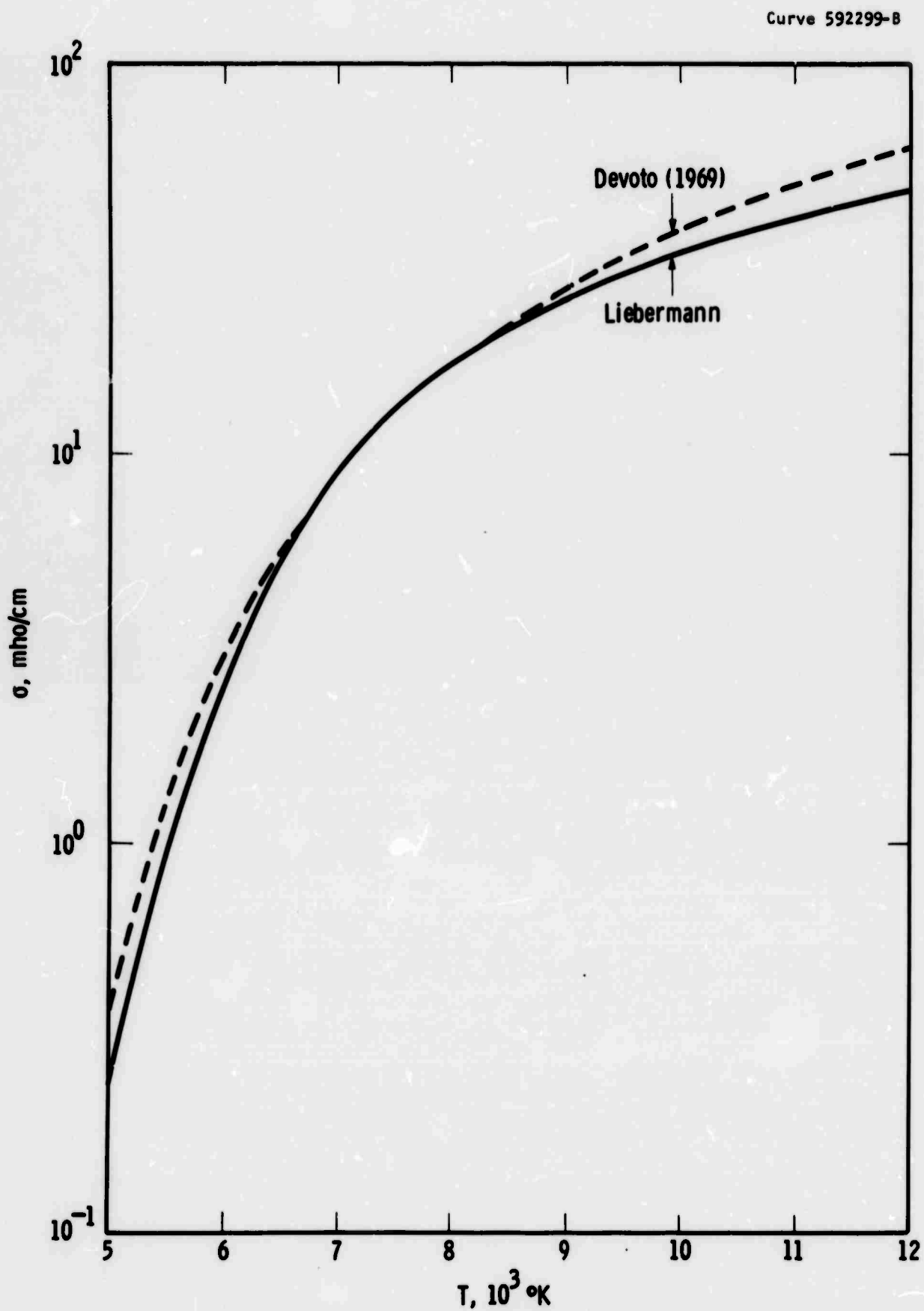


Fig. 6—Electrical conductivity of a 1.0 atmospheric krypton arc discharge

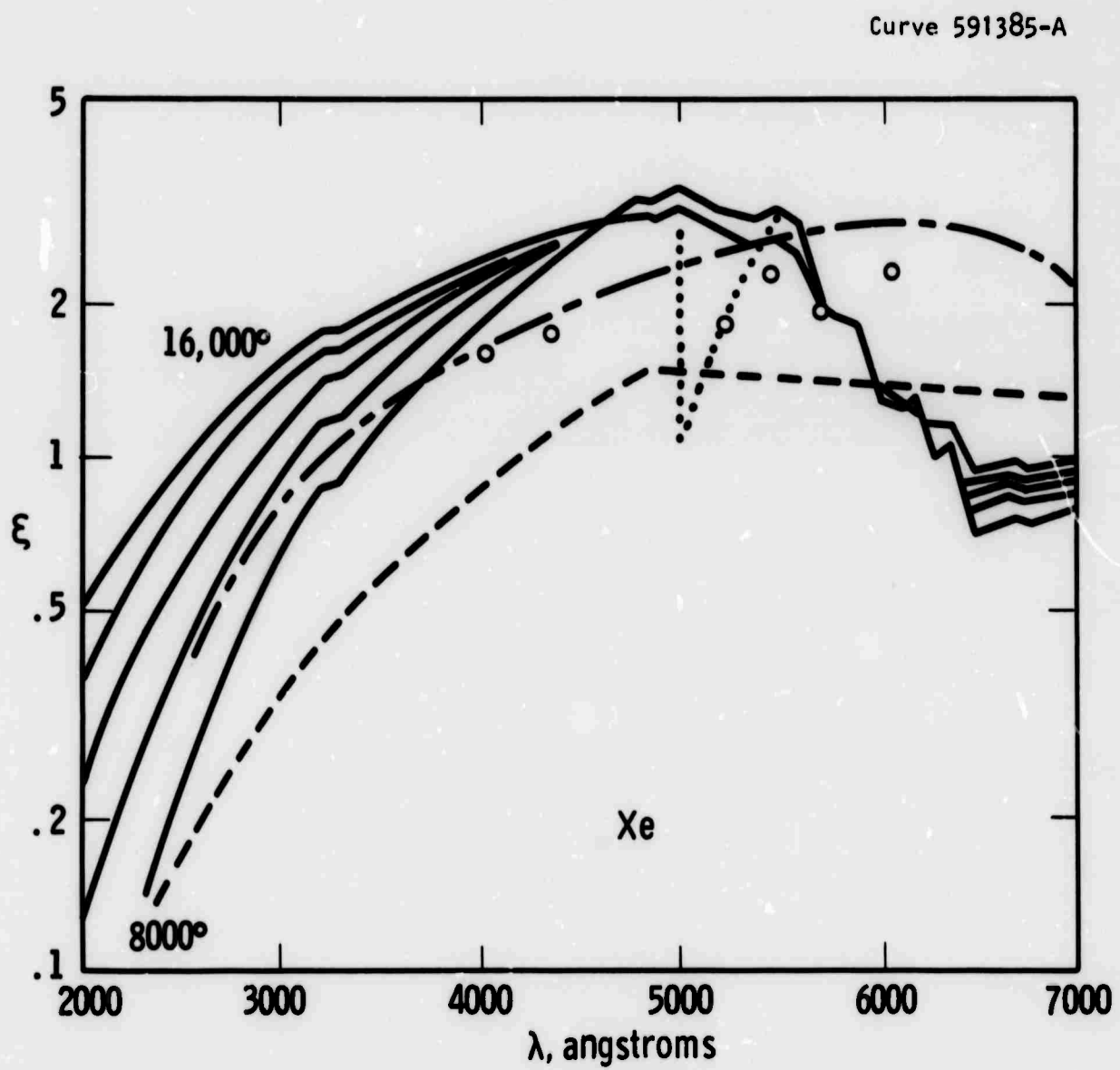


Fig. 7  $-\xi$ -Factor for xenon — Schlüter; - - -Biberman et al;  
 - · - · - Yankov; · · · · · Liebermann; o measurements by Berge et al

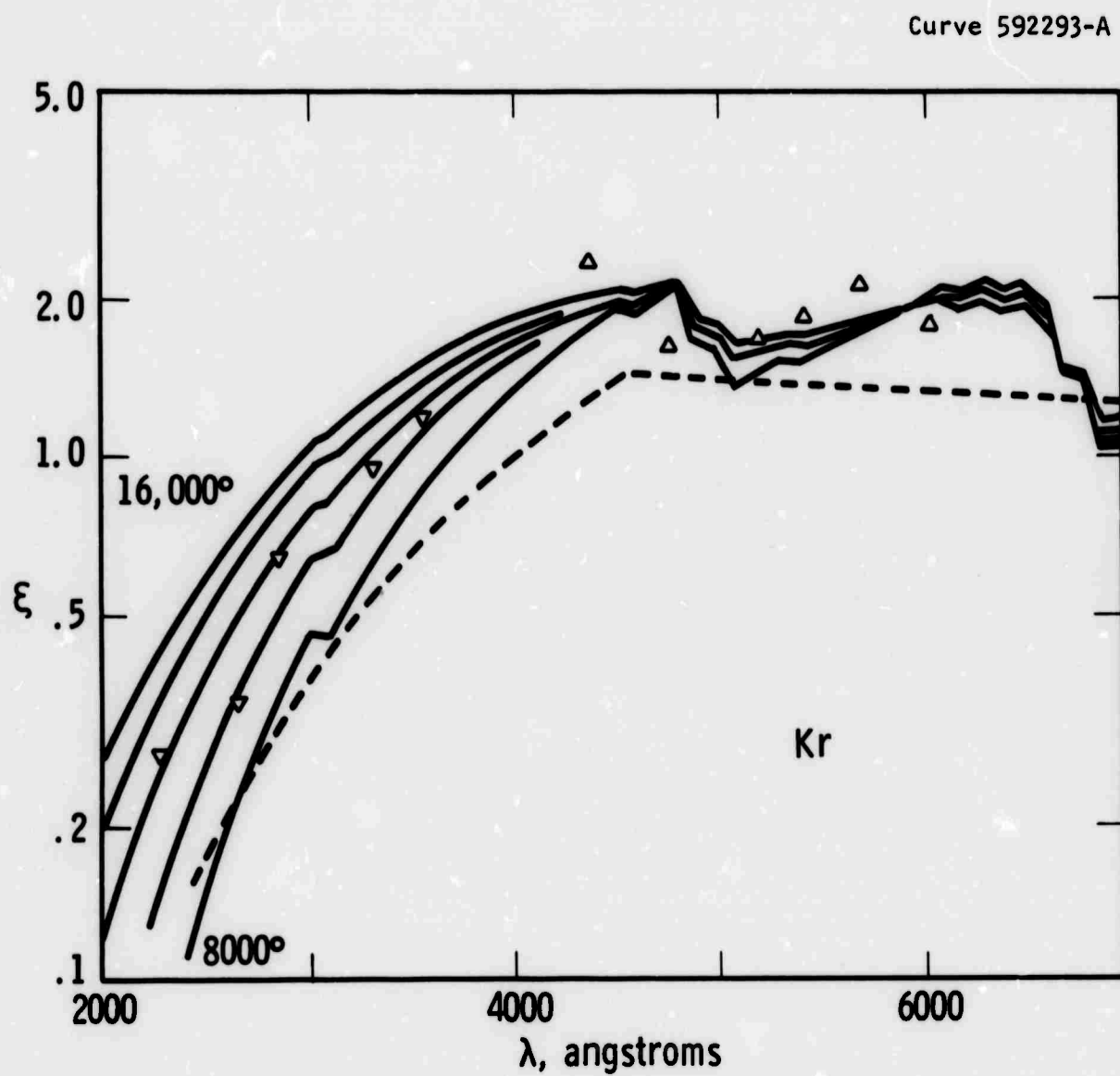


Fig. 8— $\xi$ -factor for krypton — Schlüter; - - Biberman et al;  
 $\Delta$  measurements by Carls

Curve 592300-8

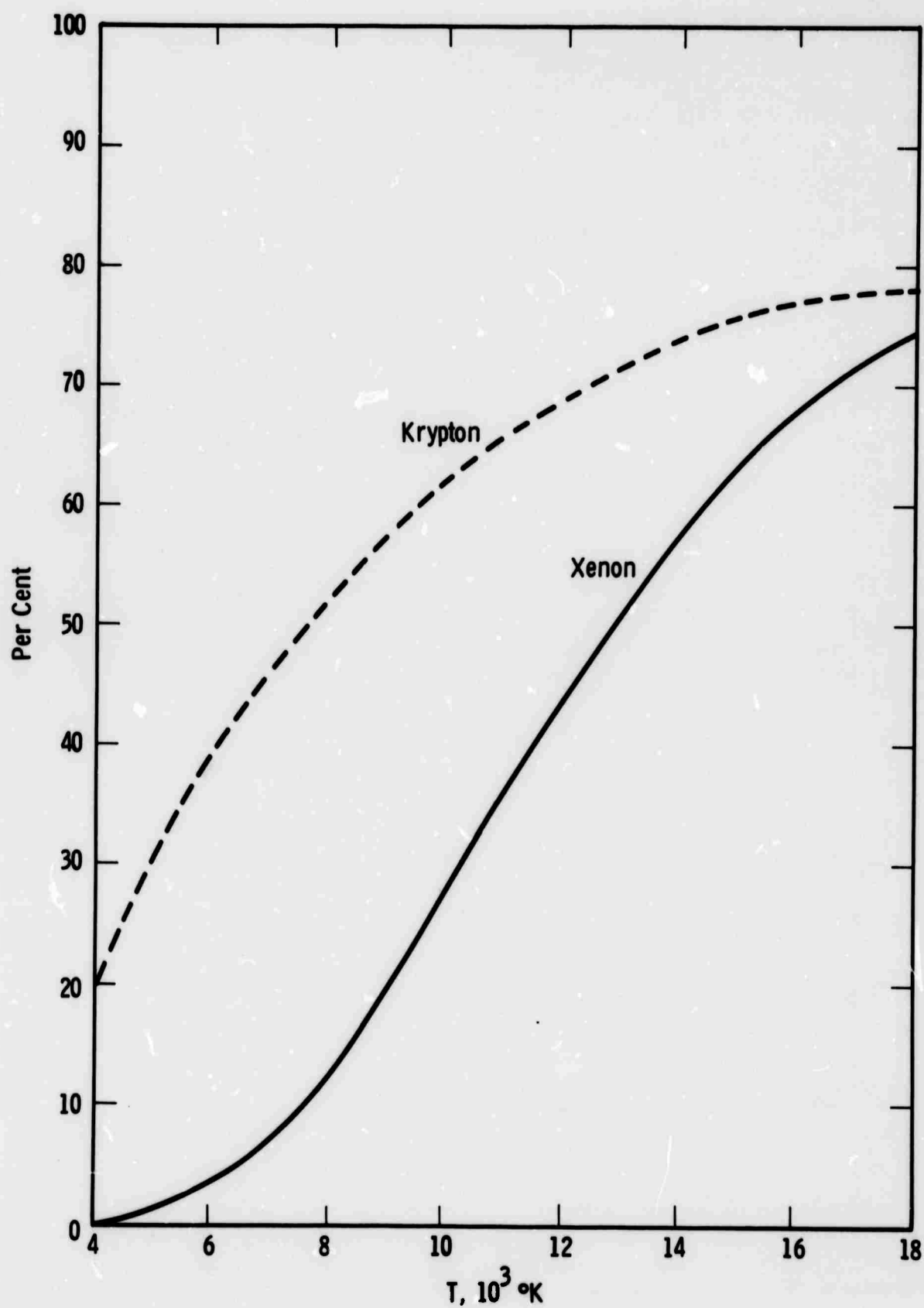


Fig. 9—Percentage of the total radiation from a 2.5 atmospheres arc discharge which is continuum radiation. The wave length interval is from 2000 to 20,000 angstroms

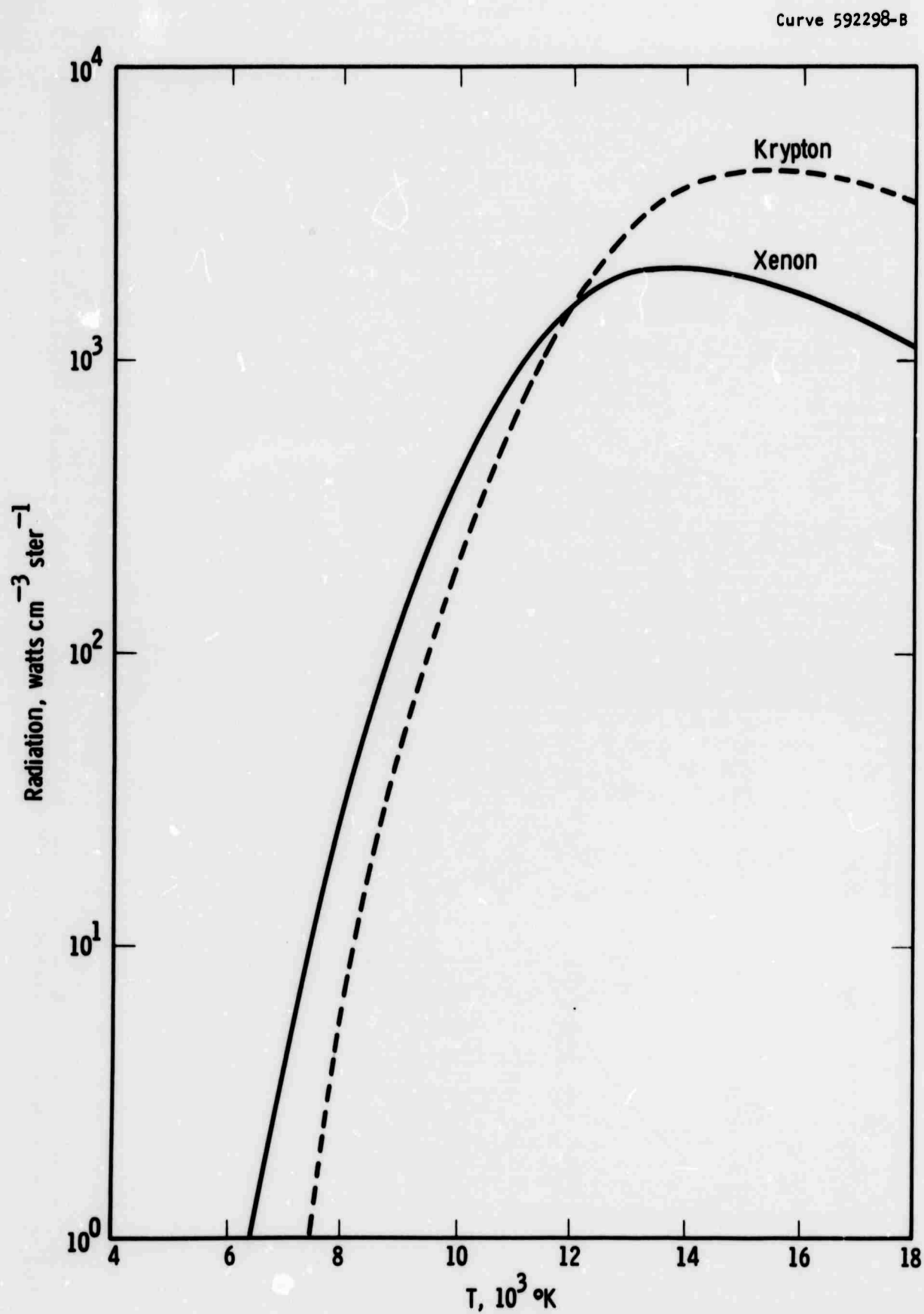


Fig. 10—Total radiation from a 2.5 atmospheres arc discharge in the wave length interval from 2000 to 20,000 angstroms

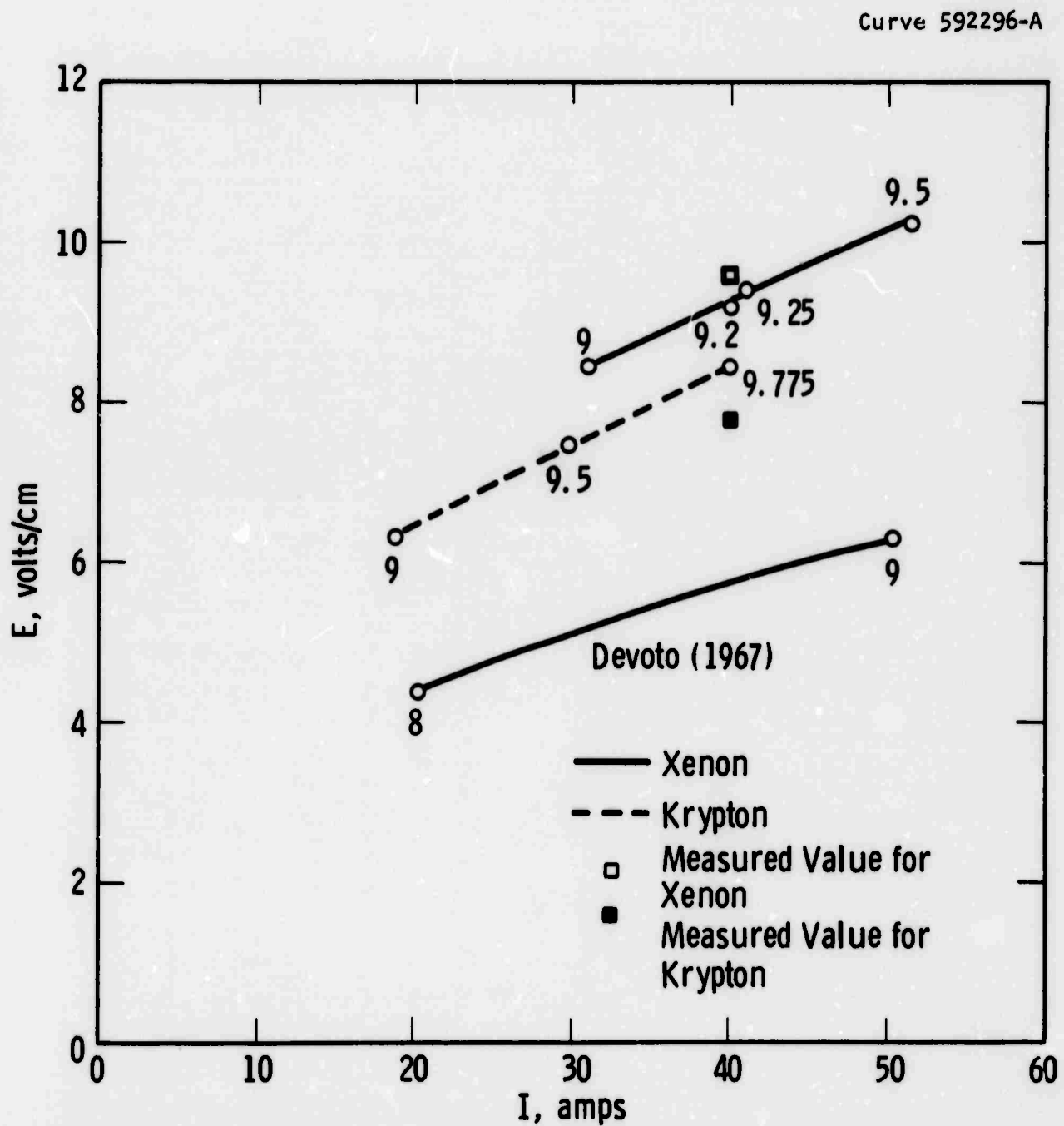


Fig. 11—The electrical characteristics of a 2.5 atmospheres arc discharge. The central core temperatures are given in  $10^3$  °K. The points on the curves indicate the temperatures at which the characteristics were calculated



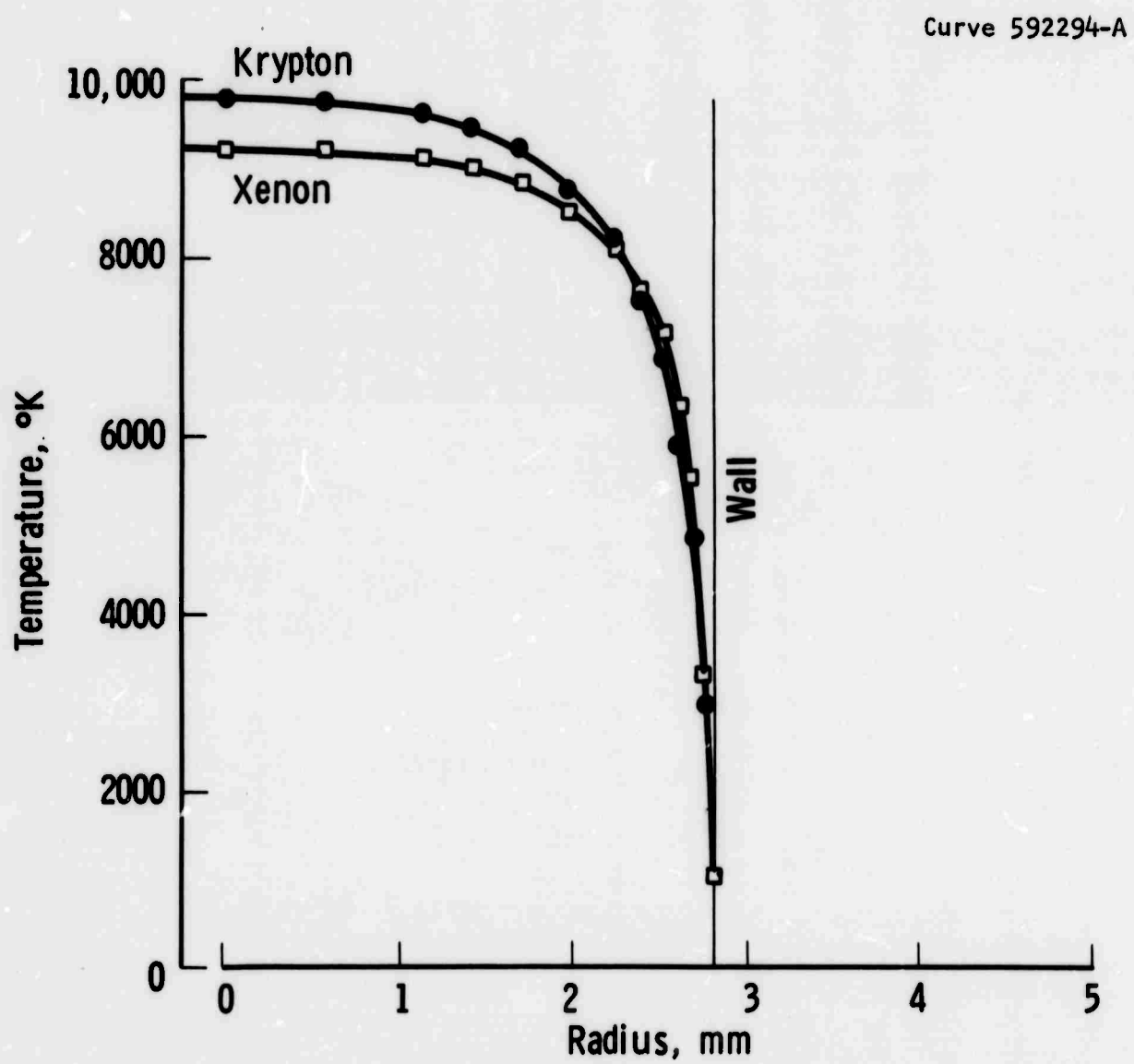


Fig. 12—Calculated temperature profiles of a 40 amp-2.5 atm arc discharge.  
The  $\square$  and  $\bullet$  denote calculated values

Fig. 13—Spectral radiance at the surface of a 40 amp-2.5 atm xenon arc discharge

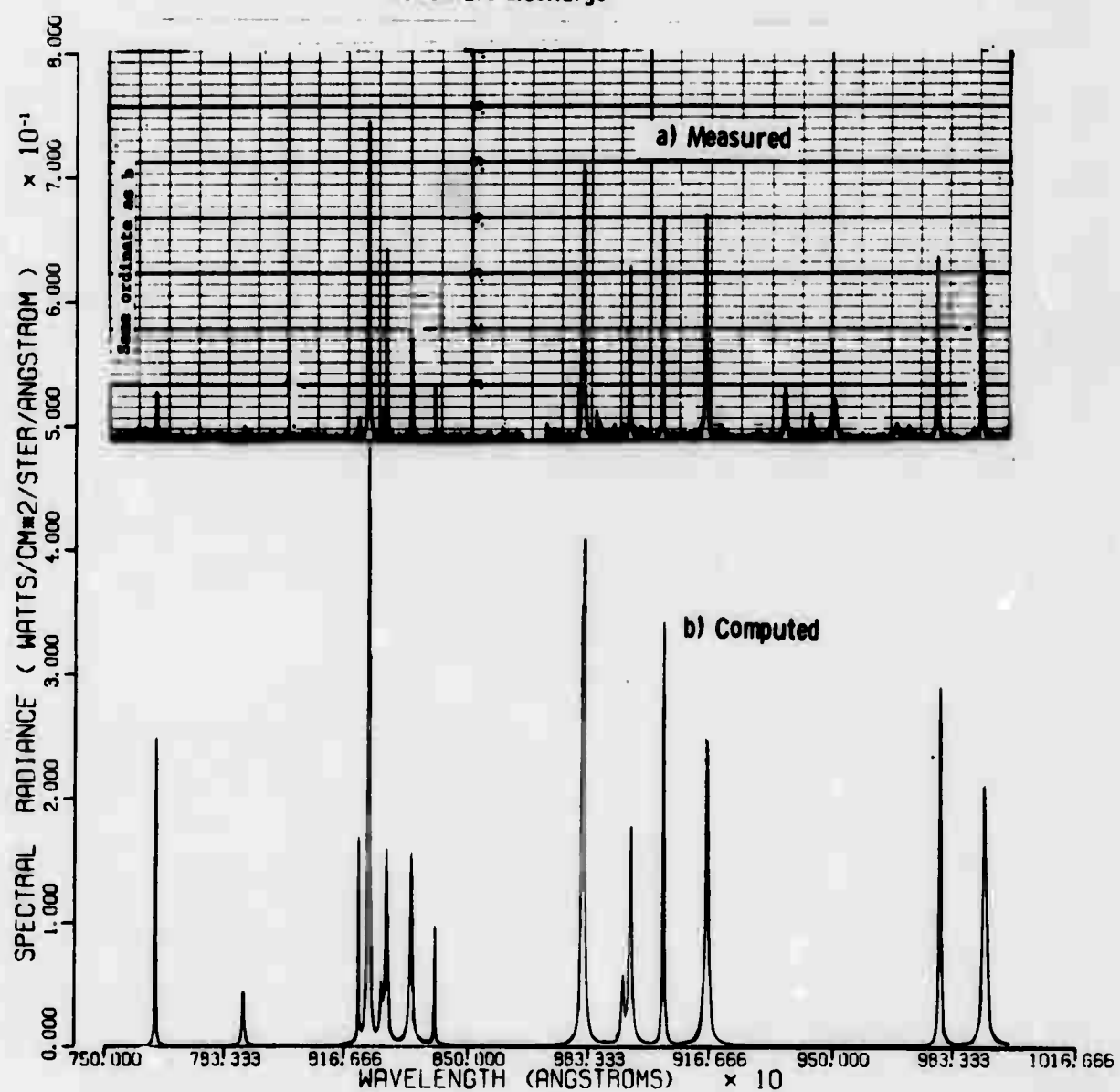


Fig. 14—Spectral radiance of the 8232 Å line at the surface of a 40 amp-2.5 atm xenon arc discharge

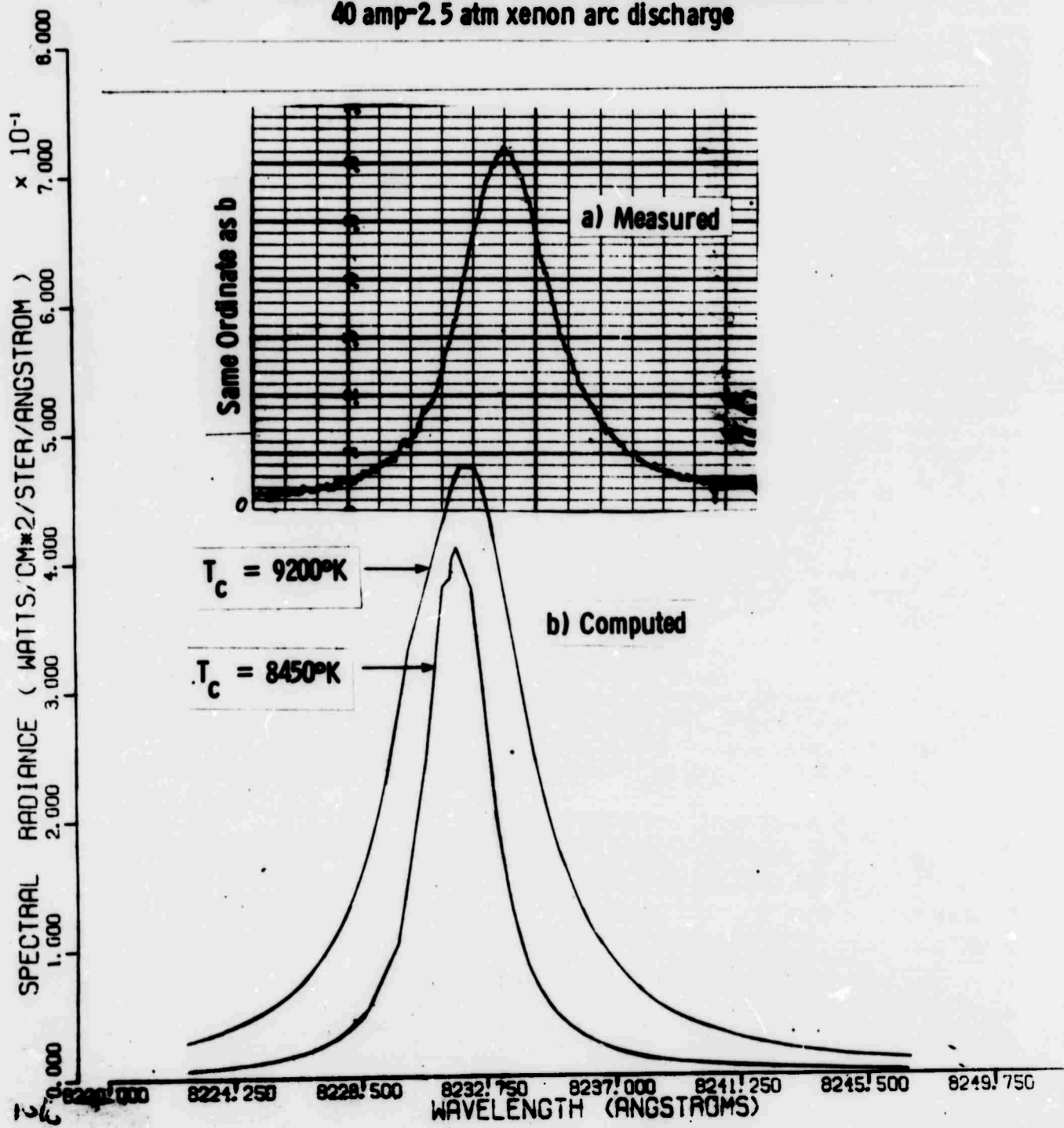


Fig. 15—Spectral absorptivity of an emission line at 9200°K in a  
40 amp-2.5 atm xenon arc discharge

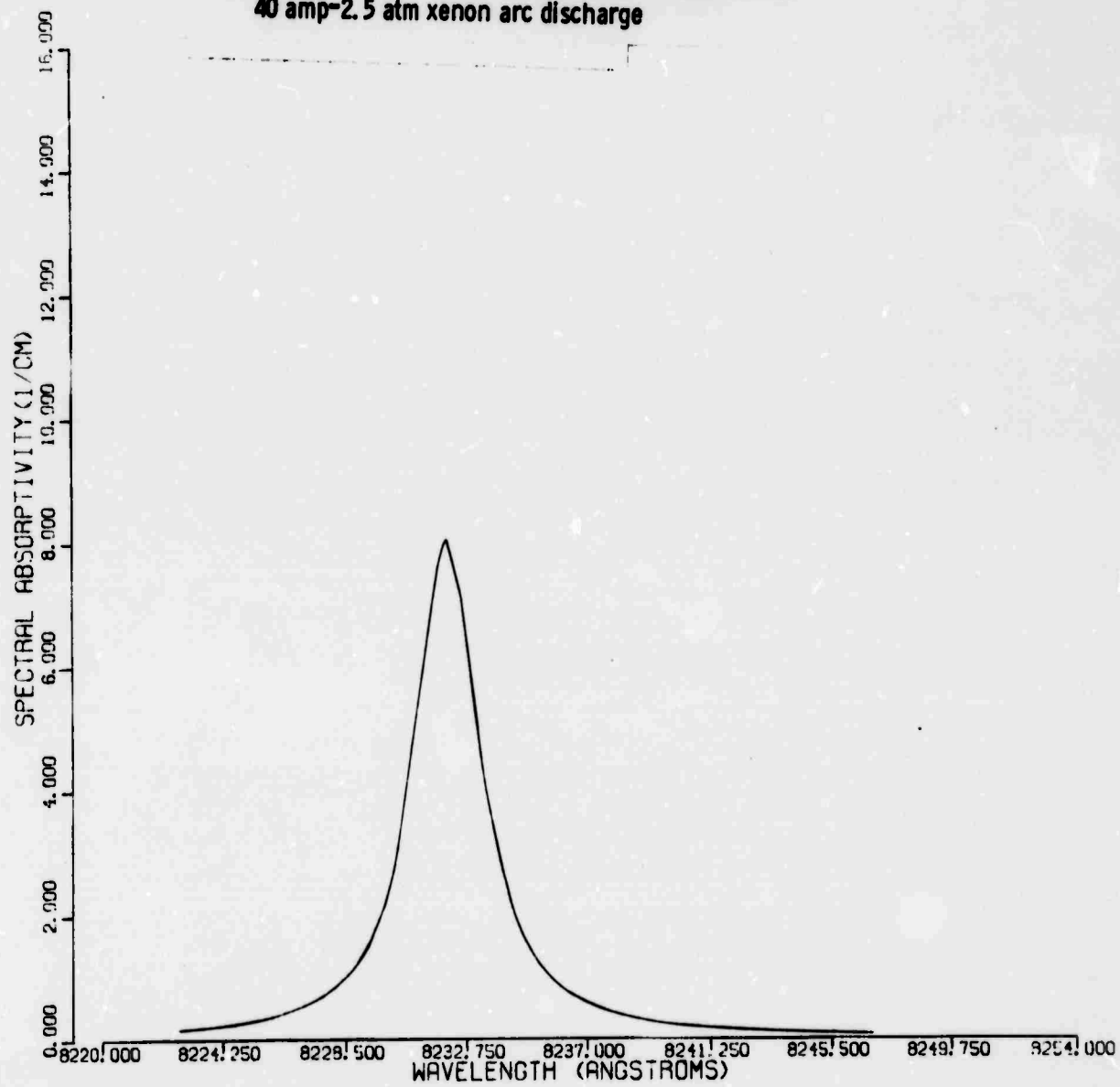
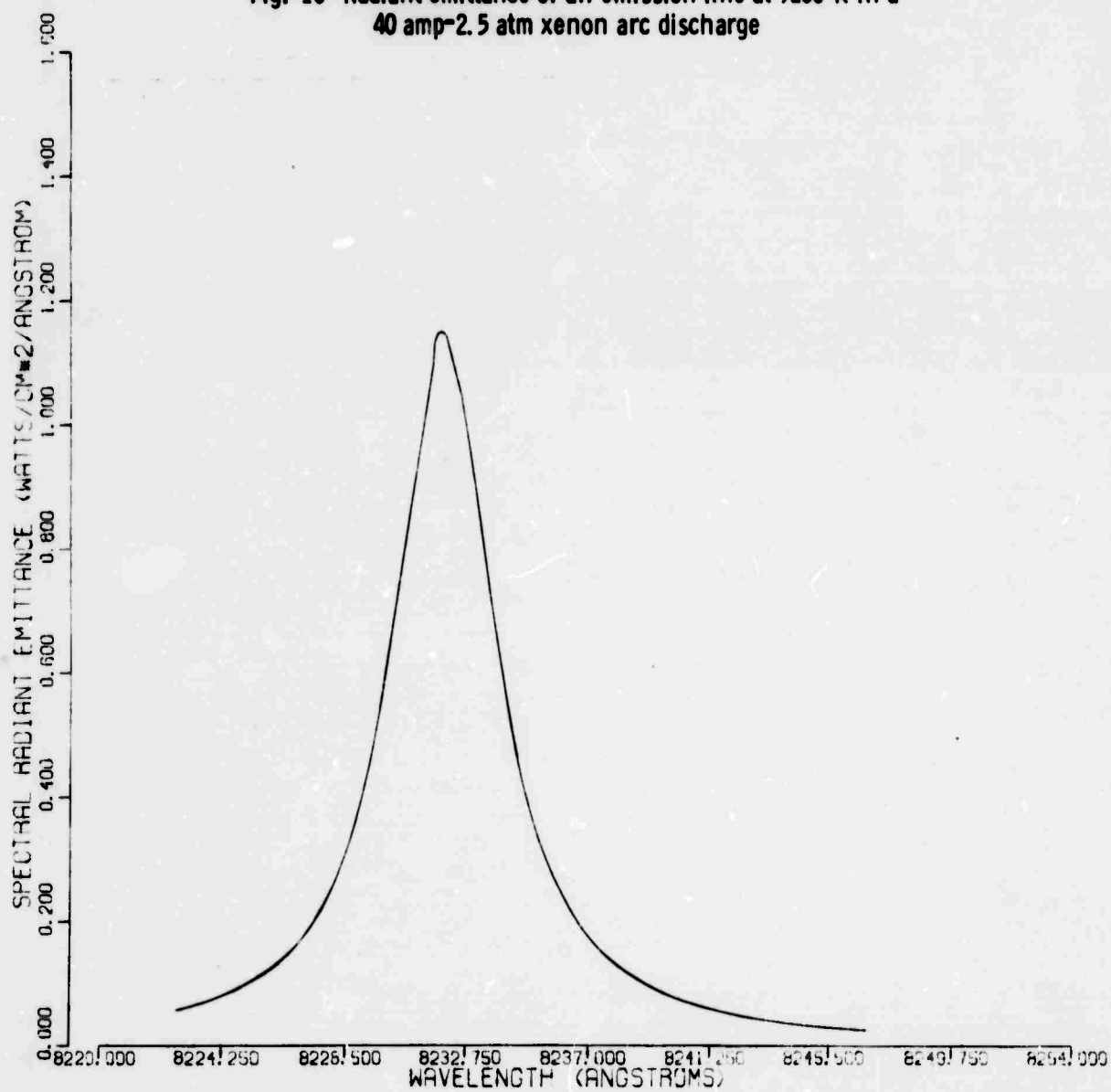


Fig. 16—Radiant emittance of an emission line at 9200°K in a  
40 amp-2.5 atm xenon arc discharge



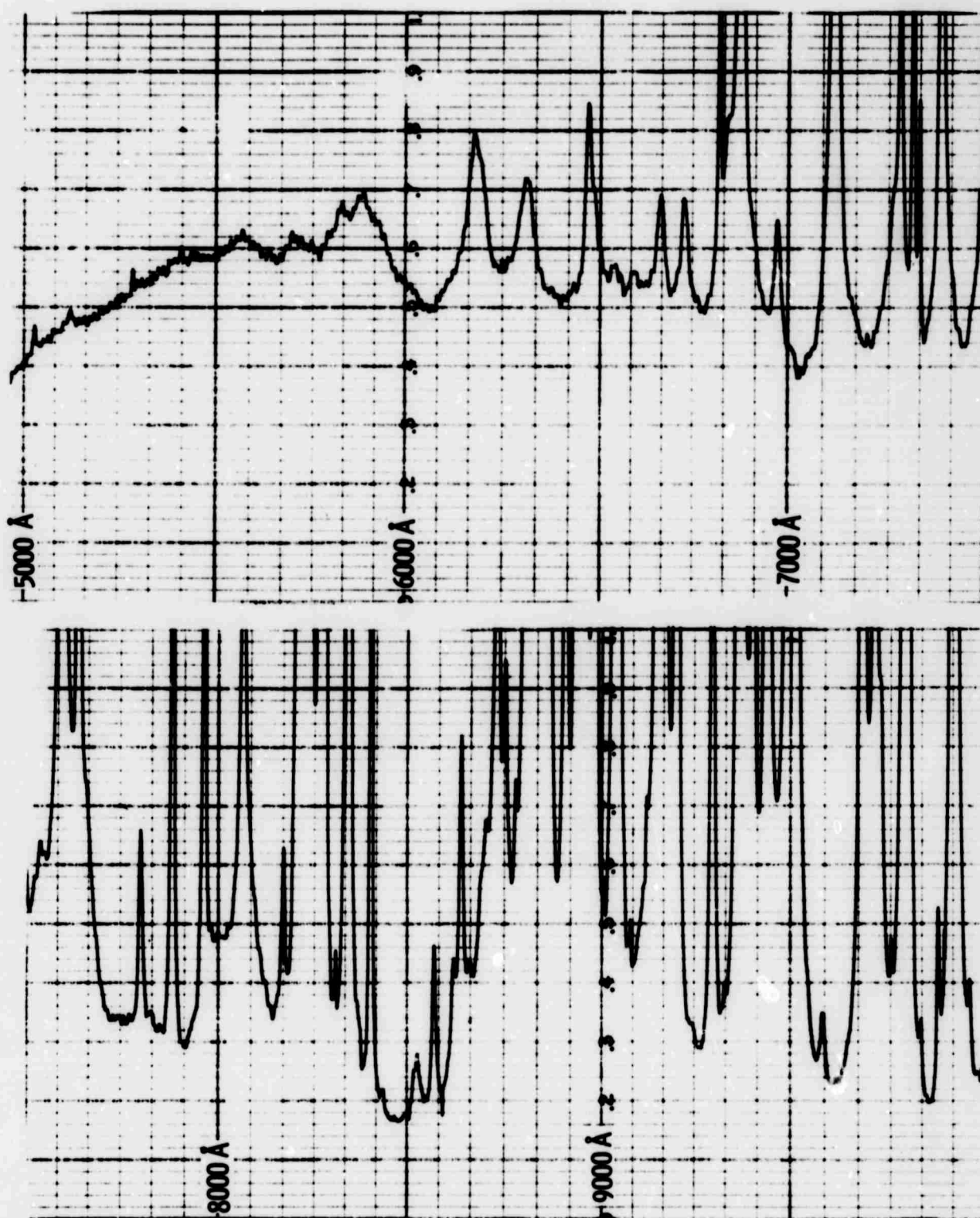


Fig. 17—Measured spectral radiance of a 40 amp-2.5 atm xenon arc discharge.  
Full scale is  $4.96 \times 10^{-3}$  watts/(cm<sup>2</sup> ster Å)

Fig. 18—Spectral radiance at the surface of a 40 amp-2.5 atm xenon arc discharge.  
The absolute values of the continuum radiance are in error (see subsection 2.2.1)

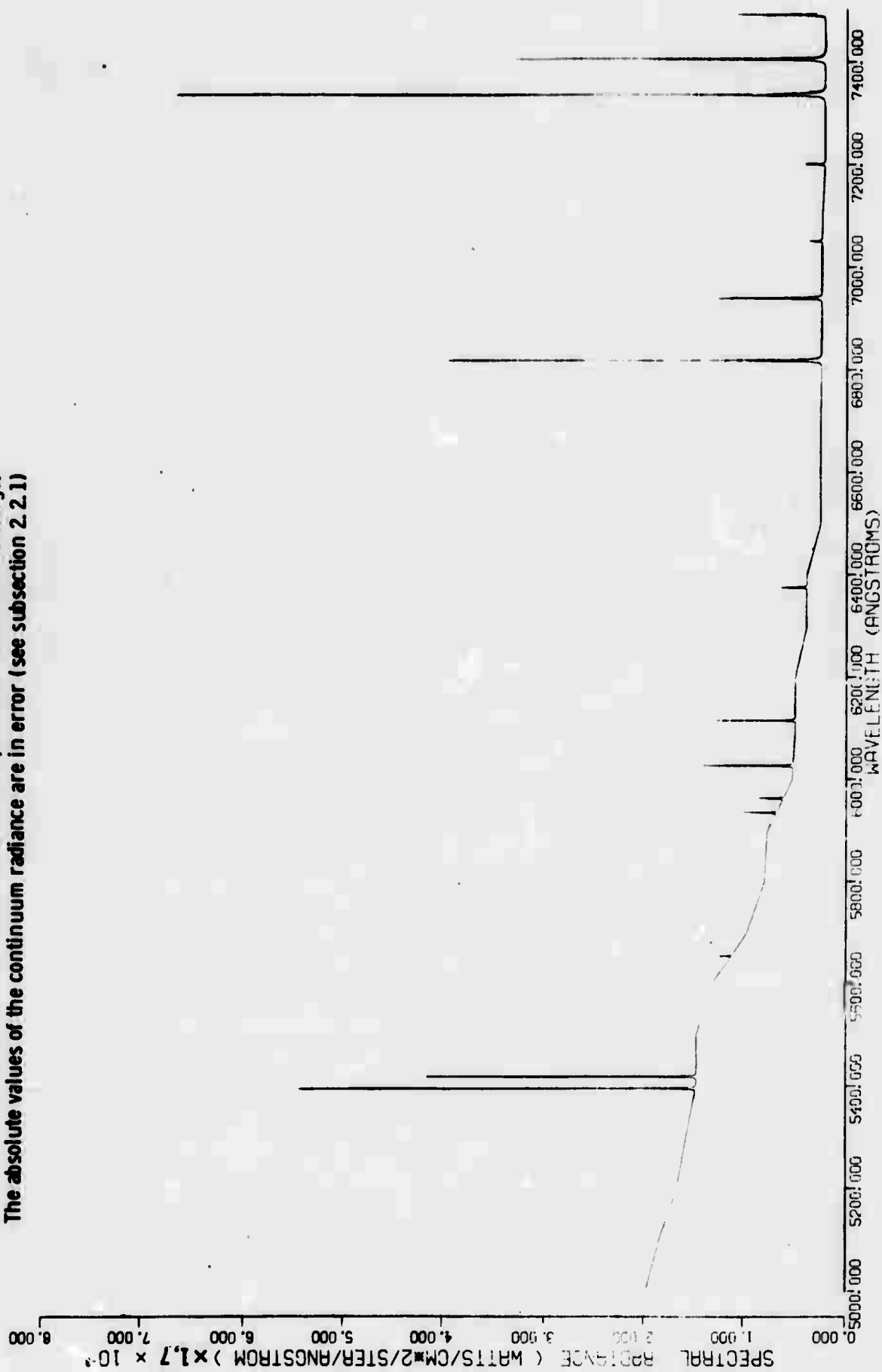


Fig. 19—Spectral radiance at the surface of a 40 amp-2.5 atm xenon arc discharge

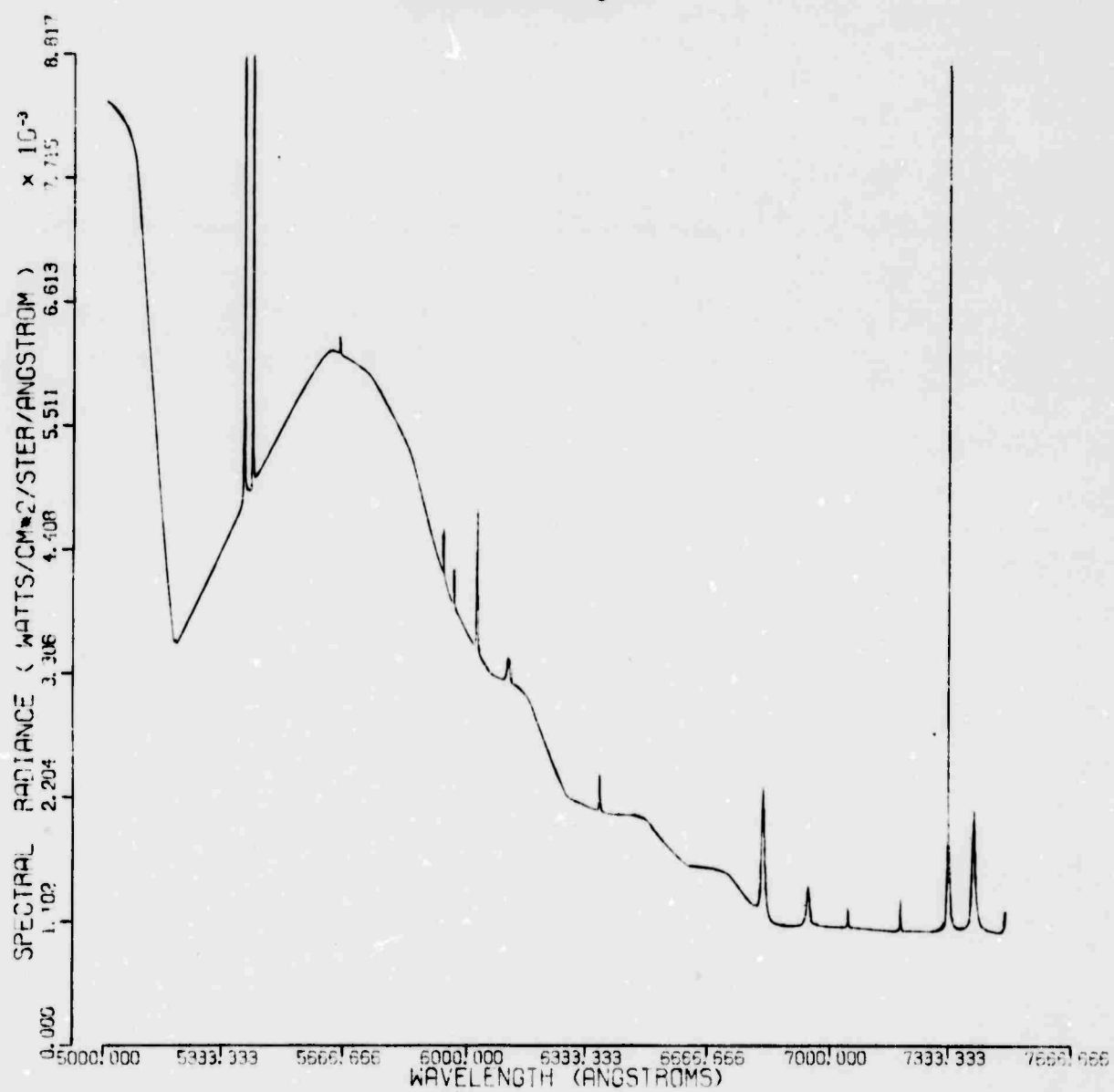




Fig. 20—Spectral radiance at the surface of a 40 amp-2.5 atm krypton arc discharge

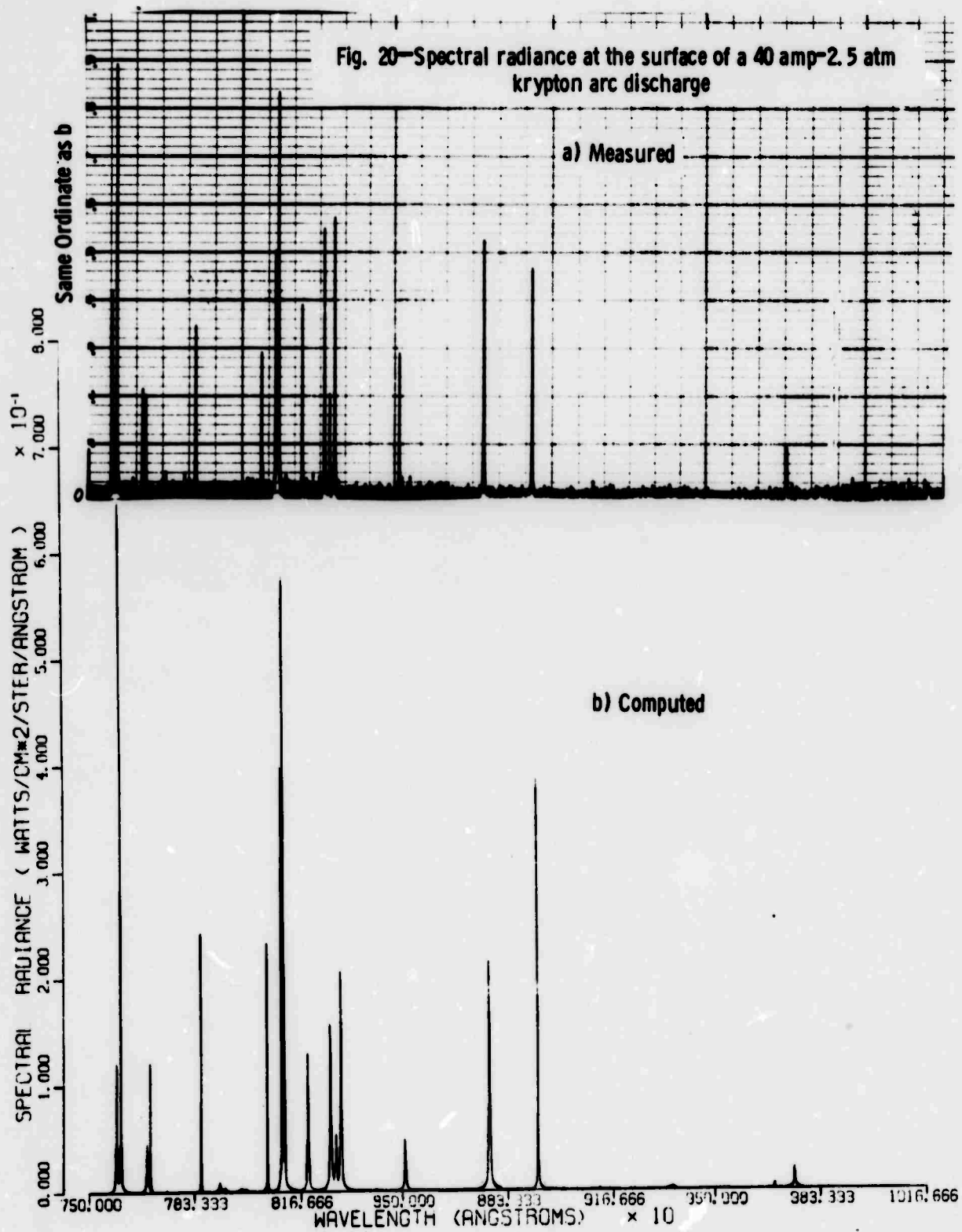
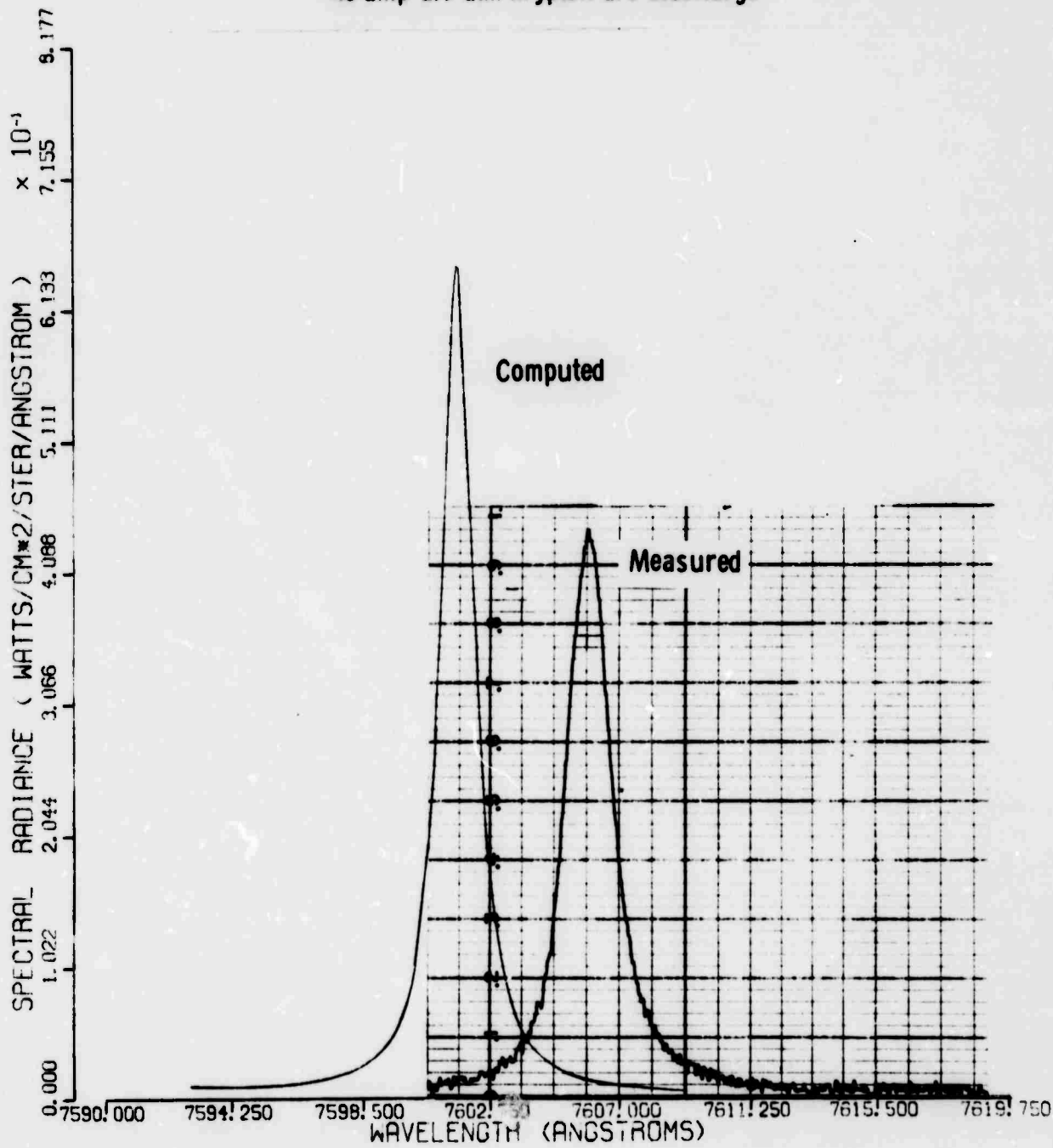


Fig. 21—Spectral radiance of the 7606 Å line at the surface of a 40 amp-2.5 atm krypton arc discharge



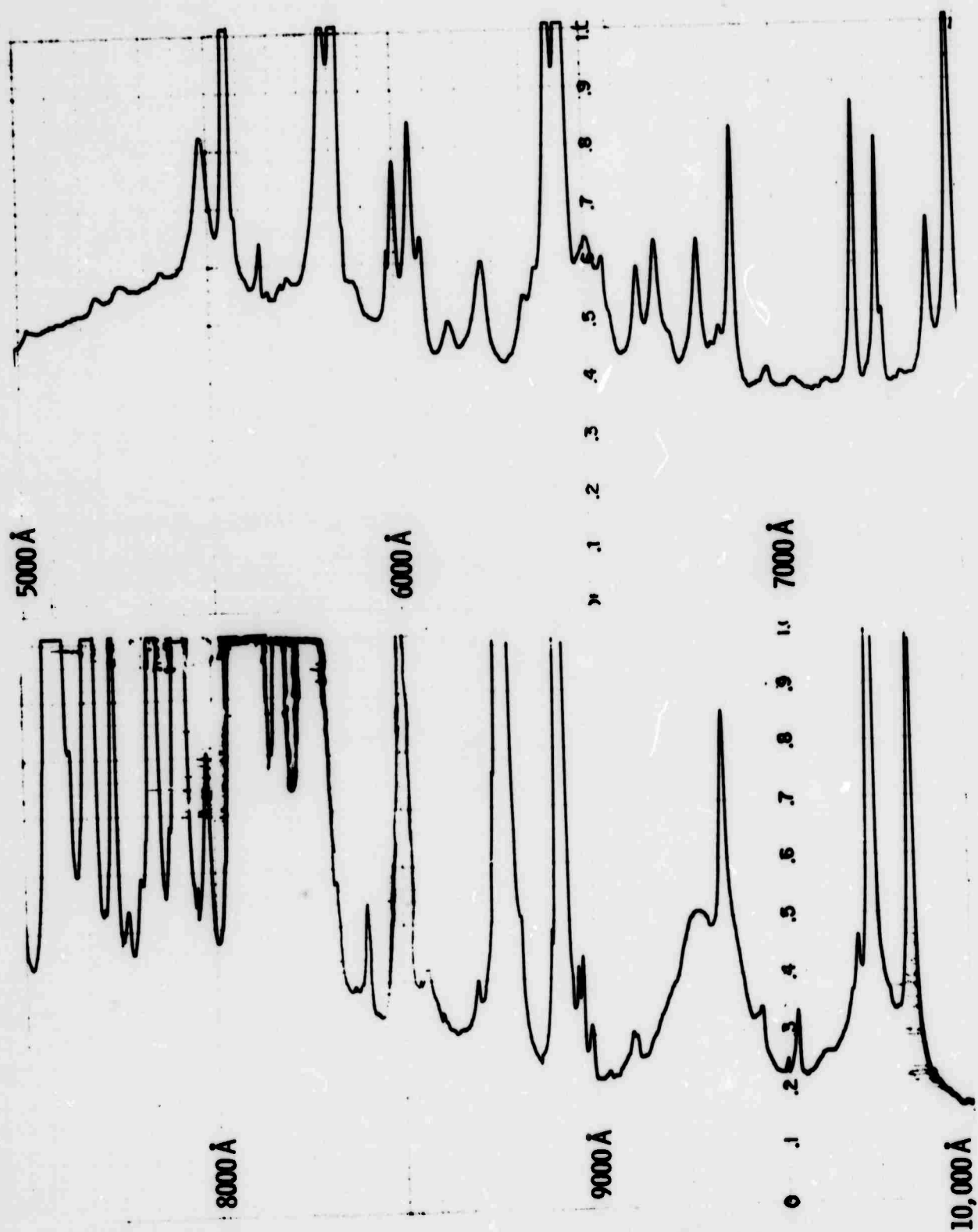
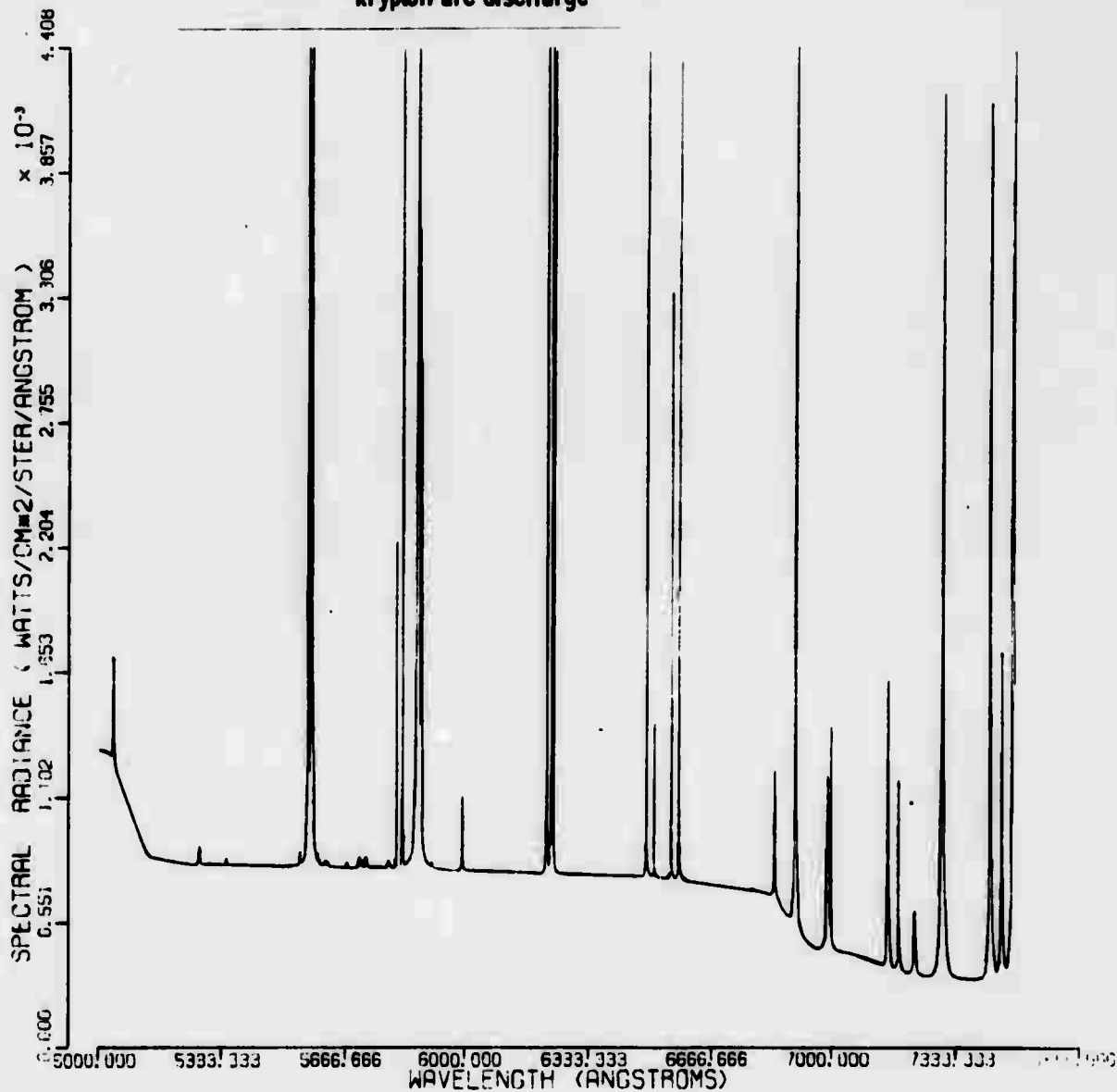


Fig. 22—Measured spectral radiance of a 40 amp-2.5 atm krypton arc discharge. Full scale is  $2.48 \times 10^{-3}$  watts/(cm<sup>2</sup> ster Å)

Fig. 23—Spectral radiance at the surface of a 40 amp-2.5 atm  
krypton arc discharge



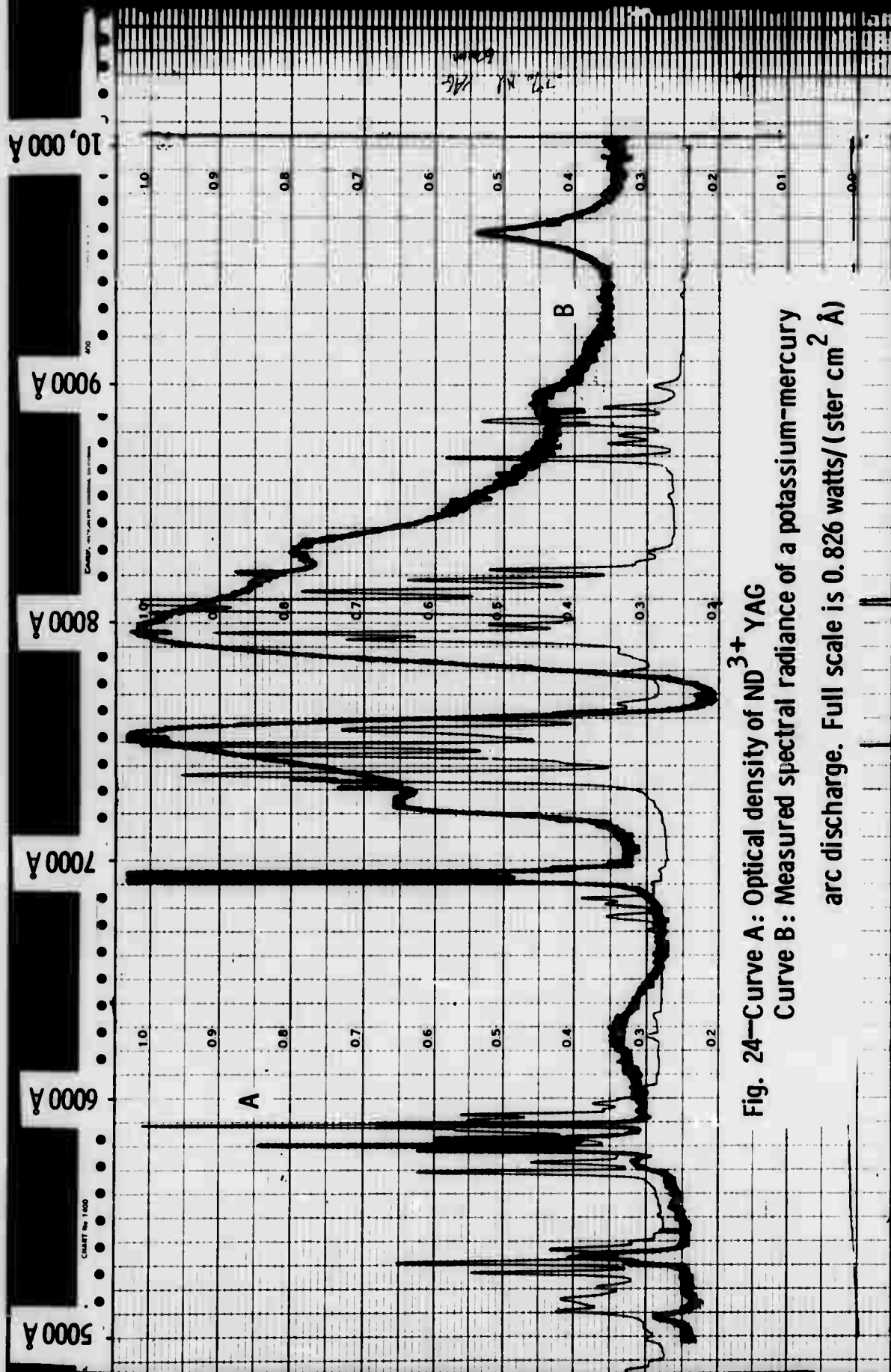


Fig. 24—Curve A: Optical density of  $\text{ND}^{3+}$  YAG  
Curve B: Measured spectral radiance of a potassium-mercury arc discharge. Full scale is  $0.826 \text{ watts/ster cm}^2 \text{ Å}$

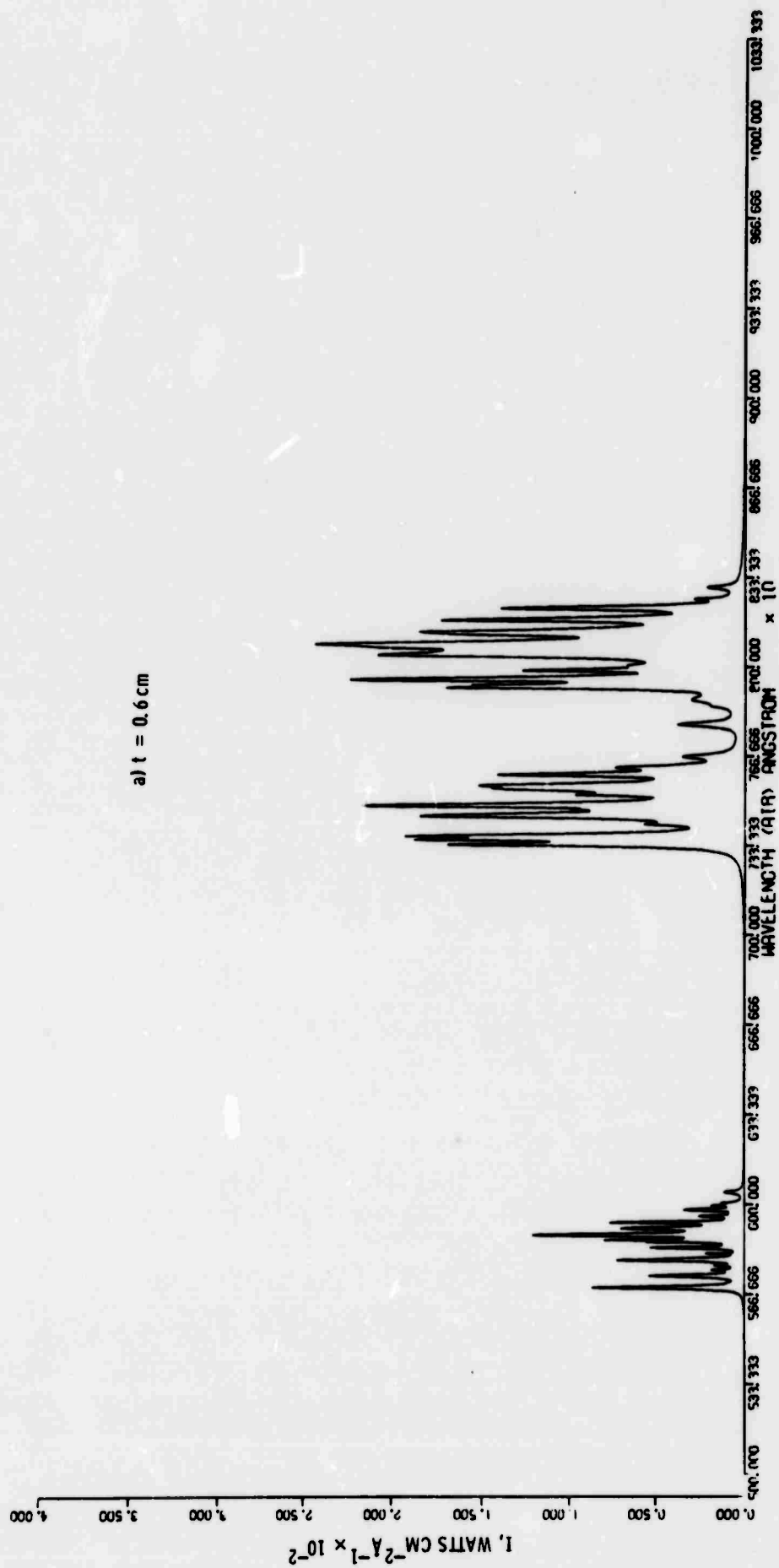
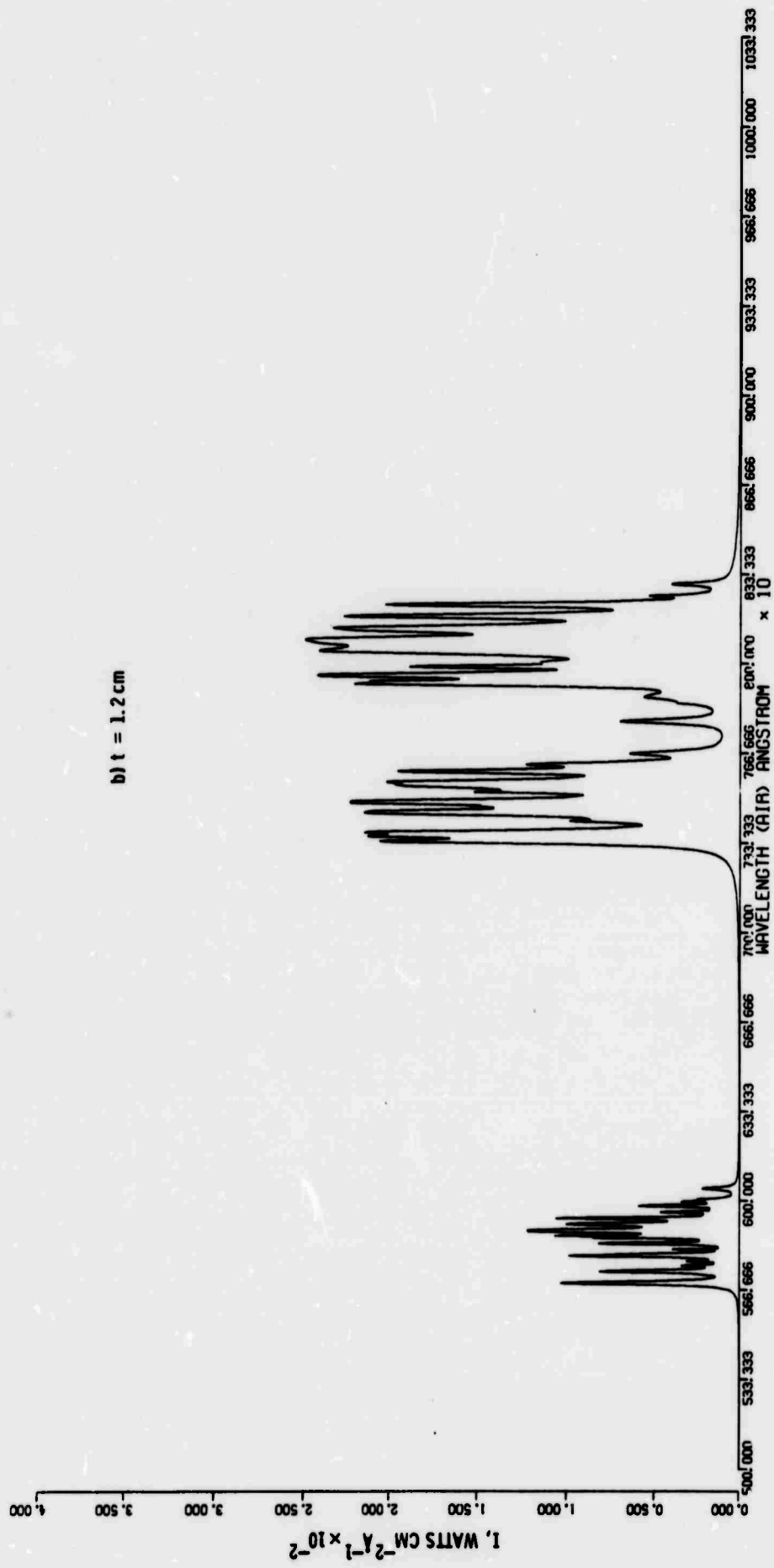
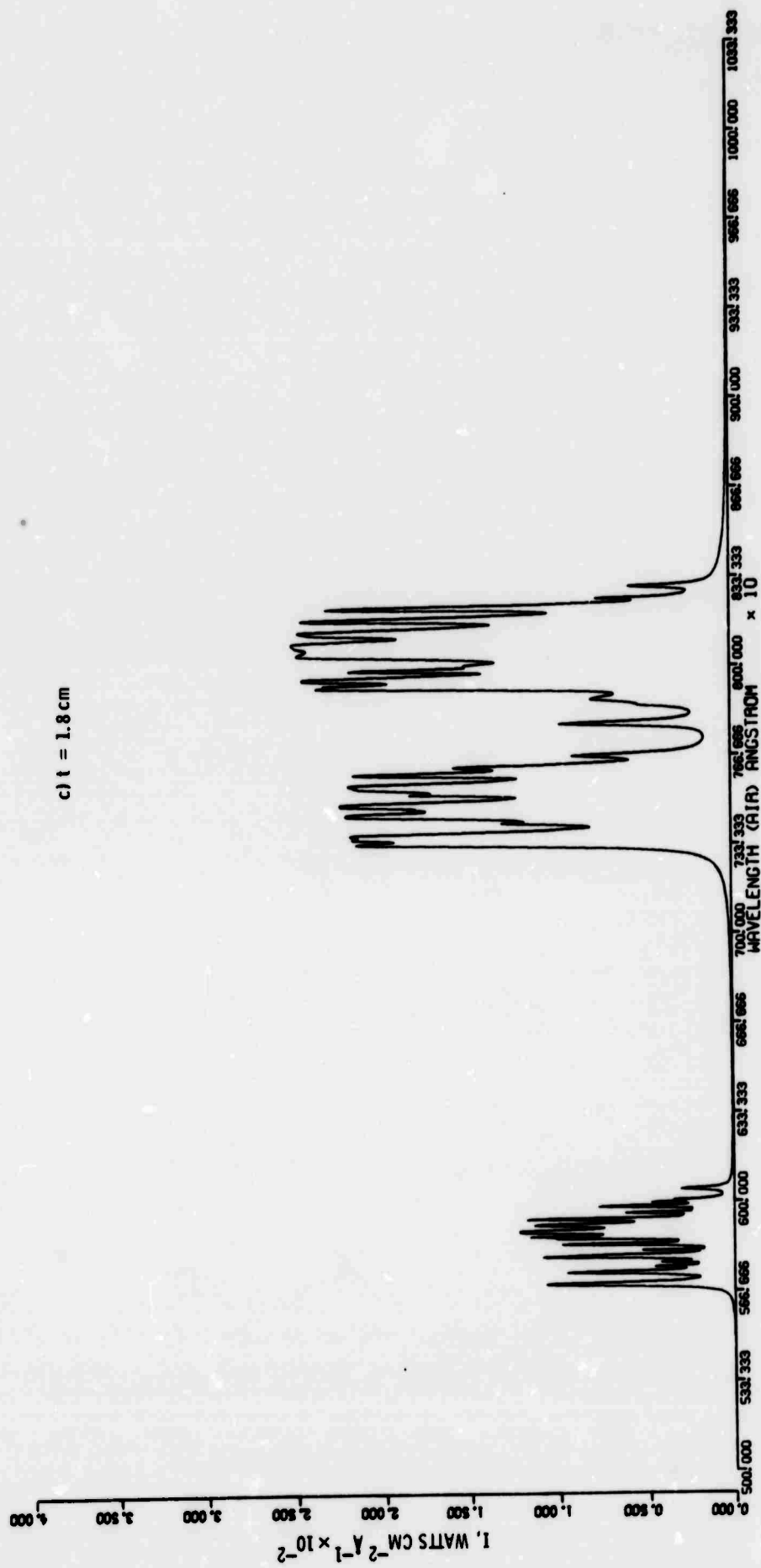
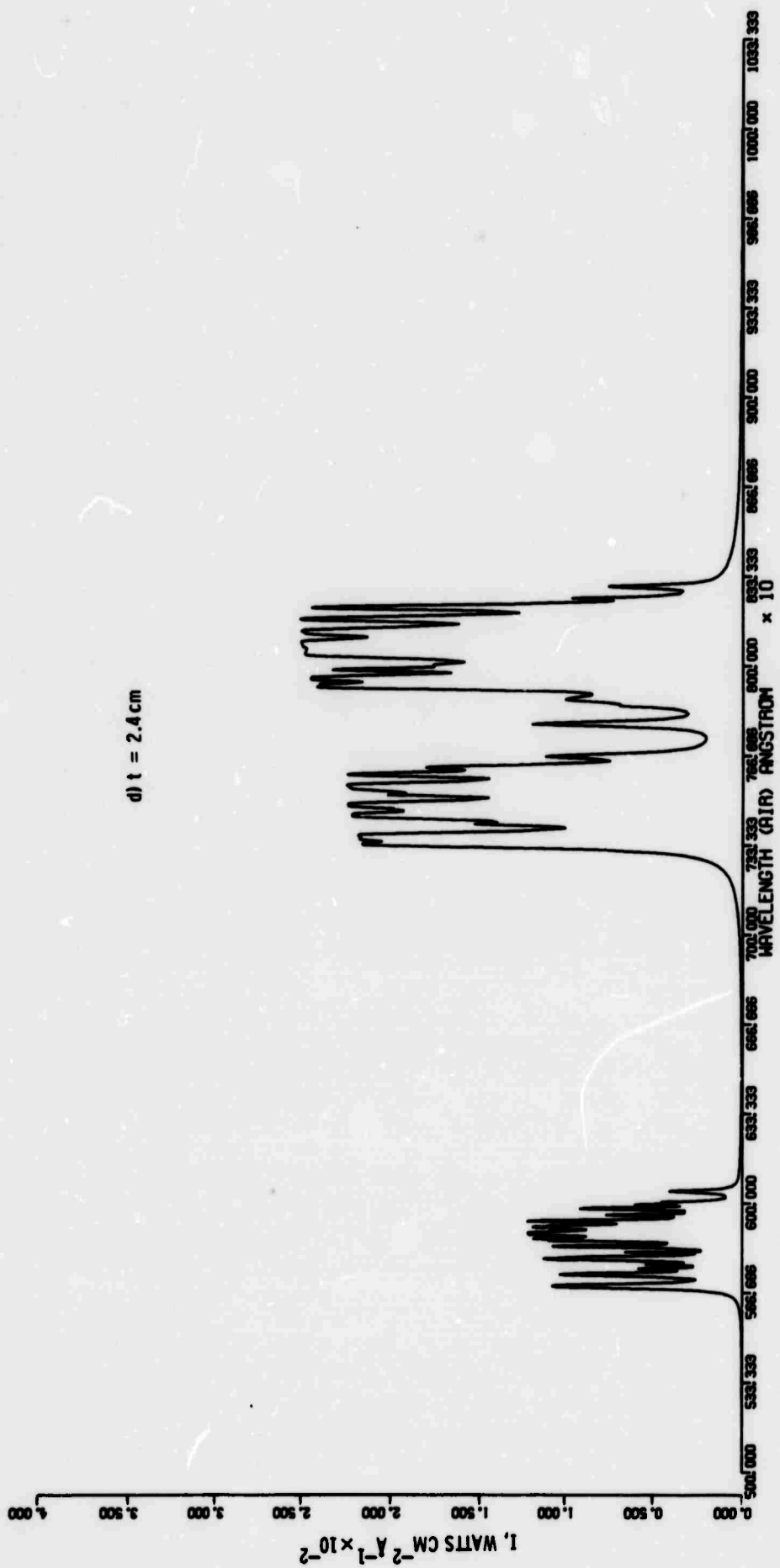


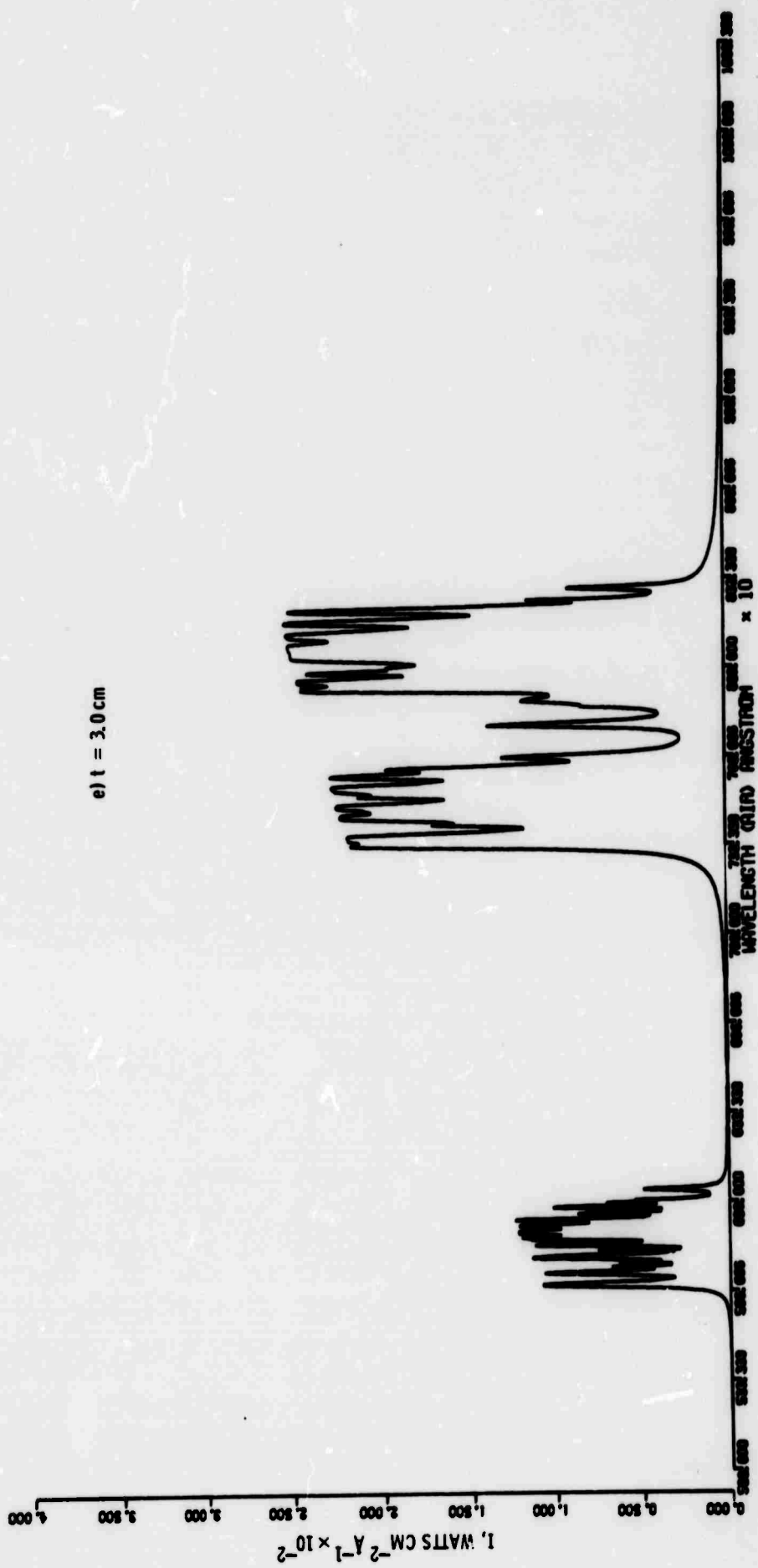
Fig. 25—Spectral overlap integrand for the W-Nd: YAG system for various slab thickness

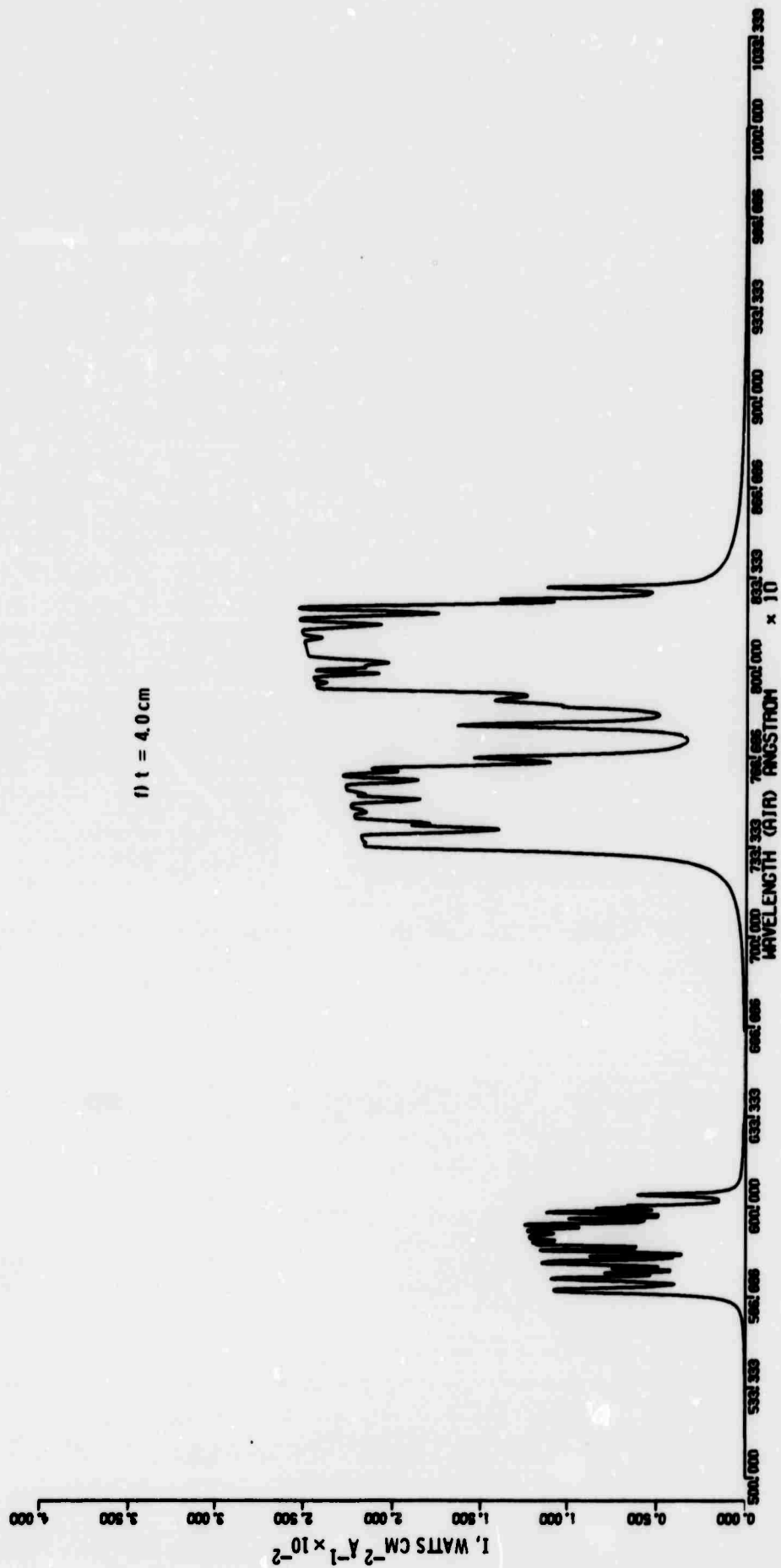












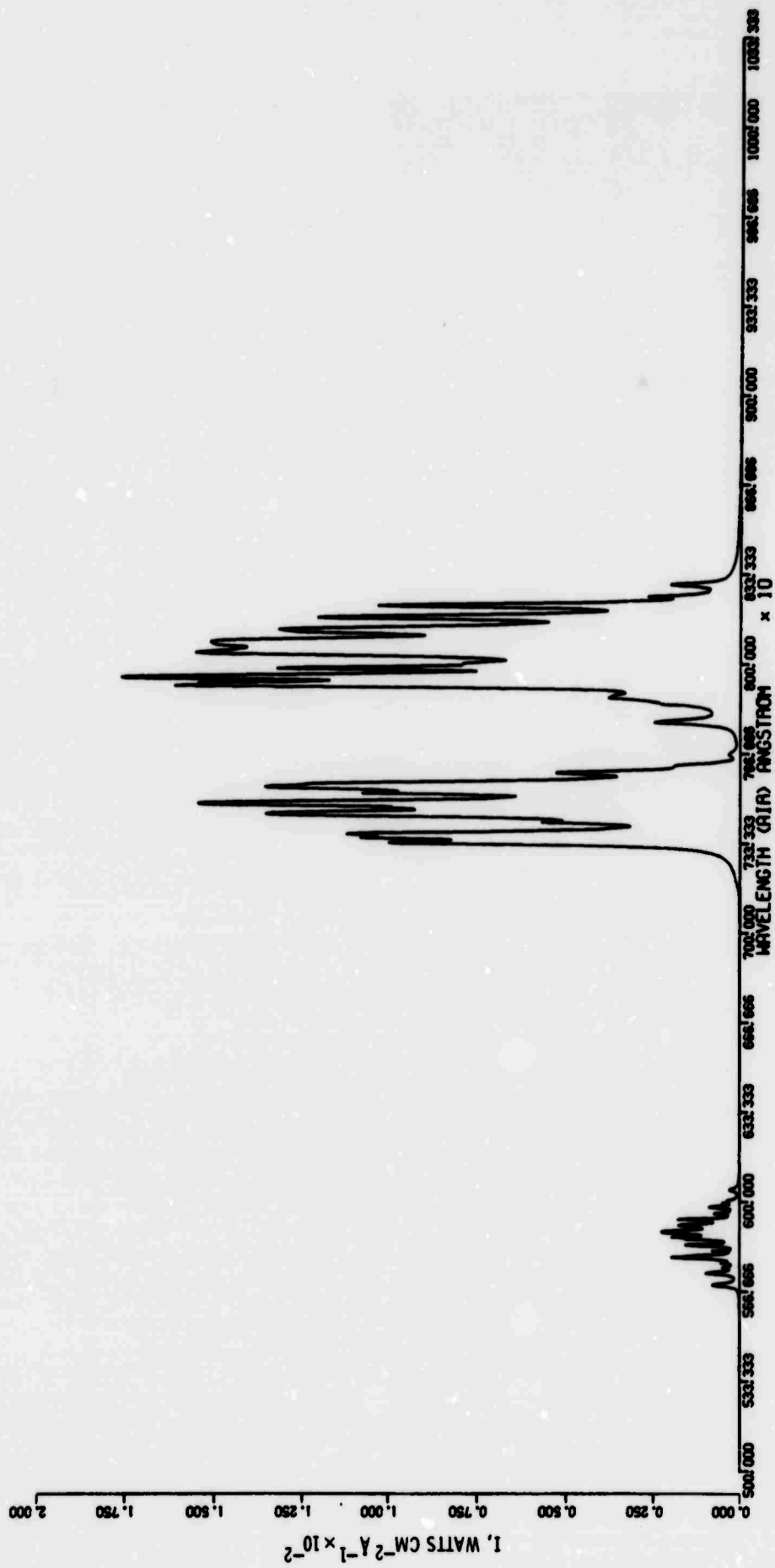


Fig. 26-Spectral overlap integrand for the K-Hg-Nd: YAG system for a 1.2 cm slab thickness

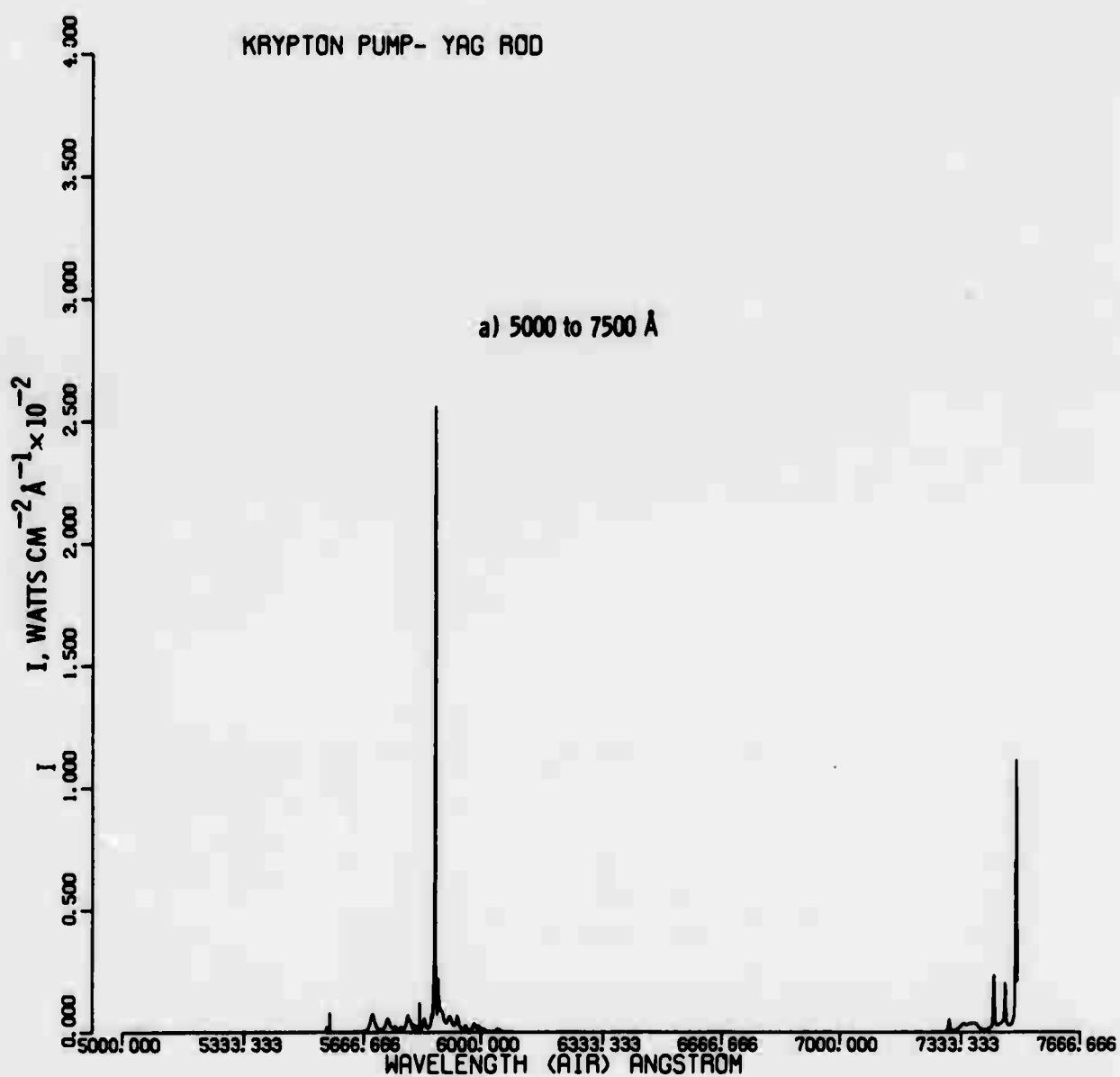
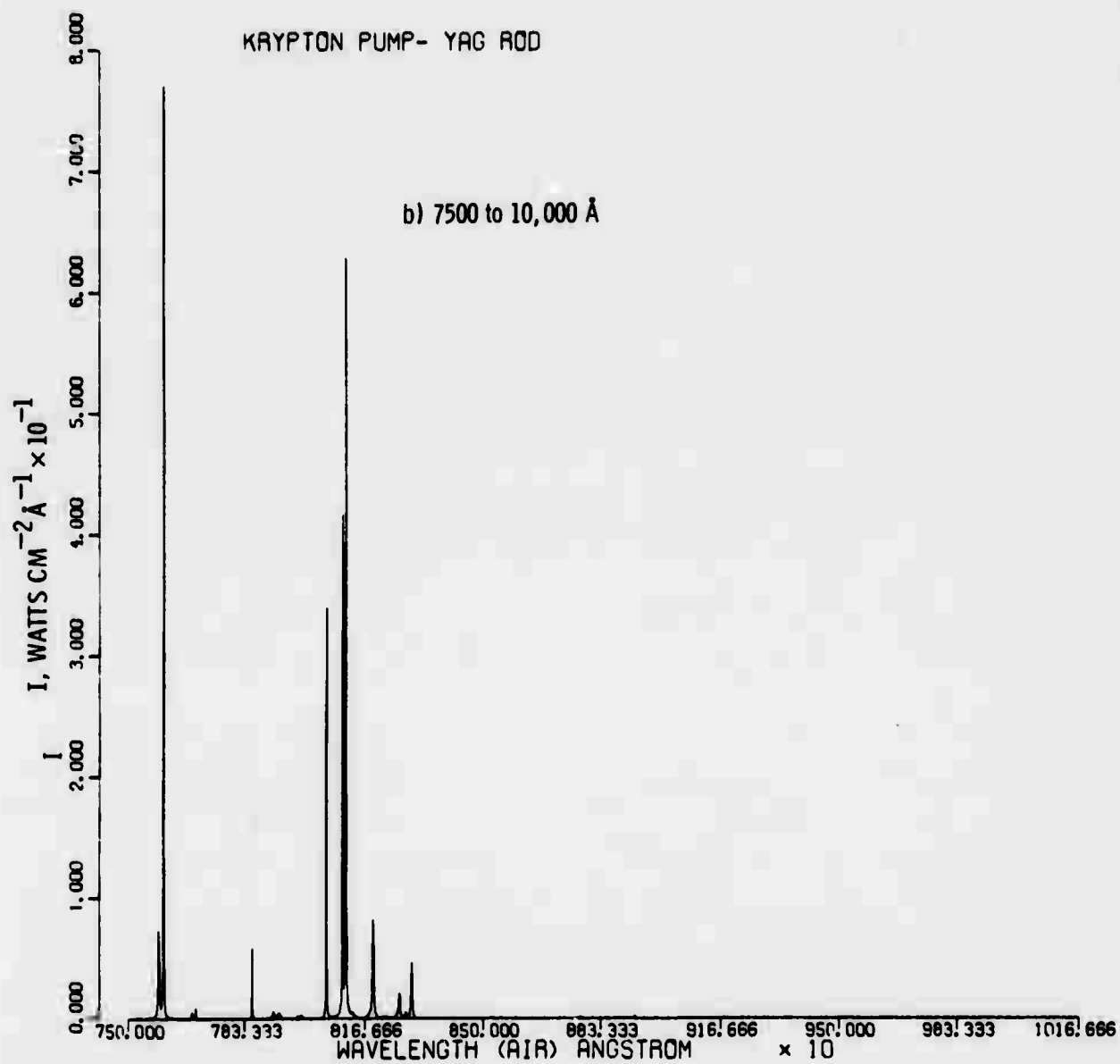


Fig. 27—Spectral overlap integrand for the Kr-Nd: YAG system for a 1.2 cm slab thickness



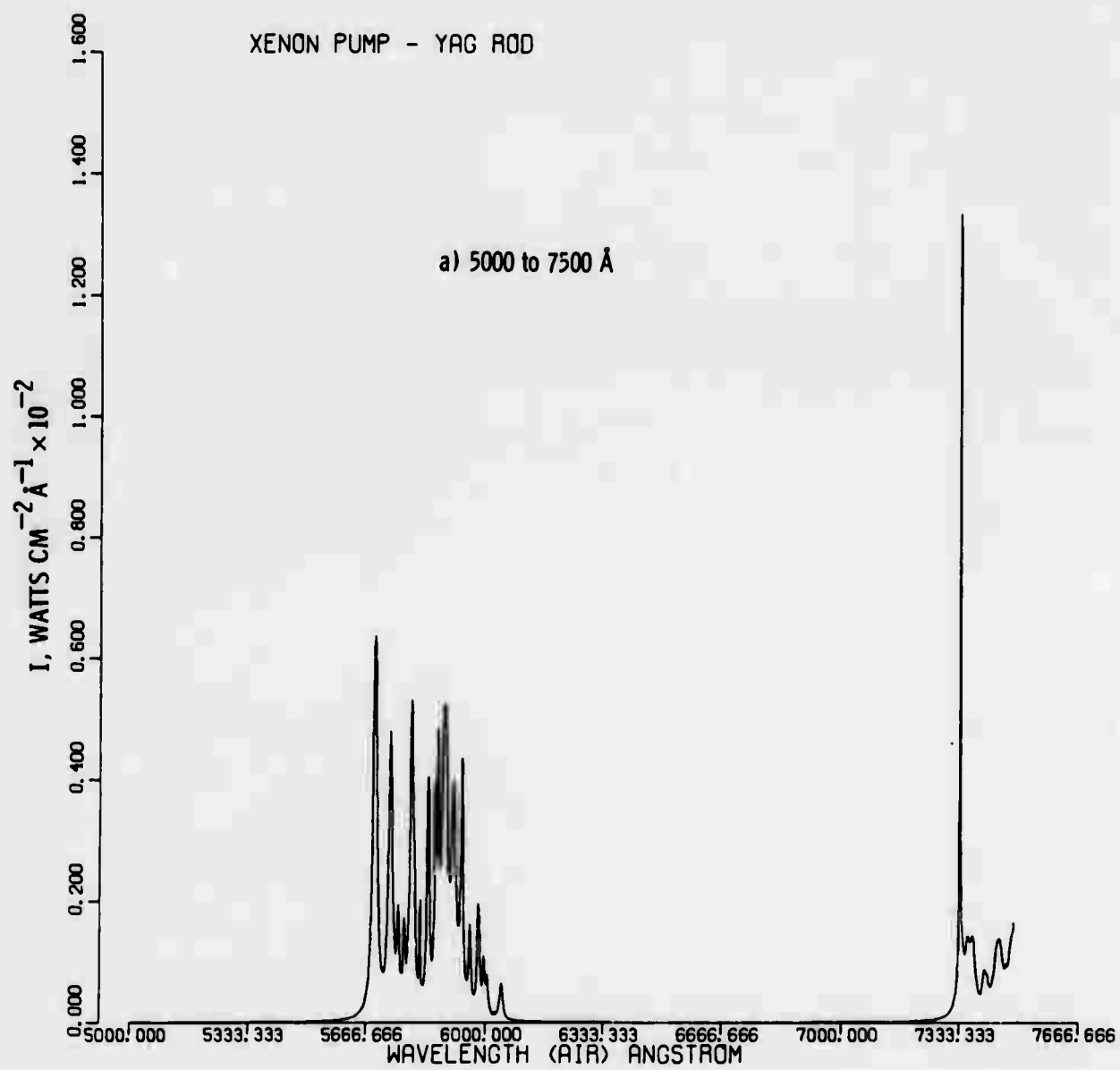
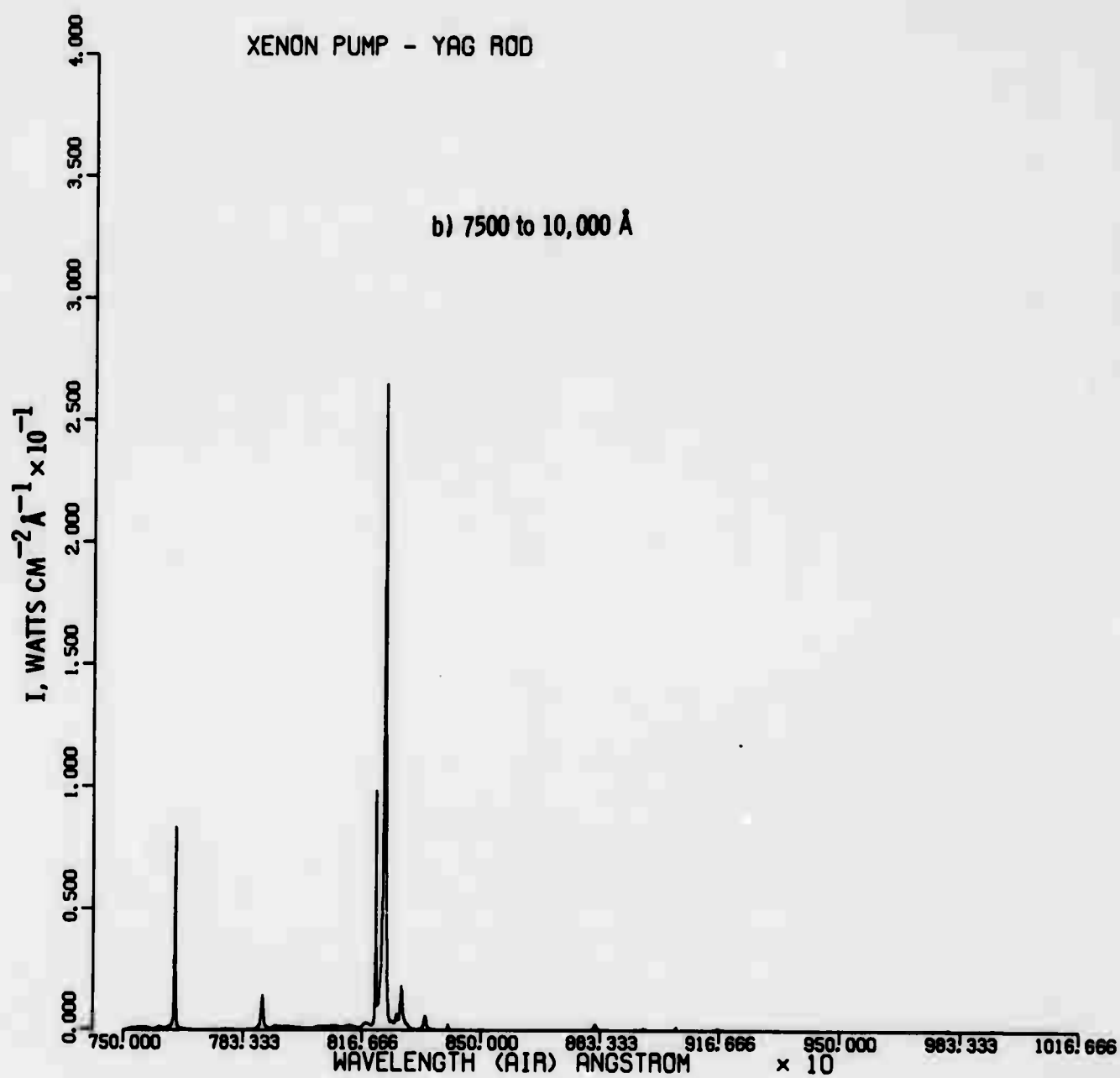


Fig. 28—Spectral overlap integrand for the Xe-Nd: YAG system for a 1.2 cm slab thickness





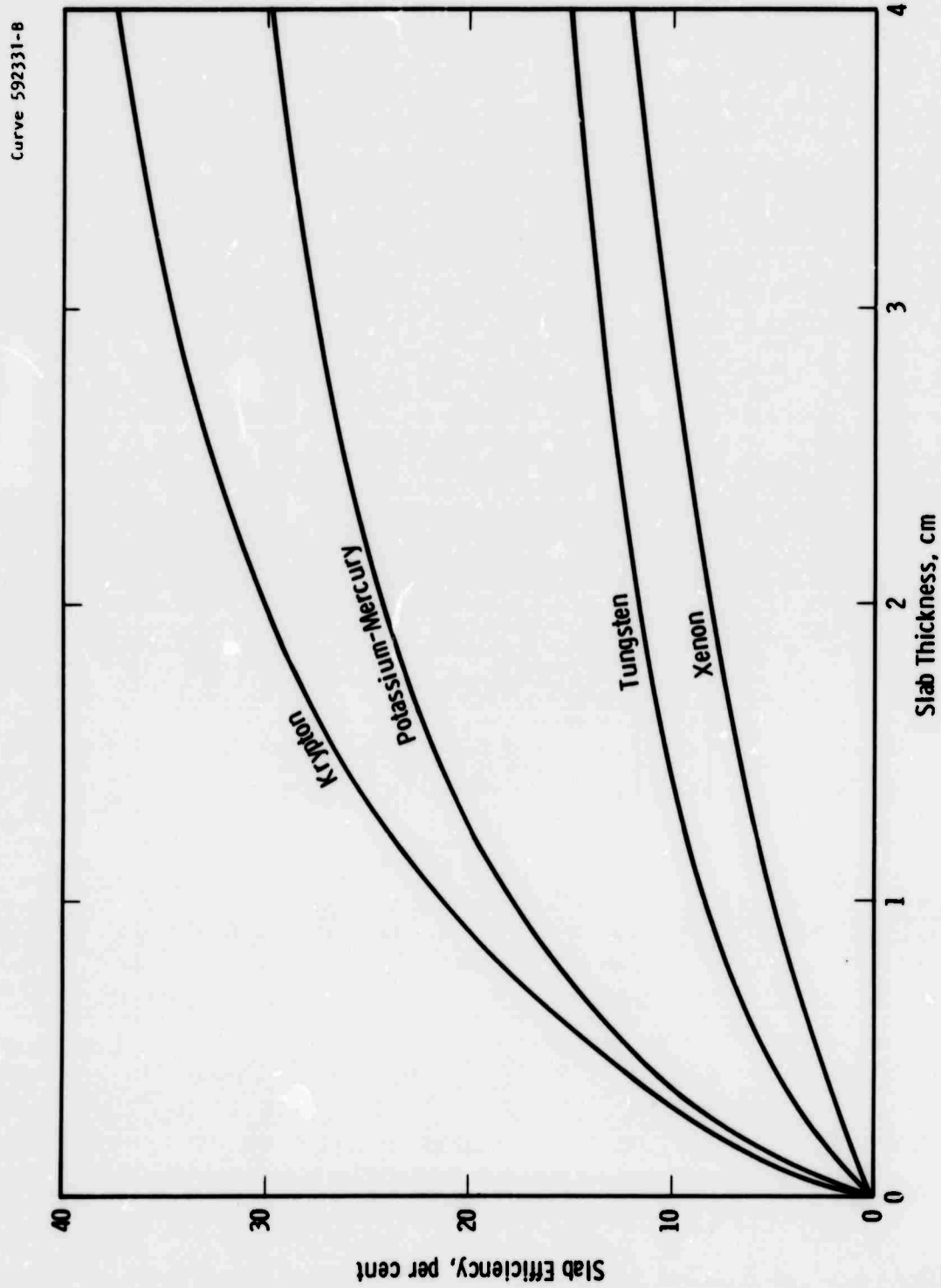


Fig. 29--Slab efficiency for 0.7% Nd:YAG being pumped by four lamps

Curve 592330-B

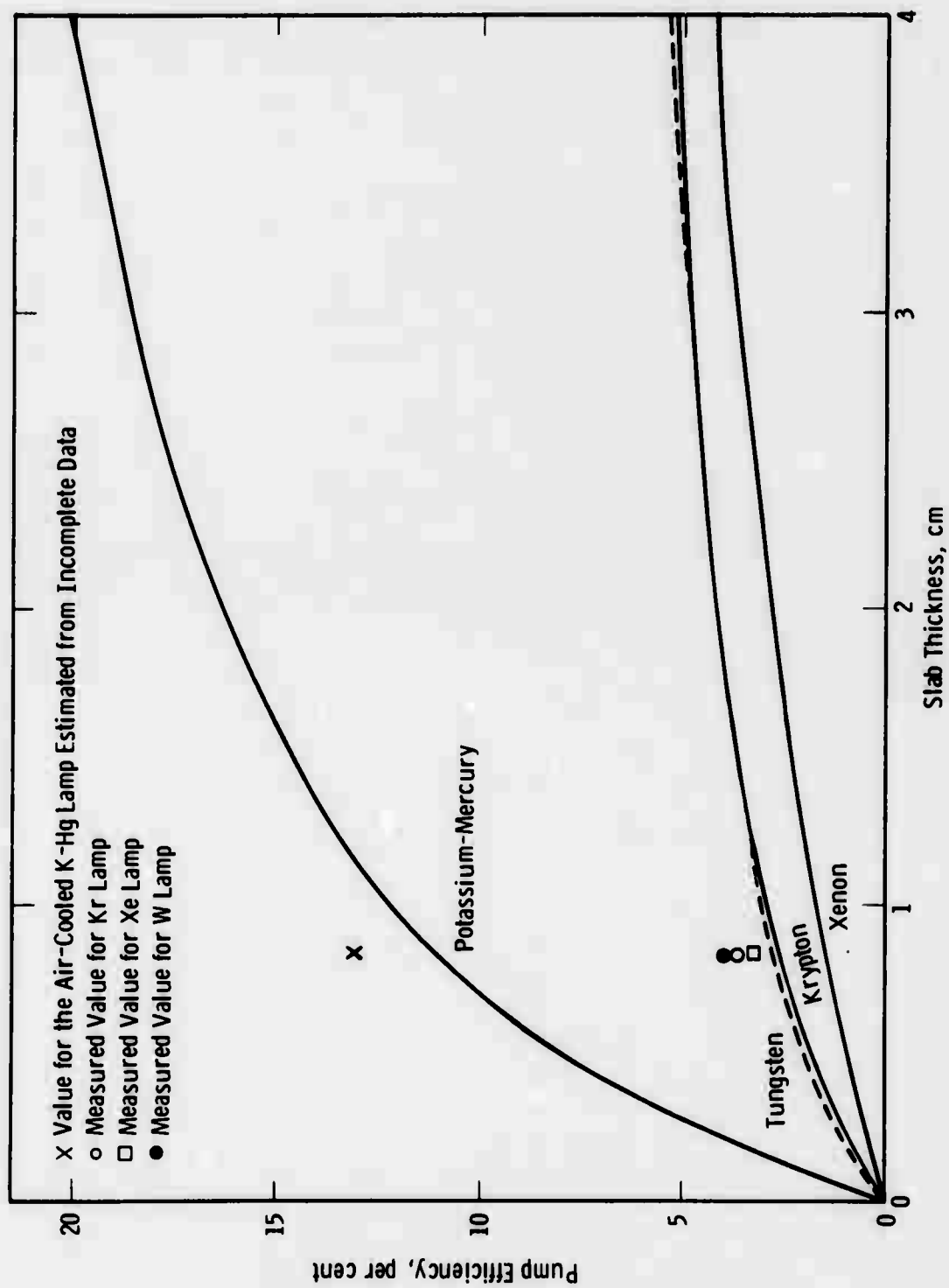


Fig. 30—Pump efficiencies for four lamps pumping a 0.7% Nd:YAG slab

Curve 592332-A

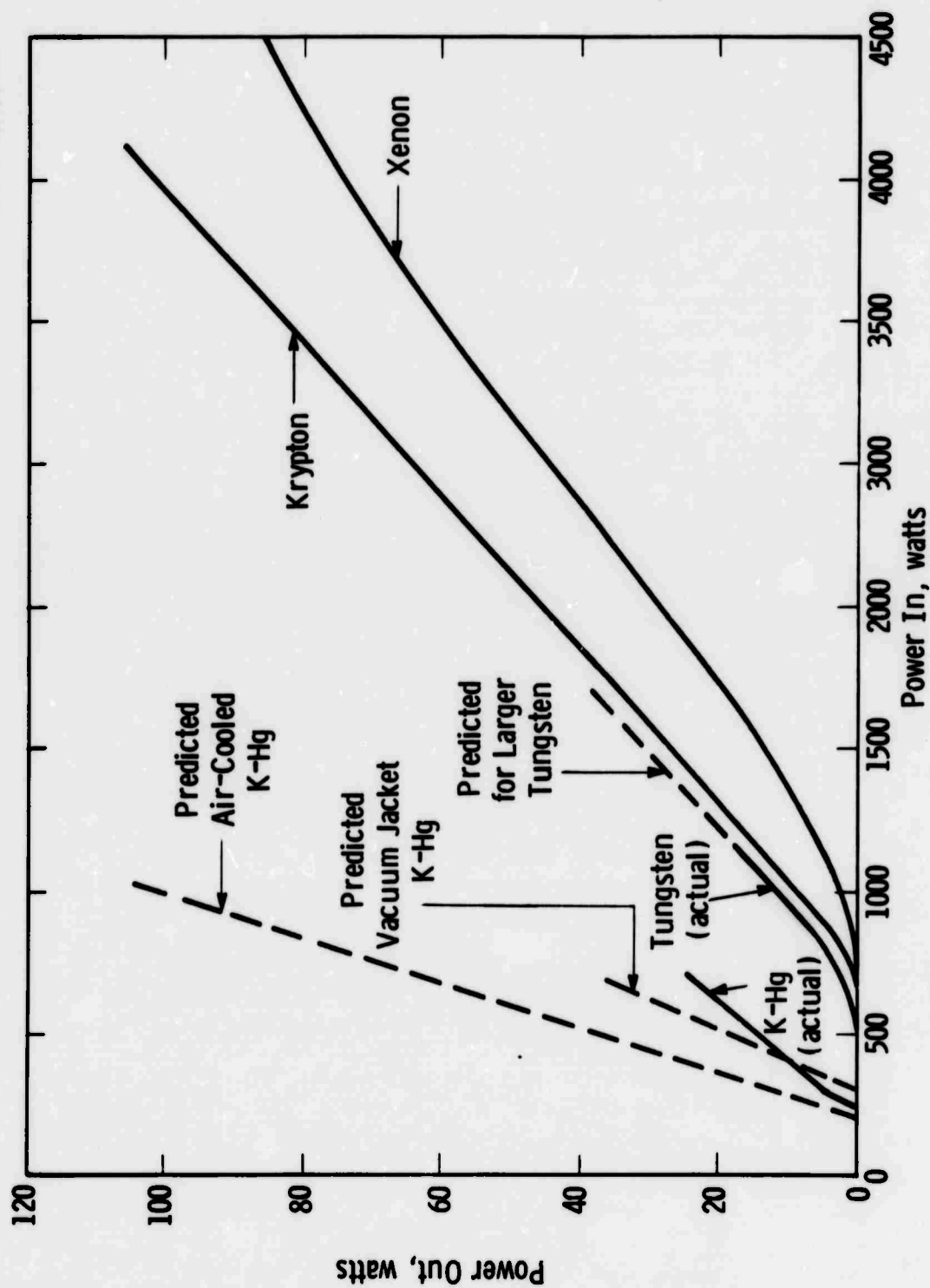


Fig. 31—Measured power conversion of a 5 x 50 mm Nd:YAG rod

Curve 592329-8

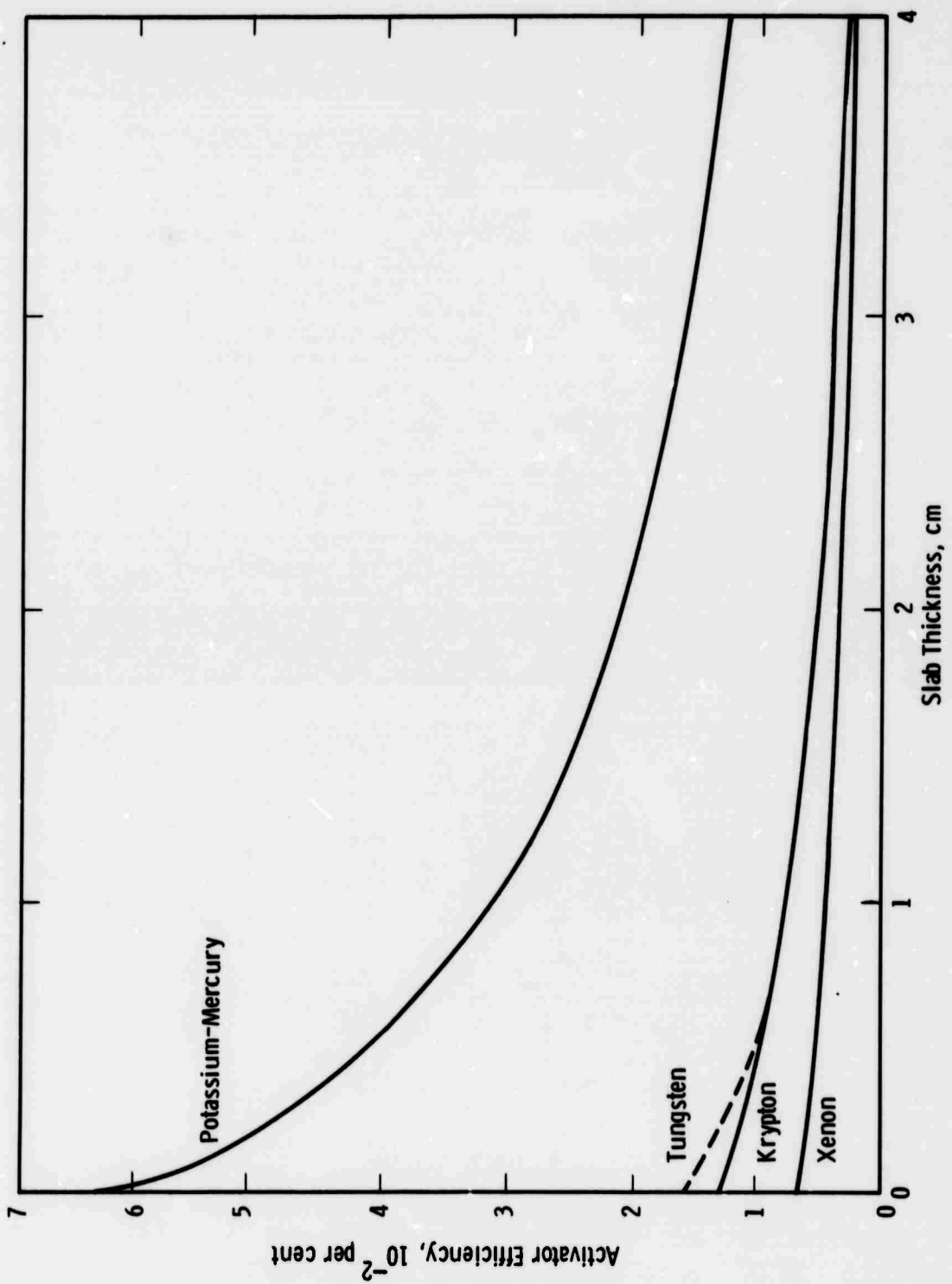


Fig. 32—Activator efficiency for four lamps pumping a 0.7% Nd:YAG slab. The input power densities have been normalized to 200 watts/cm<sup>2</sup>

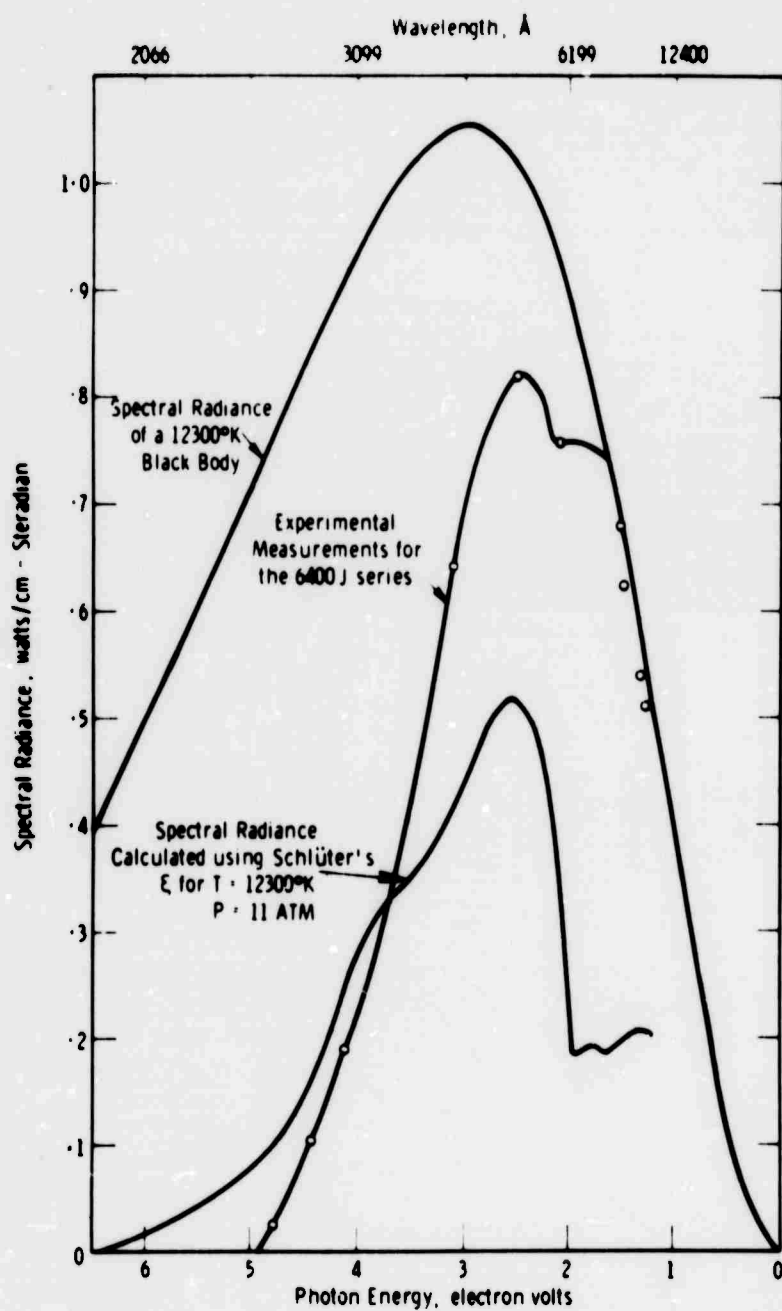


FIG. 33 Linear plot of the experimental and theoretical values for the spectral radiance of a 1.27 cm thick xenon plasma of homogeneous temperature corresponding to the 6400J - 4480 Å cm<sup>2</sup> peak current density series. Flashtube: 1.27 cm inside dia., 30 cm long, filled to 150 torr xenon.

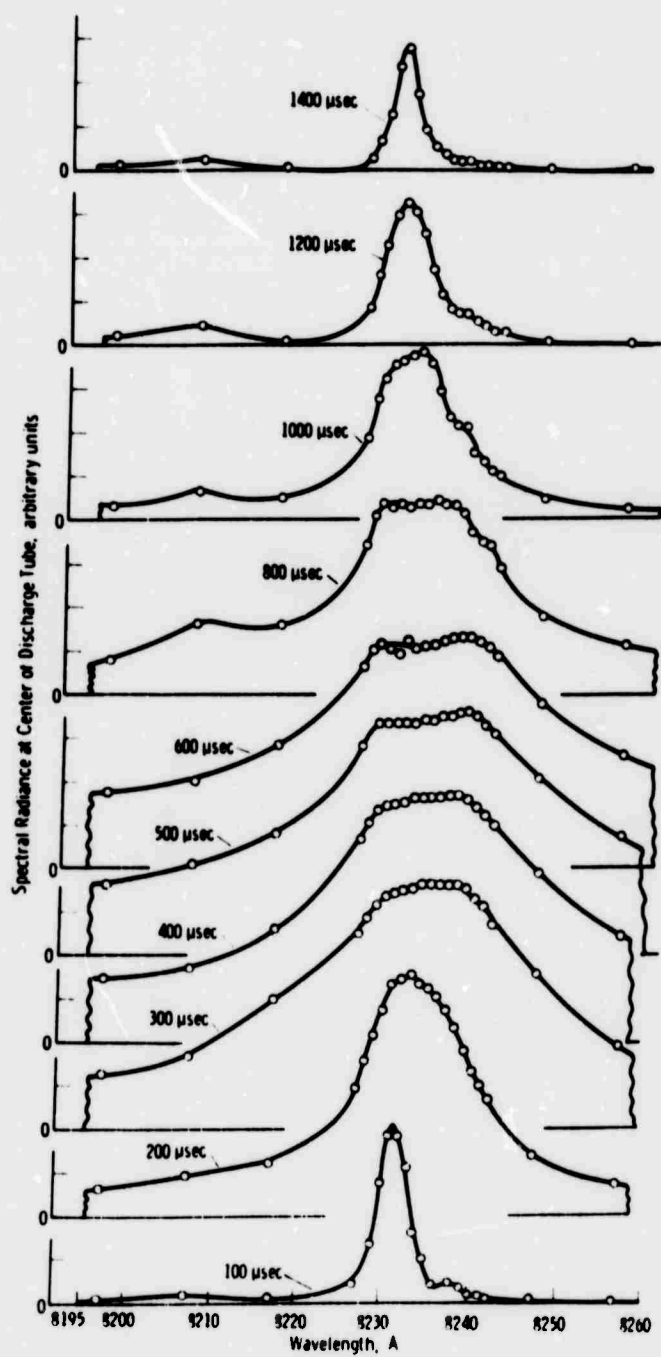


FIG 34 Time history of 8231.6 Å line of xenon, 780J input, 12.7 mm dia. tube, 150 torr initial pressure. Peak current 1140 amps. Peak electric field, 29 V/cm.

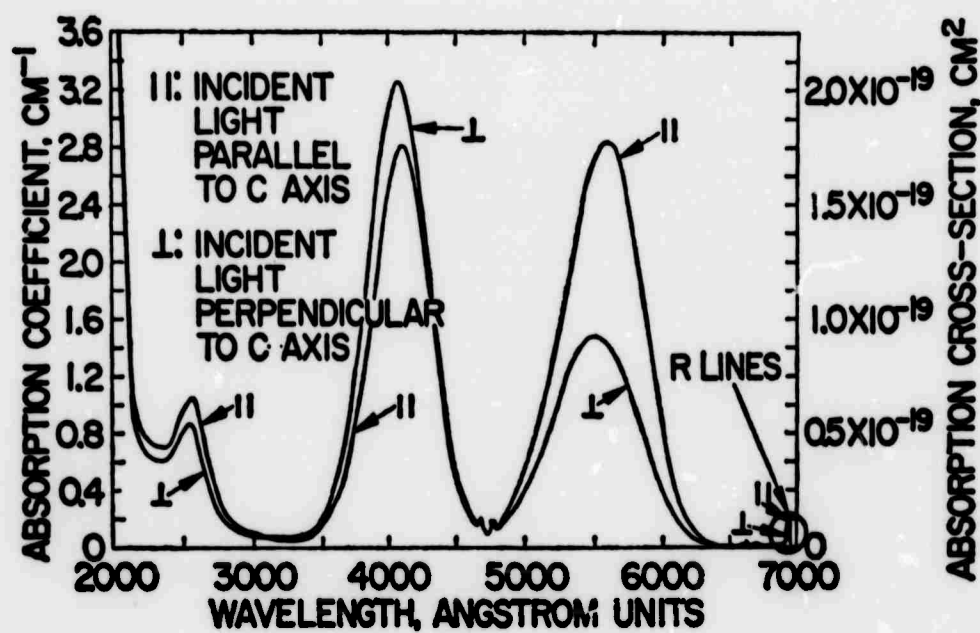


FIG. 35 Spectrophotometric absorption spectrum of ruby. The absorption cross section  $\sigma$  (right scale) is given by  $\sigma = \alpha / N_0$ , where  $\alpha$  is the linear absorption coefficient and  $N_0$  the number of absorbing centers per cm<sup>3</sup>.

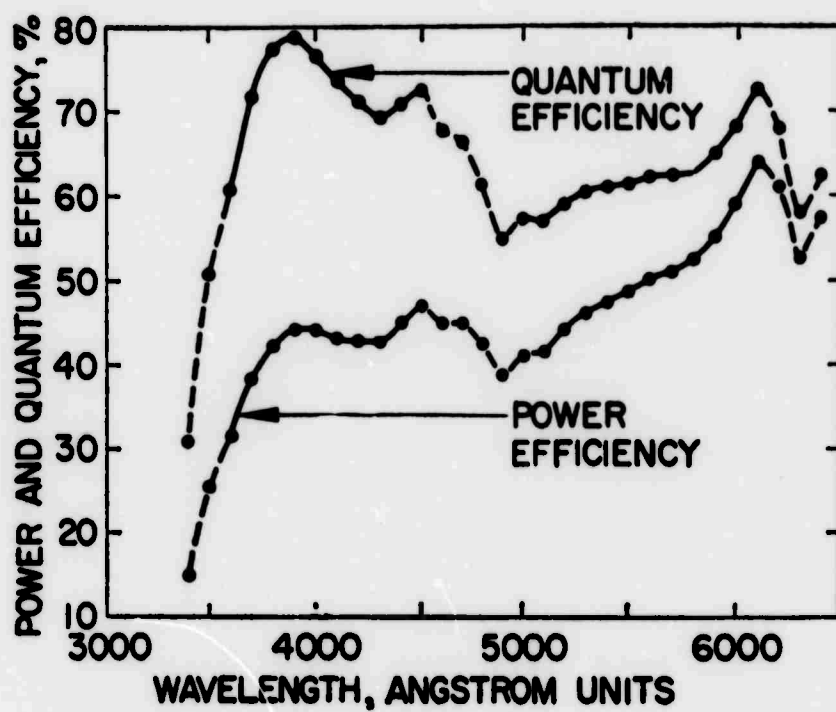


FIG. 36 Fluorescent quantum and power efficiencies for ruby: ratio of output fluorescence to input absorption as a function of wavelength.



Curve 592729-8

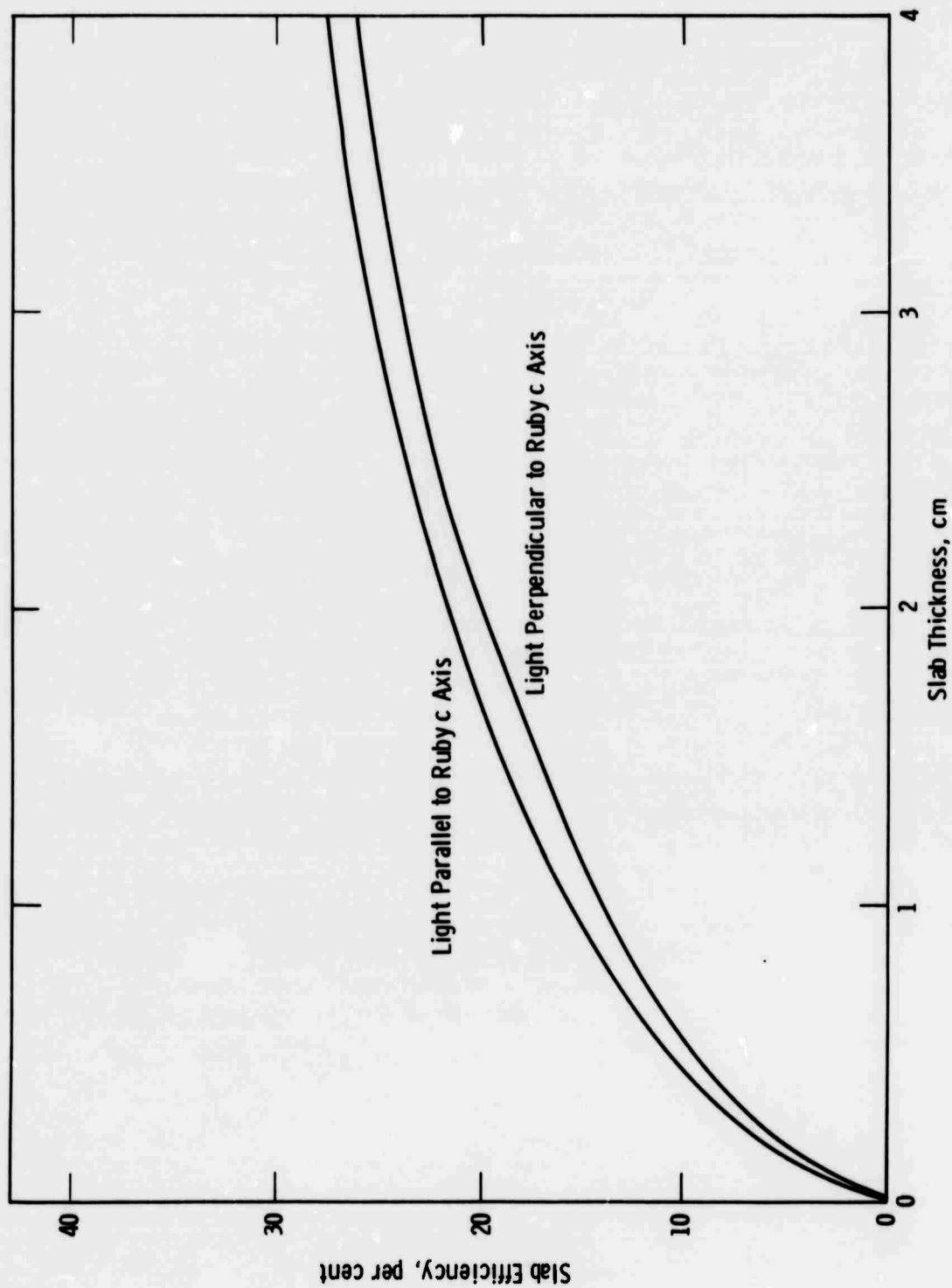


Fig. 37—Slab efficiency for a xenon flash lamp pumping a ruby slab

Curve 592730-8

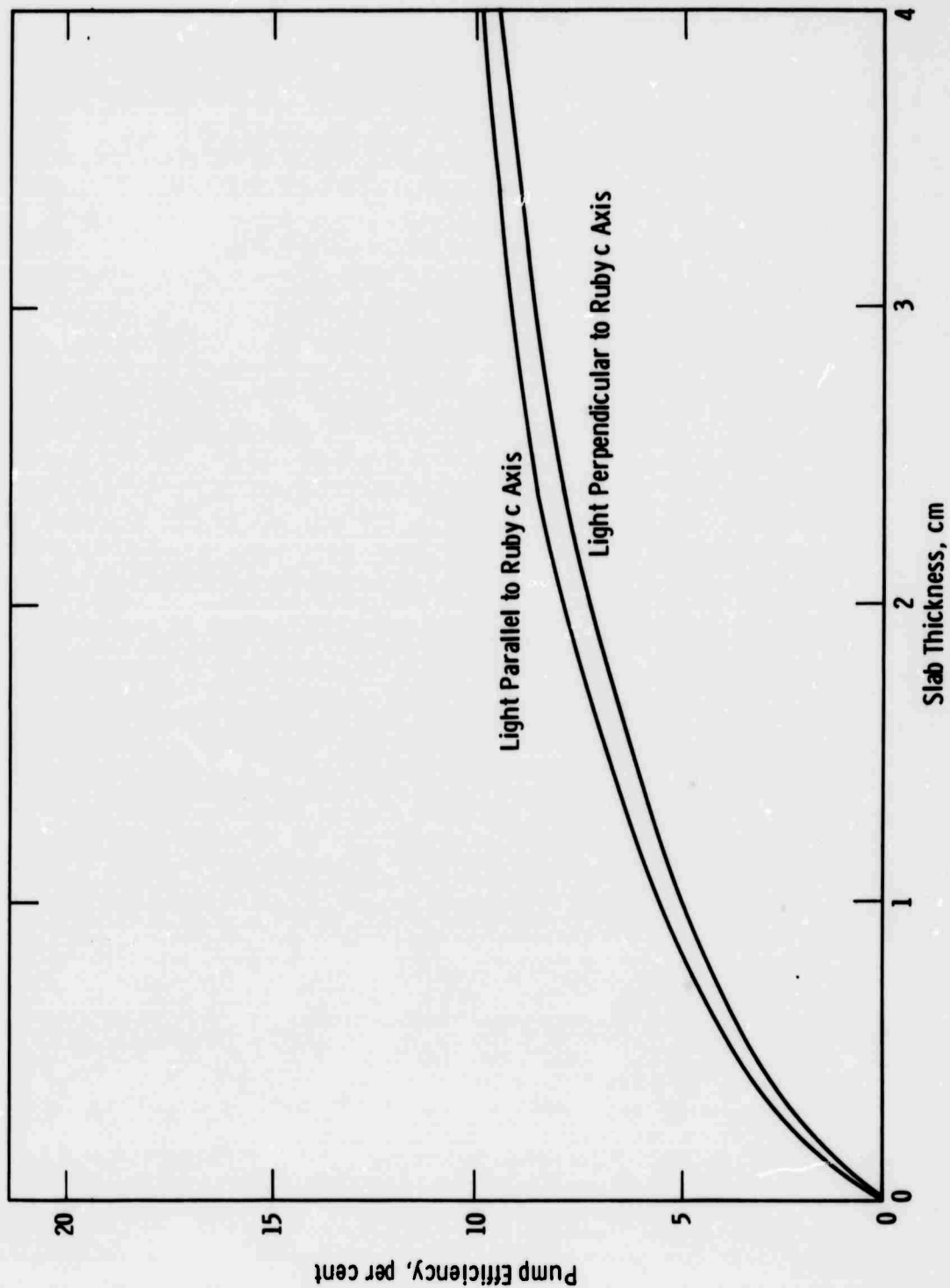


Fig. 38—Pump efficiency for a xenon flash lamp pumping a ruby slab

Curve 592728-B

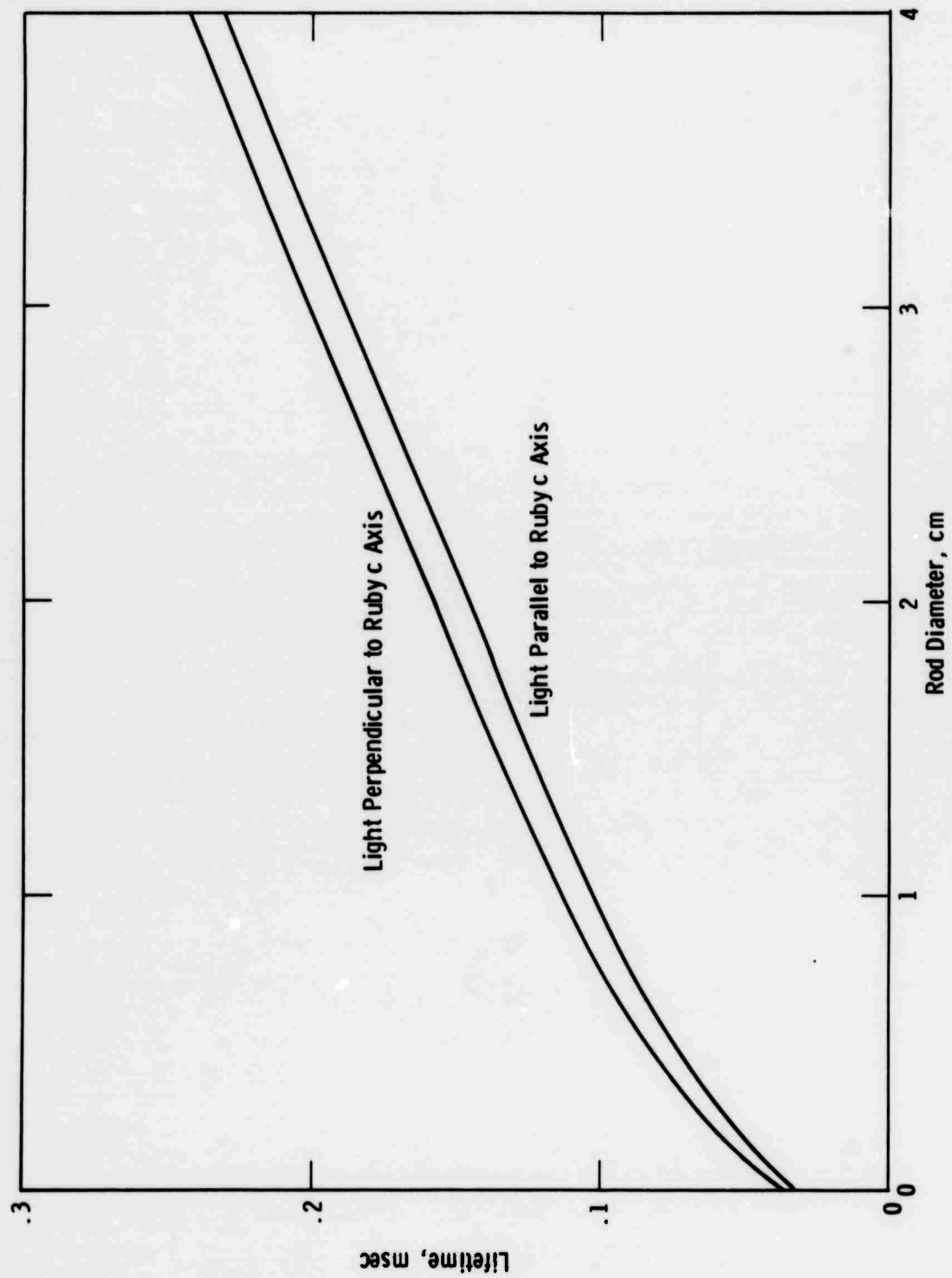


Fig. 39—Effective lifetimes of excited chromium ions in a ruby laser rod pumped by a xenon flash lamp

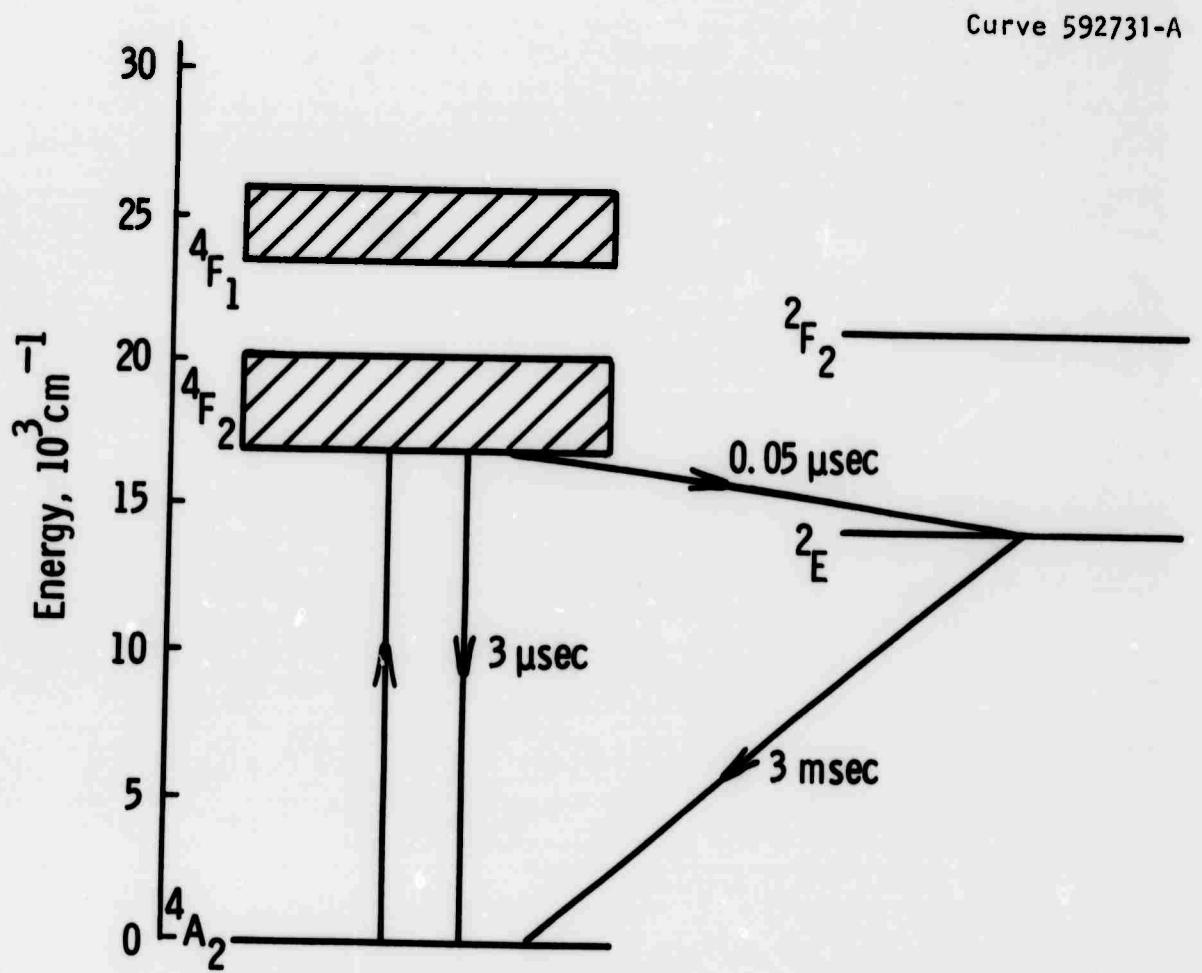


Fig. 40—Energy level diagram of ruby with lifetimes at 300°K

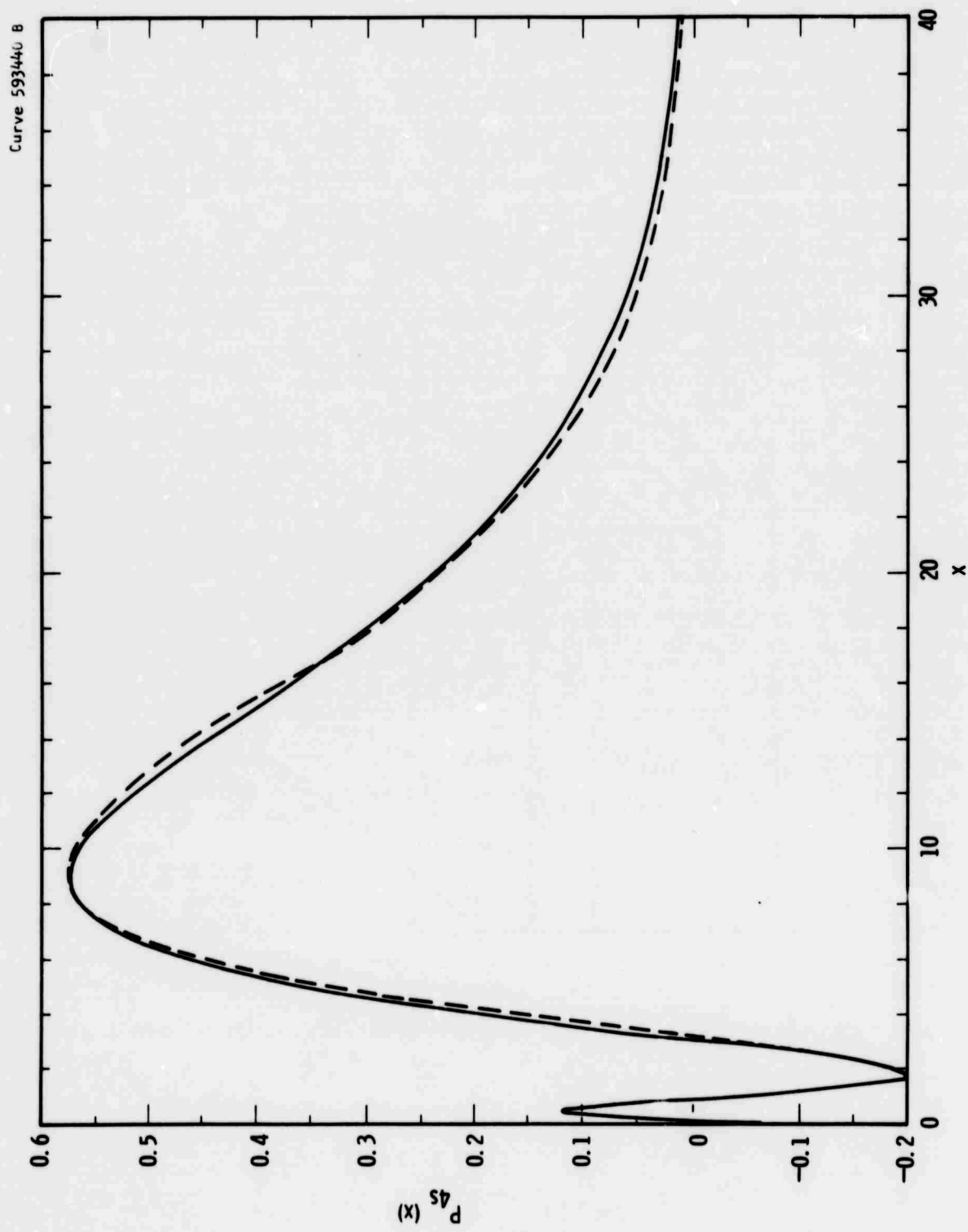


Fig. 41 - The PF Cu 4s radial wave function (dashed curve) compared to the original Hartree-Fock<sup>38</sup> radial wave function (solid curve)

Dwg. 722B512

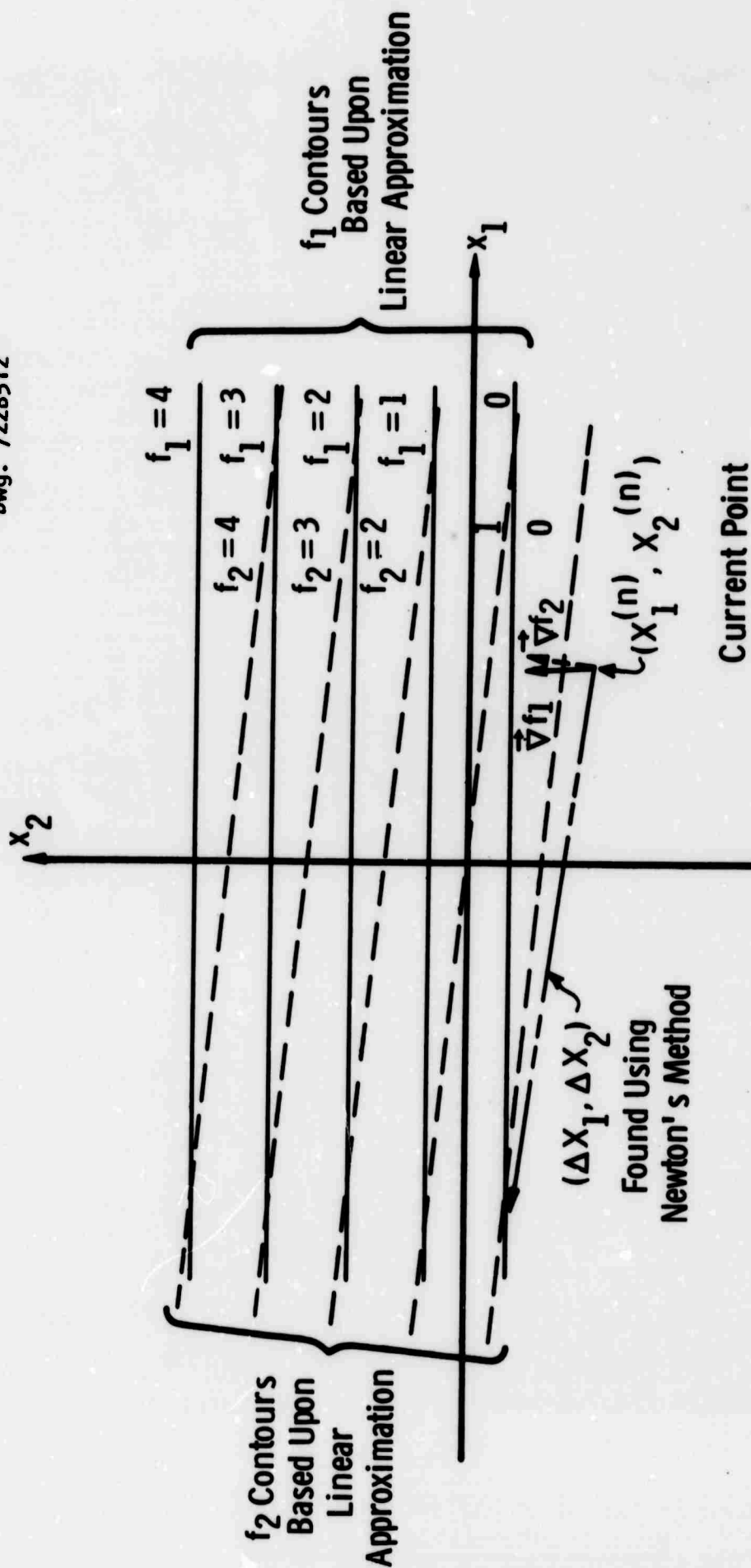


Fig. 42—Newton's method applied to two parameters which are almost linearly dependent

**BLANK PAGE**

## DOCUMENT CONTROL DATA - R&amp;D

(Security classification of title, body of abstract and indexing annotation must be entered when the overall report is classified)

1. ORIGINATING ACTIVITY (Corporate author) Westinghouse Research Laboratories Pittsburgh, Pa. 15235		2a. REPORT SECURITY CLASSIFICATION Unclassified	
		2b. GROUP	
3. REPORT TITLE OPTICAL PUMPING OF LASERS			
4. DESCRIPTIVE NOTES (Type of report and inclusive dates) Final Report 1 June 1969 to 31 March 1970			
5. AUTHOR(S) (Last name, first name, initial) Lyle H. Taylor, Irving Liberman, Richard Liebermann, Alex Federowicz, Lloyd Armstrong, Jr. (Consultant)			
6. REPORT DATE 31 May 1970	7a. TOTAL NO. OF PAGES 174	7b. NO. OF REFS 64	
8a. CONTRACT OR GRANT NO. N00014-69-C-0428	8a. ORIGINATOR'S REPORT NUMBER(S) 70-9C1-SOOPL-R3		
b. PROJECT NO.			
c. ARPA Order No. 1312			
d. Code 5704	8b. OTHER REPORT NO(S) (Any other numbers that may be assigned this report)		
10. AVAILABILITY/LIMITATION NOTICES Distribution of this document is unlimited.			
11. SUPPLEMENTARY NOTES		12. SPONSORING MILITARY ACTIVITY	
13. ABSTRACT The emission spectra of 40-amp 2.5 atm xenon and krypton arc discharges are calculated. The spectral overlap of these spectra and the measured emission spectra of tungsten and potassium-mercury arc discharges with the measured absorption spectra of Nd:YAG are used to determine relative system efficiencies which agree well with measured values. It is found that the K-Hg lamp is four times more efficient in pumping Nd:YAG than the studied W, Kr, and Xe lamps. The spectral overlap calculation for a nominal ruby oscillator-amplifier at the peak of the flash lamp pulse gives a pump efficiency which is much higher than measured system efficiencies. This discrepancy may be caused by the time dependent behavior of the flash lamp pulse and the oscillator pulse. A new technique is developed to obtain electronic radial wave functions from known radial integrals. In a test case, the Cu 4s wave function is determined within $\pm 8\%$ . Group theory is applied to the calculation of radial integrals involving hydrogen wave functions and some selection rules are explained.			



14. KEY WORDS	LINK A		LINK B		LINK C	
	ROLE	WT	ROLE	WT	ROLE	WT
Absorption Arcs Configurations Emission Gases Lasers Theory Optical Pumping Wave Functions Group Theory						

### INSTRUCTIONS

**1. ORIGINATING ACTIVITY:** Enter the name and address of the contractor, subcontractor, grantee, Department of Defense activity or other organization (corporate author) issuing the report.

**2a. REPORT SECURITY CLASSIFICATION:** Enter the overall security classification of the report. Indicate whether "Restricted Data" is included. Marking is to be in accordance with appropriate security regulations.

**2b. GROUP:** Automatic downgrading is specified in DoD Directive 5200.10 and Armed Forces Industrial Manual. Enter the group number. Also, when applicable, show that optional markings have been used for Group 3 and Group 4 not authorized.

**3. REPORT TITLE:** Enter the complete report title in all capital letters. Titles in all cases should be unclassified. If a meaningful title cannot be selected without classification, show title classification in all capitals in parentheses immediately following the title.

**4. DESCRIPTIVE NOTES:** If appropriate, enter the type of report, e.g., interim, progress, summary, annual, or final. Give the inclusive dates when a specific reporting period is covered.

**5. AUTHOR(S):** Enter the name(s) of author(s) as shown on or in the report. Enter last name, first name, middle initial. If military, show rank and branch of service. The name of the principal author is an absolute minimum requirement.

**6. REPORT DATE:** Enter the date of the report as day, month, year; or month, year. If more than one date appears on the report, use date of publication.

**7a. TOTAL NUMBER OF PAGES:** The total page count should follow normal pagination procedures, i.e., enter the number of pages containing information.

**7b. NUMBER OF REFERENCES:** Enter the total number of references cited in the report.

**8a. CONTRACT OR GRANT NUMBER:** If appropriate, enter the applicable number of the contract or grant under which the report was written.

**8b, 8c, & 8d. PROJECT NUMBER:** Enter the appropriate military department identification, such as project number, subproject number, system numbers, task number, etc.

**9a. ORIGINATOR'S REPORT NUMBER(S):** Enter the official report number by which the document will be identified and controlled by the originating activity. This number must be unique to this report.

**9b. OTHER REPORT NUMBER(S):** If the report has been assigned any other report numbers (either by the originator or by the sponsor), also enter this number(s).

**10. AVAILABILITY/LIMITATION NOTICES:** Enter any limitations on further dissemination of the report, other than those

imposed by security classification, using standard statements such as:

- (1) "Qualified requesters may obtain copies of this report from DDC."
- (2) "Foreign announcement and dissemination of this report by DDC is not authorized."
- (3) "U. S. Government agencies may obtain copies of this report directly from DDC. Other qualified DDC users shall request through \_\_\_\_\_."
- (4) "U. S. military agencies may obtain copies of this report directly from DDC. Other qualified users shall request through \_\_\_\_\_."
- (5) "All distribution of this report is controlled. Qualified DDC users shall request through \_\_\_\_\_."

If the report has been furnished to the Office of Technical Services, Department of Commerce, for sale to the public, indicate this fact and enter the price, if known.

**11. SUPPLEMENTARY NOTES:** Use for additional explanatory notes.

**12. SPONSORING MILITARY ACTIVITY:** Enter the name of the departmental project office or laboratory sponsoring (paying for) the research and development. Include address.

**13. ABSTRACT:** Enter an abstract giving a brief and factual summary of the document indicative of the report, even though it may also appear elsewhere in the body of the technical report. If additional space is required, a continuation sheet shall be attached.

It is highly desirable that the abstract of classified reports be unclassified. Each paragraph of the abstract shall end with an indication of the military security classification of the information in the paragraph, represented as (TS), (S), (C), or (U).

There is no limitation on the length of the abstract. However, the suggested length is from 150 to 225 words.

**14. KEY WORDS:** Key words are technically meaningful terms or short phrases that characterize a report and may be used as index entries for cataloging the report. Key words must be selected so that no security classification is required. Identifiers, such as equipment model designation, trade name, military project code name, geographic location, may be used as key words but will be followed by an indication of technical context. The assignment of links, rules, and weights is optional.